PLASMONIC EFFECTS UPON OPTICAL TRAPPING OF METAL NANOPARTICLES

Maria Dienerowitz

A Thesis Submitted for the Degree of PhD
at the
University of St. Andrews

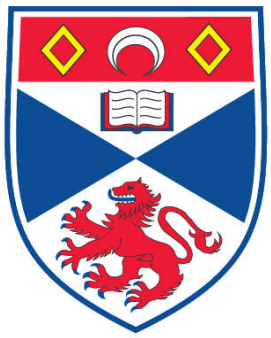

2010

Full metadata for this item is available in
Research@StAndrews:FullText
at:
https://research-repository.st-andrews.ac.uk/

Please use this identifier to cite or link to this item:
http://hdl.handle.net/10023/1634

This item is protected by original copyright

This item is licensed under a
Creative Commons License

Plasmonic effects upon Optical Trapping of metal nanoparticles

Maria Dienerowitz

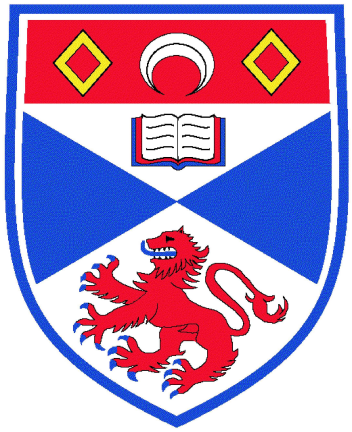

Thesis submitted for the degree of Doctor of Philosophy
of the University of St Andrews

July 3, 2010

Declaration

I, Maria Dienerowitz, hereby certify that this thesis, which is approximately 35,000 words in length, has been written by me, that it is the record of work carried out by me and that it has not been submitted in any previous application for a higher degree. I was admitted as a research student in September 2006 and as a candidate for the degree of Doctor of Philosophy in June 2007; the higher study for which this is a record was carried out in the University of St Andrews between 2006 and 2010.

Signature of Candidate:..... Date: .....

I hereby certify that the candidate has fulfilled the conditions of the Resolution and Regulations appropriate for the degree of Doctor of Philosophy in the University of St Andrews and that the candidate is qualified to submit this thesis in application for that degree.

Signature of Supervisor:..... Date: .....

In submitting this thesis to the University of St Andrews we understand that we are giving permission for it to be made available for use in accordance with the regulations of the University Library for the time being in force, subject to any copyright vested in the work not being affected thereby. I also understand that the title and abstract will be published, and that a copy of the work may be made and supplied to any bona fide library or research worker, that my thesis will be electronically accessible for personal or research use unless exempt by award of an embargo as requested below, and that the library has the right to migrate my thesis into new electronic forms as required to ensure continued access to the thesis. We have obtained any third-party copyright permissions that may be required in order to allow such access and migration, or have requested the appropriate embargo below. The following is an agreed request by candidate and supervisor regarding the electronic publication of this thesis: Access to Printed copy and electronic publication of thesis through the University of St Andrews.

Signature of Candidate:..... Signature of Supervisor:.....

Date: .....

Abstract

Optical trapping of metal nanoparticles investigates phenomena at the interface of plasmonics and optical micromanipulation. This thesis combines ideas of optical properties of metals originating from solid state physics with force mechanism resulting from optical trapping. We explore the influence of the particle plasmon resonance of gold and silver nanospheres on their trapping properties. We aspire to predict the force mechanisms of resonant metal particles with sizes in the Mie regime, beyond the Rayleigh limit.

Optical trapping of metal nanoparticles is still considered difficult, yet it provides an excellent tool to investigate their plasmonic properties away from any interface and offers opportunities to investigate interaction processes between light and nanoparticles. Due to their intrinsic plasmon resonance, metal nanoparticles show intriguing optical responses upon interaction with laser light. These differ greatly from the well-known bulk properties of the same material.

A given metal nanoparticle may either be attracted or repelled by laser light, only depending on the wavelength of the latter. The optical forces acting on the particle depend directly on its polarisability and scattering cross section. These parameters vary drastically around the plasmon resonance and thus not only change the magnitude but also the direction and entire nature of the acting forces. We distinguish between red-detuned and blue-detuned trapping, that is using a trapping wavelength shorter or longer than the plasmon resonance of the particle. So far optical trapping of metal nanoparticles has focussed on a wavelength regime far from the particle's resonance in the infrared. We experiment with laser wavelengths close to the plasmon resonance and expand the knowledge of metal nanoparticle trapping available to date. Existing theoretical models are put to the test when we compare these with our real experimental situations.

Contents

1 Introduction **11**

2 Theoretical foundation **15**
2.1 Interaction of light with matter 16
2.1.1 Polaritons and plasmons 17
2.1.2 Optical properties of metals 19
2.1.3 Optical manipulation of matter 22
2.2 Spherical metal nanoparticles 25
2.2.1 The Particle Plasmon 26
2.2.2 Quasi-static approximation 27
2.2.3 Mie theory 29
2.2.4 Results and discussion 31
2.3 Forces in optical trapping 38
2.3.1 Maxwell stress tensor and Lorentz force 39
2.3.2 Gradient and scattering force decomposition 40
2.3.3 Limits and open questions 42
2.4 Conclusions 43

3 Experimental setup **45**
3.1 Materials and sample preparation 45
3.2 The optical setup 48
3.2.1 The single-beam trap: Optical tweezers 49
3.2.2 The dual beam trap: Fibre trap 51
3.3 Imaging nanoparticles 53
3.3.1 Brightfield microscopy in transmission - diascopic illumination 54
3.3.2 Brightfield microscopy in reflection - episcopic illumination . . 56
3.3.3 Darkfield microscopy 61
3.4 Detecting nanoparticles 63
3.4.1 Video detection: Particle tracking 64
3.4.2 Electronic detection: Quadrant photodiode 65
3.4.3 Calibrating the detection system 68
3.5 Conclusions 73

4 Optical trapping above resonance **75**
4.1 The single-beam trap . . . 76
4.2 Characterising the optical trap . . . 78
4.2.1 Histograms and potential energy . . . 79
4.2.2 Power spectrum and roll-off frequency . . . 80
4.2.3 Trap stiffness . . . 82
4.3 Results and discussion . . . 83
4.4 Wavelength dependence of the trap stiffness . . . 88
4.4.1 Supercontinuum beam profile . . . 90
4.5 Conclusions . . . 93

5 Optical trapping below resonance **95**
5.1 Optical vortex trap for resonant confinement . . . 96
5.1.1 Laguerre-Gaussian beams . . . 96
5.1.2 Laguerre-Gaussian trap . . . 98
5.2 Orbital angular momentum transfer . . . 102
5.3 Results and discussion . . . 104
5.4 Conclusion . . . 109

6 Summary and Outlook **111**

Bibliography **114**

Publications **123**

List of symbols and acronyms

The tables give all acronyms and symbols used throughout this thesis in alphabetical order.

CCD	charge-coupled device
cw	continuous wave
DIC	differential interference contrast
InGaAs	Indium gallium arsenide
LG	Laguerre-Gaussian
NA	numerical aperture
OAM	orbital angular momentum
QPD	quadrant photodiode
SEM	scanning electron microscope
TE	tranverse electric
TEM	transverse electromagnetic
TM	transverse magnetic

α	polarisability
γ	drag coefficient
γ_c	collision damping frequency
ε_0	vacuum permittivity
δ	skin depth
ε_b	background permittivity
ε_r	relative permittivity
η	dynamic viscosity
κ	trap stiffness
λ	wavelength
μ_0	vacuum permeability
μ_r	relative permeability
ρ	charge density
σ	standard deviation
χ	susceptibility
ω	frequency
ω_p	plasma frequency

$\mathbf{B}$	magnetic induction
c	speed of light in medium
c_0	speed of light in vacuum
$\mathrm{C}_{\mathrm{abs}}$	absorption cross section
$\mathrm{C}_{\mathrm{ext}}$	extinction cross section
$\mathrm{C}_{\mathrm{scat}}$	scattering cross section
$\mathbf{D}$	electric displacement
d	diameter of a sphere
$\mathbf{E}$	electric field
e	electric charge
f_c	corner frequency
$\mathbf{F}_{\mathrm{abs}}$	absorption force
$\mathbf{F}_{\mathrm{grad}}$	gradient force
$\mathbf{F}_{\mathrm{scat}}$	scattering force
$\mathbf{H}$	magnetic field
$\mathbf{j}$	current density
k	wave vector
ℓ	azimuthal phase index
$\mathbf{M}$	magnetisation
m_e	effective elecron mass
m	relative refractive index
n_d	number density of electrons
ñ	refractive index of a material
$\mathbf{P}$	polarisation
$\mathbf{p}$	dipole moment
p	radial mode index
q	electric charge
r	radius of a sphere
$\mathbf{S}$	Poynting vector
$\overleftrightarrow{\mathbf{T}}$	Maxwell stress tensor
T	temperature
t	time
$\mathbf{v}$	velocity
V	volume of a sphere
x	size parameter

1 Introduction

The interaction of light with matter gives rise to the most fascinating effects. Over the centuries the size of the objects of investigation decreased and has by now arrived at nanometre dimensions - smaller than the wavelength of light itself. Research in optics thus comprises a very diverse field ranging from something as trivial as refraction through a lens to complex ideas as using light to trap atoms and small particles. In some fields light is used as a tool for investigation such as optical tweezers in optical trapping. Others thrive to control light by engineering matter, for instance metal nanostructures in the field of plasmonics.

This thesis endeavours to build a bridge between established concepts of optical trapping and plasmonics. Optical trapping has already proven to be an essential tool, not only in physics but also within biology and chemistry [1, 2]. Plasmonics has emerged as a thriving field of research over the past 10 years as a result of advances in fabrication and characterisation at the nanoscale [3, 4].

In the beginning of optical trapping it was believed that it is impossible to tweeze metal beads [5, 6]. When it was finally shown in 1994 that optical tweezing of metal nanospheres is indeed possible [7], this research field started to attract more and more attention with many questions still to explore. Although optical trapping of metal nanoparticles is still considered difficult [8–10], it provides an excellent tool to investigate their plasmonic properties away from any interface and offers opportunities to investigate interaction processes between light and nanoparticles.

Most research in plasmonics is focussed on the properties and design of planar metal nanostructures. Recently their potential for optical trapping has generated a lot of interest [11, 12]. However, 3D optical trapping of freely floating metal nanoparticles is fundamentally different to surface plasmon trapping with planar metal substrates. The latter relies on the excitation of the nanostructure to create an optical trap. Due to their intrinsic plasmon resonance, metal nanoparticles show intriguing optical responses upon interaction with laser light. These differ greatly from the well-known bulk properties of the same material. This work envisages to combine ideas of optical properties of metals originating from solid state physics with force mechanism resulting from optical trapping. We explore the influence of the particle plasmon resonance of gold and silver nanospheres on their trapping properties. We aspire to predict the force mechanisms of resonant metal particles with sizes in the Mie regime, beyond the Rayleigh limit. Our investigations are not restricted to the spectral response of metal nanoparticles but the forces applied by the incident light and the resulting interaction.

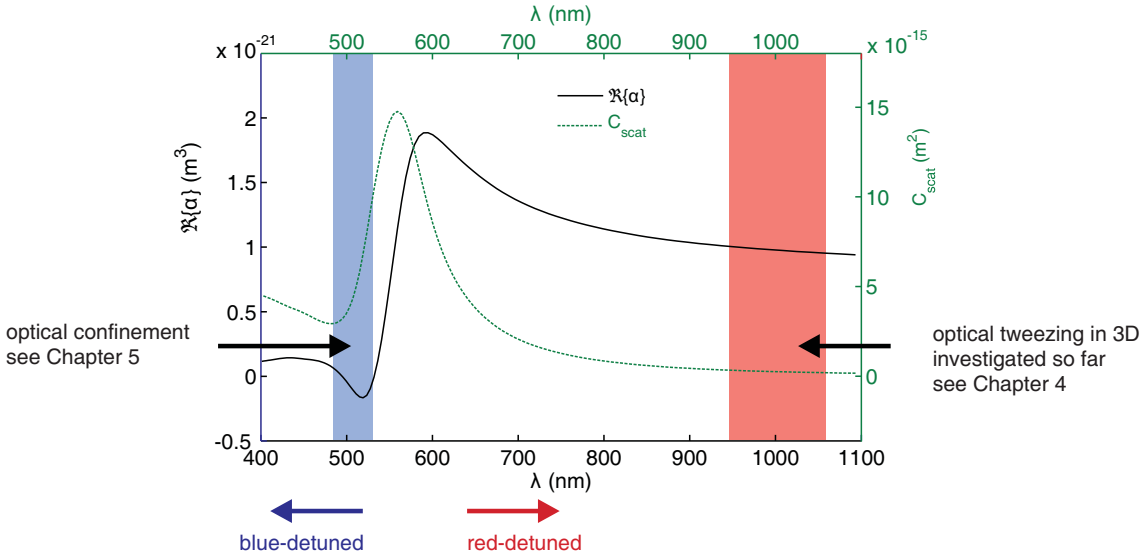

Figure 1.1: We illustrate the central theme of our work by means of the polarisability α (left axis) and scattering cross section C_{scat} (right axis) of a 80nm gold sphere. The wavelength dependence of these quantities directly influences the force light is able to exert on the particle. The wavelength region above the resonance is commonly referred to as red-detuned, below as blue-detuned. We highlighted the regions investigated so far. Experiments characterising trapping of metal nanoparticles on the red-detuned side close to resonance are still lacking to date. We obtained C_{scat} from Mie theory (see Sec. 2.2.3) and α is calculated from Eq. (2.43) explained in Sec. 2.2.4.

A given metal nanoparticle may either be attracted or repelled by laser light, only depending on the wavelength of the latter. The optical forces acting on the particle depend directly on its polarisability and scattering cross section. These parameters vary drastically around the plasmon resonance and thus not only change the magnitude but also the direction and entire nature of the acting forces. Figure 1.1 summarises this thesis using the polarisability and cross section of a 80nm gold sphere. We distinguish between red-detuned and blue-detuned trapping, that is using a trapping wavelength shorter or longer than the plasmon resonance of the particle. So far optical trapping of metal nanoparticles has focussed on a wavelength regime far from the particle's resonance in the infrared [13, 14]. We experiment with laser wavelengths close to the plasmon resonance and expand the knowledge of metal nanoparticle trapping available to date [10, 15, 16]. Existing theoretical models are put to the test when we compare these with our real experimental situations.

Typically, optical trapping is described with geometrical optics which explains tweezing a dielectric particle with the lens effect or change of direction of the incident ray of light [1, 17, 18]. The particles we study in our work are too small for us to use the geometrical optics model. However they are too large to consider them as a point dipole (Rayleigh limit). The size of our trapped particles is comparable to the

trapping wavelength (Mie regime). In addition we need to consider that light does not propagate through metal objects. Therefore we focus on the electromagnetic description of forces and matter-light interactions in our work.

The pioneering works of trapping metal nanoparticles have been conducted far from the nanoparticle's plasmon resonance, preferably using a continuous-wave trapping laser in the infrared [7]. The first applications included using a trapped gold sphere as nearfield scanning probe [19] and employ tweezers as a tool to form hot pairs for surface-enhanced Raman Spectroscopy [20]. Only recently a number of studies aimed to reveal the mechanisms of tweezing metal nanoparticles in more detail by varying the size of trapped gold and silver spheres or the trapping geometry [13, 14, 21]. In addition, possible heating effect have been investigated [22].

However there are just few trapping experiments exploring metal nanoparticles close to their resonance to date. Theoretical investigations approaching the plasmon resonance for optical trapping suggested a wavelength dependent interaction process leading to a repulsive or attractive gradient force [23–25]. The first experiments investigated the residence time of metal nanoparticles relative to free diffusion by tuning the trapping wavelength around the particle's resonance [10, 15]. The particles accumulating at the trap site are indirectly monitored by analysing their two-photon fluorescence. This thesis expands current knowledge on optical trapping of metal nanoparticles. We present blue-detuned trapping of 100nm gold spheres by directly observing the particle's interaction with laser light below their resonance wavelength [16]. Furthermore we explore trapping in the infrared with a pulsed trapping laser.

In the first half of this thesis we introduce the theoretical framework and the experimental methods we employed. The relevant theoretical concepts are grouped into forces in optical trapping and optical properties of metal nanoparticles with key material properties such as the polarisability as well as Mie cross sections. We revise common models to describe the plasmon resonance and force calculations and critically examine their validity for our experiments in Chapter 2. In Chapter 3 we describe the setting up of an optical trap. The main focus of this chapter is the imaging of the nanoparticles - a challenging aspect of our experiments as the nanoparticle sizes are below the diffraction limit. We make use of their intrinsic resonance for imaging. We also discuss our detection methods.

The second half of this thesis presents our experimental results. We trap metal nanoparticles on both sides of their plasmon resonance. Chapter 4 discusses red-detuned optical trapping. The trapping laser wavelength is longer than the particle resonance and the nanoparticles are attracted in the high intensity region of a tightly focussed Gaussian beam. We measure the trap stiffness for gold and silver nanoparticles and for various laser powers. In Chapter 5 we investigate the confinement of gold nanospheres within the dark core of a doughnut-shaped beam. We exploit the plasmon resonance to trap a nanoparticle with a blue-detuned laser by using repulsive forces to our advantage.

2 Theoretical foundation

We start this thesis with the theoretical fundamentals before we continue with the experimental part of our work. In order to combine plasmonics and optical trapping we have to merge their respective theoretical concepts to understand the physics in our trapping experiments. We find that we rapidly reach the limits of the models commonly employed in optical trapping: essentially the force decomposition into gradient and scattering force. This chapter intends to guide the reader through the basics of light-metal interactions all the way to force calculations.

The reader is likely to be familiar with established concepts describing light propagation in dielectrics in terms of rays, waves or photons. We are interested in metal-light interactions of nanometer sized silver and gold nanospheres. Therefore we concentrate on classical electromagnetic theory describing light as a wave propagating through media such as dielectrics or metals. Additionally we introduce the concept of a plasmon, a much used expression nowadays, especially in the vibrant field of plasmonics. We present the optical properties of metals, in particular the skin depth and permittivity, to give the reader a good basis for understanding the following in depth discussion about nanoparticle resonances and optical forces.

It is possible to exert a force with light on small objects and particles. Its nature depends on the material of the particle and the applied wavelength of the light source. In this work we are interested in the response of a metal nanosphere to laser light of varying wavelengths, which we chose to model with the quasi-static approximation and Mie theory. Although conceptually completely different, both methods lead to a resonance in the metal nanoparticle's response to incident radiation. At resonance the nanoparticle interacts most intensely with the exciting field. The internal electric charges are driven at a maximum, polarise the particle and result in strong scattering and absorption of the exciting field. At this point we discuss the polarisability α as key concept describing the nanoparticle's resonance.

The first section of this chapter gives a brief introduction to the basics of light propagation in media as well as optical manipulation of matter. In the second section we present two popular approaches describing nanoparticle resonances in terms of the quasi-static approximation and Mie theory. The third section of this chapter is dedicated to the consequences of a plasmonic resonance for optical trapping with respect to the optical forces. Finally, we discuss the applicability of the theoretical findings to our experiment of optically manipulating metal nanospheres.

2.1 Interaction of light with matter

In the simplest case, light interacting with any form of matter results in scattering, reflection and refraction of the incident light field. Additionally certain processes within the material light impinges on can be triggered - resonances are excited, transitions of the fundamental building blocks (electrons, molecules) to other energy levels are introduced and many more. These effects are to a first approximation summarised to the material parameters and we can employ the macroscopic Maxwell equations to describe the propagation of light through matter.

$$\nabla \times \mathbf{E} = -\frac{\partial \mathbf{B}}{\partial \mathrm{t}}, \tag{2.1}$$

$$\nabla \times \mathbf{H} = \frac{\partial \mathbf{D}}{\partial \mathrm{t}} + \mathbf{j}, \tag{2.2}$$

$$\nabla \cdot \mathbf{D} = \rho, \tag{2.3}$$

$$\nabla \cdot \mathbf{B} = 0. \tag{2.4}$$

The field vectors of the electric field $\mathbf{E}$, the electric displacement $\mathbf{D}$, the magnetic induction $\mathbf{B}$ and the magnetic field $\mathbf{H}$ are connected to the charge and current density ρ and $\mathbf{j}$ respectively. We represent all vectors throughout this work as bold variables. To specify the response of the material and describe the interaction between light and matter, we introduce the macroscopic parameters ε_r (relative permittivity) and μ_r (relative permeability). The macroscopic material parameters associate the linear macroscopic response of a bulk medium to the averaged light interaction with the microscopic elements

$$\mathbf{D} = \varepsilon\mathbf{E} = \varepsilon_0\varepsilon_\mathrm{r}\mathbf{E} = \varepsilon_0\mathbf{E} + \mathbf{P}, \tag{2.5}$$

$$\mathbf{B} = \mu\mathbf{H} = \mu_0\mu_\mathrm{r}\mathbf{H} = \mu_0\Big(\mathbf{H} + \mathbf{M}\Big). \tag{2.6}$$

The vacuum permittivity $\varepsilon_0 = 8.854 \times 10^{-12} F/m$ and vacuum permeability $\mu_0 = 4\pi \times 10^{-7} H/m$ are constants and relate to the speed of light in vacuum as $c_0 = \sqrt{1/(\varepsilon_0 \cdot \mu_0)}$. In isotropic, homogeneous matter the permittivity (or dielectric function) ε_r and the permeability μ_r are scalar functions, in anisotropic media ε_r and μ_r are tensors. For metals in particular, $\mu_\mathrm{r} = 1$ and $\varepsilon_r = \varepsilon_1 + i\varepsilon_2$ is a complex function depending on the frequency ω of the incident electromagnetic field. The refractive index of a material $\tilde{\mathrm{n}} = \mathrm{n} + \mathrm{i}\kappa$ is related to the material parameters in the following way

$$\tilde{\mathrm{n}} = \sqrt{\varepsilon_\mathrm{r}\,\mu_\mathrm{r}} = \sqrt{\varepsilon_1 + i\varepsilon_2} \qquad \text{for } \mu_\mathrm{r} = 1 \tag{2.7}$$

$$\varepsilon_1 = \mathrm{n}^2 - \kappa^2 \tag{2.8}$$

$$\varepsilon_2 = 2\mathrm{n}\kappa \tag{2.9}$$

The imaginary part of the material parameters relates to absorption (and heating). All naturally occurring materials have complex material parameters. Depending on the wavelength region considered the imaginary part is often neglected. However, for metals this imaginary part is significant, sometimes even larger than the real part for visible wavelengths. Unless otherwise stated we assume a harmonic time dependence of the monochromatic electromagnetic fields according to

$$\mathbf{E}(\mathbf{r},\mathrm{t}) = \mathbf{E}(\mathbf{r})\mathrm{e}^{-\mathrm{i}\omega\mathrm{t}} \qquad \text{and} \tag{2.10}$$

$$\mathbf{H}(\mathbf{r},\mathrm{t}) = \mathbf{H}(\mathbf{r})\mathrm{e}^{-\mathrm{i}\omega\mathrm{t}} \tag{2.11}$$

in this work. The position coordinates are represented by $\mathbf{r} = (x, y, z)$. The real parts of the fields are obtained by

$$\mathbf{E}(\mathbf{r},\mathrm{t}) = \Re\{\mathbf{E}(\mathbf{r})\mathrm{e}^{-\mathrm{i}\omega\mathrm{t}}\} = \frac{1}{2}\Big[\mathbf{E}(\mathbf{r})\mathrm{e}^{-\mathrm{i}\omega\mathrm{t}} + \mathbf{E}^{*}(\mathbf{r})\mathrm{e}^{+\mathrm{i}\omega\mathrm{t}}\Big] \qquad \text{and} \tag{2.12}$$

$$\mathbf{H}(\mathbf{r},\mathrm{t}) = \Re\{\mathbf{H}(\mathbf{r})\mathrm{e}^{-\mathrm{i}\omega\mathrm{t}}\} = \frac{1}{2}\Big[\mathbf{H}(\mathbf{r})\mathrm{e}^{-\mathrm{i}\omega\mathrm{t}} + \mathbf{H}^{*}(\mathbf{r})\mathrm{e}^{+\mathrm{i}\omega\mathrm{t}}\Big], \tag{2.13}$$

with the star * denoting the complex conjugate.

2.1.1 Polaritons and plasmons

We would like to expand our picture of light propagating through matter as electromagnetic wave and introduce the concept of polaritons and plasmons. This will help to understand some of the mechanisms observed in the experiments presented in this thesis.

When light travels through matter there is more than the transverse electromagnetic wave we know from the light's propagation in vacuum. Light interacts with the building blocks of the material - its atoms and molecules. There are various models describing the complex phenomena of this interaction. Classically the electromagnetic light wave polarises the molecules and atoms it interacts with. These in turn usually slow down the propagation of the electromagnetic wave through medium. From a quantum mechanical point of view the process of light passing a material can be described as photons with certain amount of energy and momentum, which transfer these discrete amounts of energy and momentum to the material. The so produced quantum excitation has its own quantised momentum and energy. Although the phenomena mentioned in this work can all be understood classically [26], it helps to understand certain processes better when we bear the underlying quantum mechanical nature of the problem in mind.

Light-matter interactions may either be described in the so-called weak coupling regime or in the strong coupling limit. The former describes an incident photon

exciting an electron to a virtual state. This model picture is sufficient to understand most mechanisms in dilute media like gases, however it is often not enough to characterise light-matter interaction in solids. In the strong coupling regime the effect of the excited state on the incident field is taken into account in a self-consistent fashion. An optically excited state is now connected with a polarisation $\mathbf{P}$ oscillating with the incident electromagnet field. An oscillating polarisation in turn emits electromagnetic radiation itself that interacts with the incident electromagnetic field. Light travelling through matter is thus always connected to a polarisation wave, which has already appeared in the before mentioned Eq. (2.5):

$$\mathbf{P} = \varepsilon_0\big(\varepsilon_\mathrm{r}(\omega) - 1\big)\mathbf{E} = \varepsilon_0\chi\mathbf{E}. \tag{2.14}$$

In other words, an electromagnetic wave propagating through a medium is not a pure "light wave" but a mix of an electromagnetic wave and a polarisation wave. This holds true throughout the infrared, visible and ultraviolet spectrum for all dense materials such as metals, semiconductors, insulators, liquids and at times even for gases [27]. The susceptibility χ is defined by the relative permittivity $\chi = \varepsilon_r - 1$ and gives a measure how readily a medium polarises in response to an electric field.

Looking at the quantum mechanical description of this process, the polarisation wave may be quantised in the same manner as an electromagnetic wave is quantised with photons as the quanta. The quanta of the polarisation wave are so-called phonons, plasmons or excitons, depending on what parts of matter are actually polarised. Sometimes these quanta are called quasiparticles as they can be attributed an effective mass and other particle-like properties. In metals we commonly find plasmons, the quasiparticles describing the excitation of the free electron gas. A very nice description of a plasmon is presented in Bohren and Huffman's book "Absorption and Scattering of Light by Small Particles" [28]: *"...In the quantum-mechanical language of elementary excitations we refer to the excitation of a plasma oscillation as the creation (or production, or excitation) of a plasmon, the quantum of plasma oscillation [...]. Although a plasmon is made up of electrons, it is not an electron: it is a gang, or collection, of electrons that get together under the urging of the long-range Coulomb force and decide to act in concert. Hence, for the purpose of discussing their behaviour, they may, like an orchestra or a choir, be considered as a single entity following the same (Coulombic) conductor.[...]"*

The mixture of an electromagnetic wave and polarisation wave is called a polariton. Polaritons are a summarised expression for the quasiparticles of light in matter and a mixed state of photons and polarisation wave. The bound state of a plasmon and an electromagnetic wave is correctly termed a plasmon-polariton. In the following a plasmon-polariton is meant when talked about a plasmon to shorten the terminology. Plasmons exist in bulk metal, bound to metal-dielectric interfaces (surface plasmons) and in metal nanoparticles (particle plasmons). In the bulk they are characterised with a dispersion relation. They can even exist independently of light, exited by other mechanisms - electrons for example.

Polaritons are described within a mechanical model of oscillators coupling to the electromagnetic field. These oscillators represent electrons in various energy levels, electron hole pairs or simply entire atoms. The most common model systems of coupled oscillators are the Lorentz and Drude model which we are going to discuss in the next section. The classical mechanics and electrodynamics treatment is sufficient for most scenarios but can easily expanded with quantum mechanical corrections. We continue to name the resonant excitations due to charge oscillations plasmons, even when we do not consider their quantum properties in depth. More details about polaritons and the Lorentz model are discussed elsewhere [26, 27].

2.1.2 Optical properties of metals

One of the first things that comes to mind when thinking of metals is their shiny reflecting surface. Metals reflect visible light. It is also well-known that metals absorb light very well, but are almost transparent for the ultraviolet. The reason for these properties lies in the behaviour of the free conducting electrons upon interaction with light.

Optical properties of materials are compactly fit into the material parameters - the permittivity $\varepsilon_\mathrm{r}(\omega)$ and the permeability $\mu_\mathrm{r}(\omega)$. These values can be experimentally determined or predicted with theoretical models. The fundamental model characterising metals is the Drude-Sommerfeld model [29]. Assuming a free electron gas, the unbound conducting electrons contribute to the optical properties of the material. An applied electric field $\mathbf{E}$ exerts a force on the electrons which obey the equation of motion [29]:

$$\mathrm{m_e}\frac{\partial^2 \mathbf{x}}{\partial \mathrm{t}^2} + \mathrm{m_e}\gamma_\mathrm{c}\frac{\partial \mathbf{x}}{\partial \mathrm{t}} = -\mathrm{e}\mathbf{E} \tag{2.15}$$

The electrons have an effective mass m_e, a charge e and a collision damping frequency γ_c due to electron collisions and scattering events. There is no restoring force as the conducting electrons in metal are not bound to an atom. The electrons perform an oscillatory motion $\mathbf{x}(\mathrm{t}) = \mathbf{x}_0 \mathrm{e}^{-i\omega \mathrm{t}}$ due to the applied field $\mathbf{E}(\mathrm{t}) = \mathbf{E}_0 \mathrm{e}^{-i\omega \mathrm{t}}$. Solving Eq. (2.15) leads to the dielectric function

$$\varepsilon_\mathrm{Drude}(\omega) = 1 - \frac{\omega_\mathrm{p}^2}{\omega^2 + \mathrm{i}\gamma_\mathrm{c}\omega}, \tag{2.16}$$

with the plasma frequency $\omega_\mathrm{p} = \sqrt{n_d e^2/(m_e \varepsilon_0)}$ of the free electron gas and the number density of electrons n_d. This Drude model is sometimes referred to as the high frequency limit of the Lorentz oscillator model [30]. The real part of the dielectric function $\varepsilon_\mathrm{Drude}(\omega)$ is negative below the plasma frequency ω_p. This confirms the well-known metallic properties - light cannot propagate through metal but is reflected and absorbed. Physically the electrons are able to move fast enough

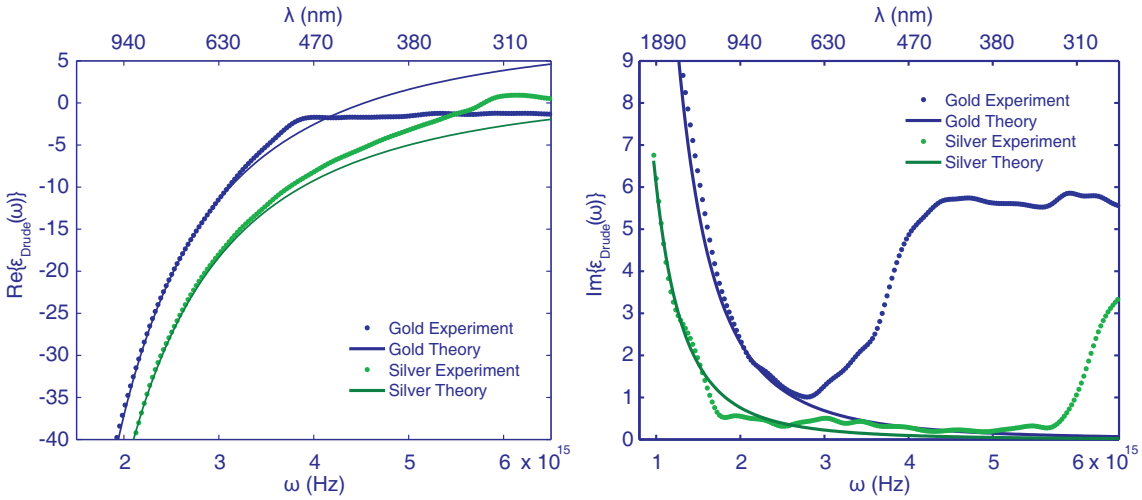

Figure 2.1: *Left* - Comparison of experimentally obtained real part of the permittivity for gold and silver [31] and the theoretical model of a free electron gas (see Eq. (2.17)). *Right* - The calculated imaginary part of the permittivity does not fit the experimental values as well as the real part on the left side. The values used for fitting Eq. (2.17) are $\varepsilon_b = 9$, $\omega_\mathrm{p} = 1.36 \cdot 10^{16}\mathrm{Hz}$ and $\gamma_c = 9.9968 \cdot 10^{13}\mathrm{Hz}$ for gold [32] as well as $\varepsilon_b = 2.5$, $\omega_\mathrm{p} = 1.37 \cdot 10^{16}\mathrm{Hz}$ and $\gamma_c = 3.2258 \cdot 10^{13}\mathrm{Hz}$ for silver [31, 33, 34].

to shield the incident electric field. For even higher frequencies, namely in the ultraviolet, the incident electric field oscillates so fast that the free electrons are not able to follow this high frequency excitation anymore and the metal becomes transparent.

The Drude model is usually extended for noble metals to account for the polarisation effects of the filled d-bands close to the Fermi surface with a so-called background permittivity ε_b

$$\varepsilon_\mathrm{Drude}(\omega) = \varepsilon_b - \frac{\omega_\mathrm{p}^2}{\omega^2 + \mathrm{i}\gamma_c\omega}. \tag{2.17}$$

There are further extensions to Eq. (2.16) approximating the experimental values even better by accounting for interband transitions, the excitation of lower lying bound electrons below the Fermi surface into the conduction band by high energy photons [32]. Qualitatively, the Drude model describes the interactions of electrons in a metal with incoming radiation very well und helps to understand much of the underlying physics. Quantitatively it reaches its limits in the visible spectrum as illustrated in Fig. 2.1. Therefore we stick to the experimental values [31] of the permittivity for the remainder of our calculations.

In addition to the permittivity $\varepsilon_\mathrm{r}(\omega)$ we like to discuss another important material parameter: the skin depth δ. It characterises the penetration depth of the electromagnetic field into the metal. More precisely, at the skin depth the amplitude of

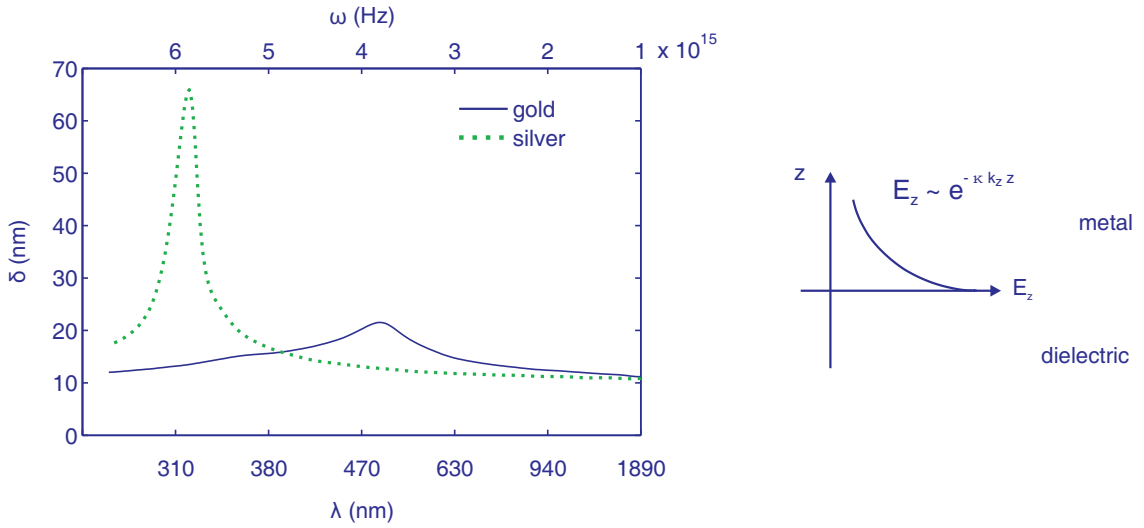

Figure 2.2: *Left* - We compare the skin depth δ in gold and silver for varying wavelength λ and frequency ω. The peak in both curves results from a minimum in the imaginary part of the refractive index κ (see also Eq. (2.20)). The position of the peak is right at the onset of interband transitions which give gold and silver their respective colours. Note that the wavelength scale is not linear. *Right* - This graph symbolises the exponential decay of the electric field penetrating a material in direction z.

the electromagnetic field falls to 1/e of its original value. Beer-Lambert's law states that the transmission of light travelling through a given medium is logarithmically depending on the absorption and length of travel. This dependency is seen clearly when looking at the propagation of a plane wave (in z direction)

$$\mathrm{E}(\omega, \mathrm{z}) = \mathrm{E}_0 \mathrm{e}^{i(k_z z - \omega t)} \tag{2.18}$$

in an attenuating medium such as metal. The wavevector k_z does have a real and an imaginary part due to the complex refractive index of metal $k_z = nk_z + i\kappa k_z$ leading to

$$\mathrm{E} = \mathrm{E}_0 \underbrace{e^{i(nk_z z - \omega t)}}_{\text{oscillation}} \underbrace{e^{-\kappa k_z z}}_{\text{attenuation}} . \tag{2.19}$$

The second part attenuates the wave the further it penetrates into the metal. The energy density of the electric field is proportional to the square of its time average and gives together with $k_z = \omega/c$ the equation for the skin depth

$$\delta = \frac{\lambda}{4\pi\kappa}, \tag{2.20}$$

with the imaginary part of the refractive index $\kappa = \Im\{\tilde{n}\}$. Sometimes this is also called the penetration depth. There are slightly different definitions depending on

whether the amplitude or the intensity of the electromagnetic wave decreased to 1/e of its original value. Eq. (2.20) refers to the intensity or energy density.

For metals the skin depth is not a constant but changes with wavelength (or frequency) because of the wavelength dependence of the material parameters. The gold and silver nanoparticles we used for our experiments described in the following chapters were 60, 80 and 100nm in diameter. Looking at Fig 2.2 suggests that the skin depth is 12nm for silver and 12-22nm for gold throughout the visible spectrum. Thus we cannot assume our nanoparticles to be entirely penetrated by a homogeneous electric field. Consequently only the outer shell of our nanoparticles contributes to the polarisation of the sphere, the inside of the sphere is shielded from the incident electric field. We discuss the polarisability of a sphere in more detail in Sec. 2.2.

2.1.3 Optical manipulation of matter

We introduce the basic concepts of optical trapping in general before we continue with the optical manipulation of metal nanoparticles in particular. In this section we provide an illustrative explanation which allows the reader to get familiar with the principles of optical trapping. The ideas presented here are adequate to explain optical manipulation of atoms or large dielectric spheres. Their applicability to our experimental situation as well as the exact mathematical terms are discussed later in a special section on optical forces (Sec. 2.3). A more extensive introduction to optical trapping is available elsewhere [1, 2, 8].

Light carries momentum. Upon interaction with matter light may change its direction as a result to scattering or refraction. This induces a momentum transfer from light to the object in its pathway. According to Newton's second law, the change of momentum p of light results in a force being applied $\mathrm{F} = \frac{\partial \mathrm{p}}{\partial \mathrm{t}}$. The magnitude of the force depends upon the power of the incident light as well as the refractive index difference between the object and the host medium. This force is in the femto-Newton regime and thus not apparent in everyday life. However for microscopic objects femto-Newtons are significant and we are thus able to observe the force exerted upon microscopic objects by light.

In general there are two size regimes considered and used for explaining the fundamentals of optical trapping: the Rayleigh regime and the ray optics regime (see also Fig. 2.3). The ray optics model describes optical trapping for large sized transparent spheres with a radius r much larger than the wavelength of the trapping laser ($\mathrm{r} \gg \lambda$), such that we work within the geometrical optics limit. The Rayleigh regime is applicable to objects much smaller than the trapping wavelength with their radius r $\ll \lambda$. The size regime in between with $\mathrm{r} \simeq \lambda$ is the Mie regime where all experiments described in this thesis take place.

With reference to Fig. 2.4 we are able to explain how optical trapping works with ray optics alone. Let us assume a transparent dielectric sphere several microns in

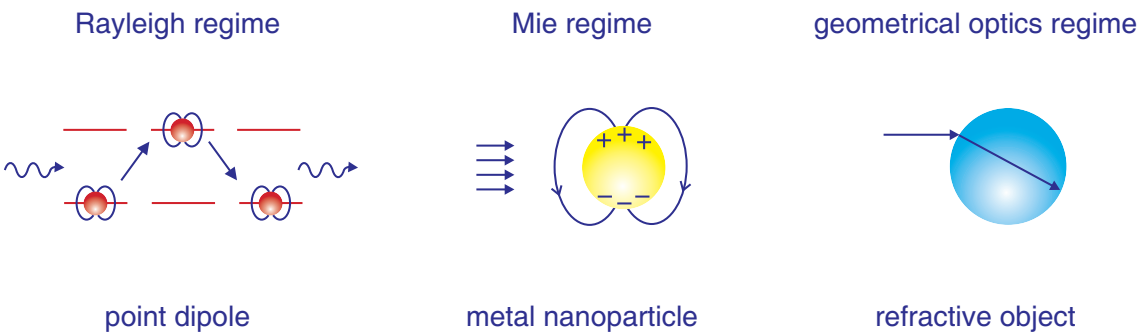

Figure 2.3: The graph illustrates the different size regimes of trapped objects with respect to the trapping wavelength. The Rayleigh regime is applicable to particles with a radius r much smaller than the trapping wavelength $r \ll \lambda$ such as atoms. The geometrical optics regime encompasses large transparent spheres, several microns in diameter, such that we are able to employ ray optics ($r \gg \lambda$). The size regime in between with $r \simeq \lambda$ is the so-called Mie regime and includes the metal nanoparticles discussed in this thesis.

diameter being passed by light rays. Light passing the sphere off-centre will always be refracted causing the light ray to change its direction and momentum. Because of Newton's third law *actio=reactio* the force exerted on the sphere is in opposite direction causing the sphere to be pulled towards the ray of light. This may seem counter-intuitive at first, yet forms the main principle of optical manipulation. Describing a laser beam possessing a Gaussian intensity profile with differently weighted light rays allows to model real experimental conditions. So if high intensity light rays pass the sphere off axis their force component acting on the sphere is dominant. Consequently the sphere is pulled in the centre of the high intensity region of the beam. This way we achieve two dimensional trapping in the plane perpendicular to the propagation direction of the beam.

Focussing this beam tightly allows us to trap an object in three dimensions as pictured on the right hand side in Fig. 2.4. The sphere is pulled towards the focus. The light rays come from above and are able to lift the sphere up in opposite direction of light propagation. Reversing the direction of the light rays does not change the direction of the force exerted on the sphere as it depends only on the intensity gradient of the beam rather than its propagation direction. Here we only describe the force resulting from refraction by changing the direction of the rays. This is commonly referred to as gradient force F_{grad}. The force arising because of reflection from the sphere, so-called scattering force F_{sct}, also occurs. It acts in direction of the propagation of light and destabilises the trap. In order to trap an object, the gradient force always has to overcome the scattering force ($F_{grad}/F_{scat} > 1$) [17]. The complete mathematical description of trapping forces in the ray optics regime is presented in [35].

The photon model helps to understand how light exerts a force on a Rayleigh ob-

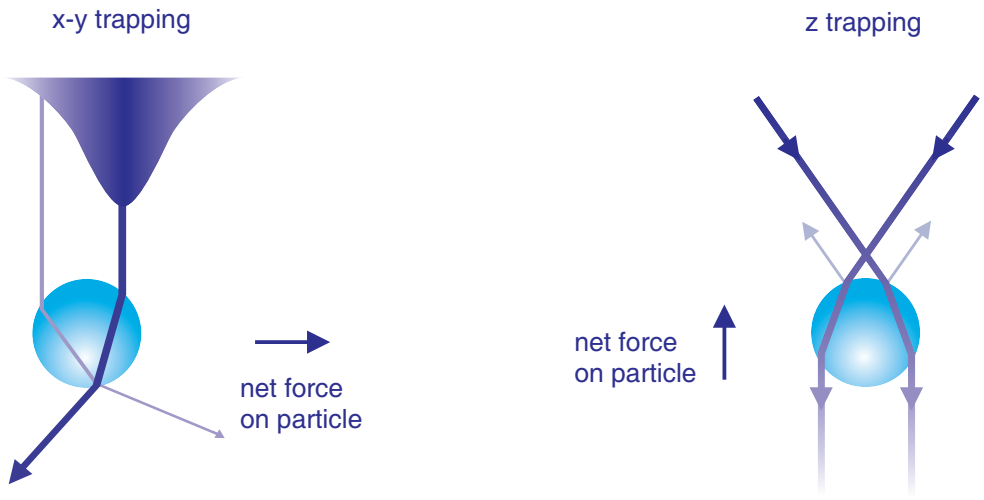

Figure 2.4: *Left* - This sketch illustrates optical trapping in two dimensions with ray optics. The sphere is trapped in the plane perpendicular to the propagation axis of the light rays. Refraction changes the direction of the light rays which results in a momentum transfer and force acting upon the sphere. Weighting light rays differently allows us to simulate a Gaussian beam profile. *Right* - Optical trapping in three dimensions is achieved by focussing the beam tightly which results in an upward motion of the sphere towards the focus of the beam. Reversing the direction of the light rays does not change the direction of the force on the sphere as the latter only depends on the intensity gradient of the light.

ject. Each photon colliding with a particle either interacts elastically or inelastically. In the elastic case the photon transfers all or parts of its linear momentum to the particle and is thus able to change the direction of travel of the particle before continuing on its own path. In the inelastic case, the photon is absorbed transferring its complete momentum to the particle. As we mentioned before the change of momentum p of the photon leads to a force $F = \frac{\partial p}{\partial t}$ applied to the particle. Optical trapping of atoms is typically explained within the Rayleigh regime. They are described as point like dipoles that absorb and re-radiate light. Historically atom trapping was demonstrated at the same time as optical trapping of larger micron-sized dielectric spheres. We refer the reader to [36, 37] for further information on atom trapping.

For calculating the forces occurring in optical trapping of Rayleigh particles we typically consider light within classical electrodynamics as opposed to quantum mechanics for atom trapping. Assuming the trapped particle in the Rayleigh regime (typically $r \ll \lambda/20$) we are able to treat it as a point-like dipole. The electromagnetic field of the incident trapping laser remains constant over the extend of the entire particle. As for the ray optics model we separate the force into gradient and scattering force [17] as

$$F_{grad} = \frac{n_{host}^3 r^3}{2}\left(\frac{m^2-1}{m^2+2}\right)\nabla(|E|^2) = \frac{n_{host}}{2}\alpha\nabla(|E|^2), \tag{2.21}$$

$$F_{scat} = \frac{I_0}{c}\frac{128\pi^5 r^6}{3\lambda^4}\left(\frac{m^2-1}{m^2+2}\right)^2 n_{host}. \tag{2.22}$$

We used n_{host} to denote the refractive index of the host medium, $m = n_{sphere}/n_{host}$ for the relative refractive index, I_0 for the beam's intensity and λ as wavelength of the incident radiation. In Eq. (2.21) we summarised some terms as the polarisability α, an important quantity we are going to discuss in detail later on (see Sec. 2.2.2). In order to achieve a strong gradient force F_{grad} for trapping the particle it is important to increase the intensity gradient. Simply adjusting the laser intensity also increases the scattering force F_{scat} and does not necessarily lead to 3D trapping.

The presented models help to understand the basic principles of optical trapping. However, they do not explain every aspect of it. Especially optical trapping of metal nanoparticles as discussed in this thesis is challenging to position within the common models. Ray optics completely fails us, not only because of the size of our metal nanoparticles, which is comparable to the laser's wavelength, but also the material. Metal is not transparent for visible light and we cannot argue with refraction of beams. Applying the point dipole model as described has its own challenges. Contrary to a dielectric sphere, where the individual point dipoles of many composing atoms and molecules can be added up, a metal sphere presents a totally different physical system. Here the conducting electrons of the metal strongly interact with each other; they are not fixed to a position and thus respond collectively to the incoming field. The ideas of scattering and gradient forces remain, calculating the polarisability however is different. In addition we have to take absorption into account which is also present for dielectrics also but does not play such a prominent role as for metals.

Note that for dielectrics the refractive index of the trapped object is the distinctive material parameter for force calculations. Metals are commonly described with their permittivity ε to calculate particle properties. Of course these quantities are interchangeable but it is more appropriate to use ε for metals rather than their refractive index. We show in subsequent sections how to calculate the polarisability α of a metal particle which also relies on its permittivity ε. We return to the force analysis at the end of this chapter once we discussed spherical metal nanoparticles and their interaction with light.

2.2 Spherical metal nanoparticles

All experiments conducted in this work expose gold or silver nanoparticles to laser light. The diameter of these particles ranges from 60nm-100nm which is smaller but still comparable to the applied wavelength of the electromagnetic field (400-1000nm). Metal nanoparticles sustain localised plasmon resonances bound to the particle. Close to resonance the material properties and consequently the interaction

between metal nanoparticles and the incident light changes dramatically. The effect of the metal nanoparticle's resonance on the forces exerted by light of different wavelengths is our main subject of study (see Chapters 4 and 5 for our experimental findings). A resonance is an amplified response of the resonant system to a periodic excitation at specific frequencies. For metal nanoparticles the oscillating system is the electron plasma within the metal sphere that is excited by the incoming electric field. The size and material of the sphere determine the position of the resonant frequencies.

After a brief definition and illustrative introduction of the particle plasmon we show how to calculate the particle plasmon resonance for spheres following the two most popular approaches. The first method, the quasi-static approximation, introduces the polarisability of the particle as key concept by analysing the charge distribution of a sphere in an electric field. The second method is the well-known Mie theory, including electromagnetic fields interacting with the metal nanoparticle. The resonance appears in the response of the particle in form of a different field distribution. Both methods quantise the particle plasmon resonance: one in terms of the polarisability, the other in the form of cross sections. We demonstrate how to relate these quantities to each other. In the final part of this section, we critically examine the applicability of the presented methods to our experiments.

2.2.1 The Particle Plasmon

The particle plasmon resonance of tiny gold and silver spheres is located in the visible rendering these metal nanoparticles brightly coloured upon excitation. This can be achieved with normal daylight - a laser is not necessarily needed. Centuries ago our ancestors already used these physical properties by melting gold and silver in glass leading to tiny metal inclusions that give the glass a bright permanent colour that does not bleach nor cease. These colourful glasses were often used in church windows. Nanoparticle-doped glass may look different in reflection or transmission. If the included gold nanoparticles are large enough to scatter green predominantly, the glass will look green in reflection or at an angle. In transmission however the glass is looking red as all green light has already been scattered out of the beam path. The colours of metal nanoparticles are a result of absorption and scattering of the incident light. Scattering is more pronounced than absorption for larger particles as we illustrate in Sec. 2.2.3. We observed these distinct colours of various nanoparticles in our experiment by viewing them in a special form of illumination described in Sec. 3.3.

Light scattering on metal nanoparticles or interaction with the plasmon is an elastic process. Free electrons in the metal react to the incident light, responding strongly close to resonance due to increased scattering and polarisation of the particle. The particle plasmon is a localised mode of the electron oscillations and thus a bound quasi-particle. It has no dispersion relation and does not propagate. Particle

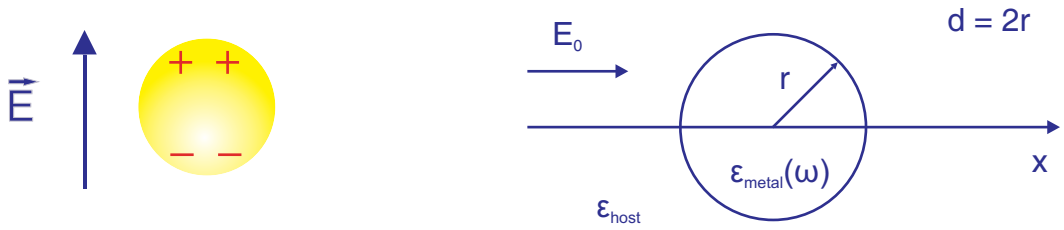

Figure 2.5: *Left* - This sketch symbolises the response of a metal sphere to an electrostatic field $E_0\hat{\mathbf{x}}$. *Right* - This diagram of a metal sphere exposed to an electrostatic field $E_0\hat{\mathbf{x}}$ defines the variables of our problem: the incoming electric field E_0, the radius r of the sphere, the permittivity of the host ε_{host} and metal $\varepsilon_{metal}(\omega)$.

plasmons have different symmetry properties than surface plasmons. It is possible to couple light directly to a particle plasmon as the spherical symmetry does not require the same stringent wavevector matching conditions as its surface plasmon counterpart. Since the transverse momentum is not conserved in this spherical geometry, a particle plasmon exhibits a distinct resonance frequency (unlike to its surface counterpart exhibiting a broad spectrum) depending on its size, shape and material.

The plasmon resonance enhances both the field inside the particle at resonance and the surrounding near field of the sphere. Similarly to surface plasmons the excitation encounters losses. As particle plasmons do not propagate these are not characterised by a propagation length but rather a decay of the particle plasmon over time. The main loss mechanisms are a radiative decay process into photons and absorption which we discuss in more detail in Sec. 2.2.4.

2.2.2 Quasi-static approximation

The plasmon resonance manifests itself in various physical quantities. First we introduce is the polarisability α - a very important quantity for optical trapping. The polarisability is the principal material parameter in the dipole force description (see Sec. 2.3) and will be referred to a lot later on. The quasi-static approximation determines the polarisability α of a particle by reducing it to a dipole interacting with a homogeneous electric field. The polarisability characterises the entire system as it combines the material parameters of the particle and the surrounding medium. The quasi-static approximation is a good starting point to estimate the position of the resonance of metal nanoparticles. It gives a quick and simple access to the polarisability α and thus the response of the particle in the field. This explains the popularity of the quasi-static approximation as it is employed almost exclusively for optical trapping of metal nanoparticles [7, 9, 10, 13, 14, 16, 25, 38].

Due to the incident electromagnetic field, the conducting electrons of the metal sphere experience a force. The sphere is charged and, when it is small enough,

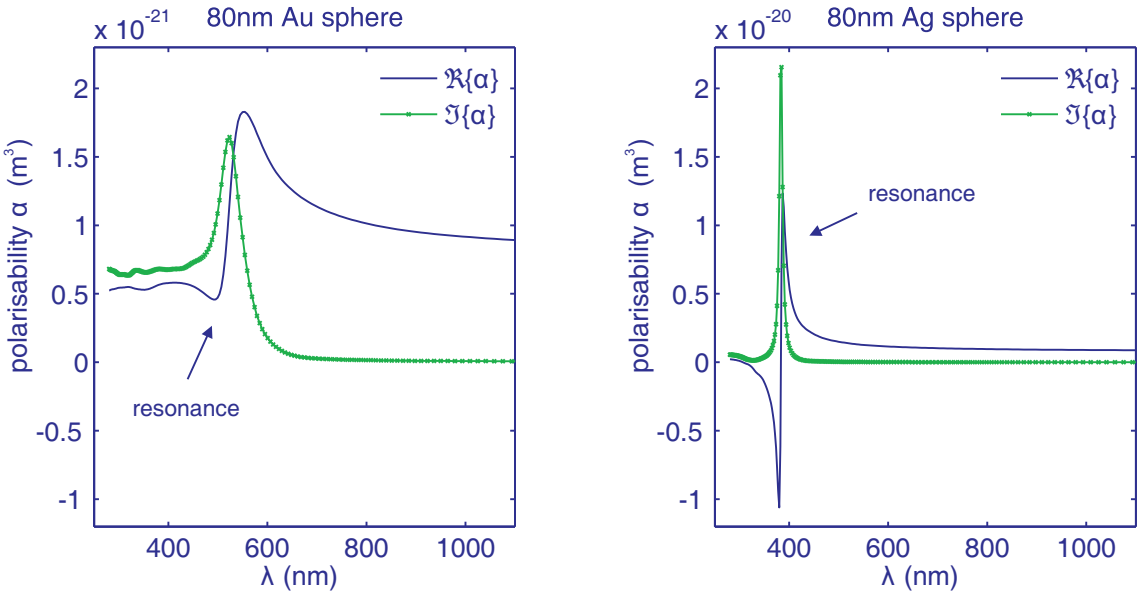

Figure 2.6: *Left* - We calculated the real and imaginary part of the polarisability α for a 80nm gold sphere in water according to Eq. (2.24). *Right* - The resonance appearing in the real and imaginary part of α for a 80nm silver sphere in water is much narrower and stronger than the one for gold. This property stems from the material parameters of the different metals with gold exhibiting more intrinsic damping than silver. The position of the resonance is at 554nm for gold and at 385nm for silver. Note the different size scale for silver and gold.

resembles a dipole with a negative charge on one side and a positive charge on the other side (see Fig 2.5). The quasi-static approximation assumes that the diameter d of the nanoparticles is much smaller than the incoming wavelength λ. In this limit the incoming field is constant over the particle's extent and the problem can be solved using a static electric field $\mathbf{E} = \mathrm{E}_0\hat{\mathbf{x}}$ (see Fig 2.5). The time dependence $\mathrm{e}^{-i\omega t}$ is easily added on after solving the problem first. It turns out that in first approximation the field inside the metal sphere is homogeneous and the scattered field is the field of a dipole oscillating at the centre of the metal sphere. The dipole moment of the metal nanoparticle is thus

$$\mathbf{p} = 4\pi\varepsilon_0\varepsilon_{\mathrm{host}}\mathrm{r}^3\frac{\varepsilon_{\mathrm{metal}}(\omega)-\varepsilon_{\mathrm{host}}}{\varepsilon_{\mathrm{metal}}(\omega)+2\varepsilon_{\mathrm{host}}}\vec{\mathrm{E}_0}. \tag{2.23}$$

Summarising Eq. (2.23), according to $\mathbf{p} = \varepsilon_0\varepsilon_{\mathrm{host}}\alpha\vec{\mathrm{E}_0}$, leads to an expression for the polarisability α of the metal nanoparticle

$$\alpha \;=\; 4\pi\mathrm{r}^3\frac{\varepsilon_{\mathrm{metal}}(\omega)-\varepsilon_{\mathrm{host}}}{\varepsilon_{\mathrm{metal}}(\omega)+2\varepsilon_{\mathrm{host}}} \;=\; 3\mathrm{V}\,\frac{\varepsilon_{\mathrm{metal}}(\omega)-\varepsilon_{\mathrm{host}}}{\varepsilon_{\mathrm{metal}}(\omega)+2\varepsilon_{\mathrm{host}}}, \tag{2.24}$$

with the volume V of the sphere, its complex permittivity $\varepsilon_{\mathrm{metal}}$ and the permittivity

of the surrounding medium $\varepsilon_{\text{host}}$. Eq. (2.24) is often referred to as Clausius-Mossotti equation. A more detailed derivation of the dipole moment may be found elsewhere [26, 30, 32].

The Clausius-Mossotti approximation (Eq. (2.24)) enables us to characterise the response of a sphere to an incident electric field by calculating α for different frequencies ω, or wavelengths λ respectively. This is the simplest method to determine the position of the resonance of a metal nanoparticle. Within this approach the resonance position depends upon the material of the particle only. Red-shifting of the resonance due to an increased particle size is not included in this model as the volume of the particle is only a prefactor in Eq. (2.24) and the permittivity of the sphere is the wavelength dependent variable. We calculated the real and imaginary part of the polarisability α for a silver and a gold sphere with $d = 80\text{nm}$; these are plotted in Fig. 2.6. The plasmon resonance appears clearly as peak in the real and imaginary part of α. The real part of the polarisability α is a key factor in the gradient force calculations we discuss in Sec. 2.3. However straightforward it is to calculate α, there is no easy way of measuring this quantity directly as one would have to determine the charge distribution of the entire metal sphere upon light excitation.

2.2.3 Mie theory

Mie theory is the most popular method to analyse the absorption and scattering by a sphere. The following is a short summary of the derivation which is presented in more detail elsewhere [28]. Figure 2.7 shows a sketch of the system considered in the following. Starting with the wave equation originating from Maxwell's equations (Eq. (2.1)-(2.4))

$$\nabla^2\mathbf{E} - \frac{1}{\mathrm{c}^2}\frac{\partial^2\mathbf{E}}{\partial \mathrm{t}^2} = 0, \tag{2.25}$$

for the electromagnetic field ($\mathbf{E}$,$\mathbf{H}$) and its speed in medium

$$\mathrm{c} = \frac{\mathrm{c}_0}{\mathrm{n}} = \frac{1}{\sqrt{\varepsilon_0\,\varepsilon_\mathrm{r}\cdot\mu_0\,\mu_\mathrm{r}}} \qquad \text{with} \qquad \mathrm{c}_0 = \frac{1}{\sqrt{\varepsilon_0\mu_0}} = \mathrm{c}_0 = 2.998\times10^8\frac{\mathrm{m}}{\mathrm{s}}, \tag{2.26}$$

this vector problem is reduced to the scalar wave equation $\nabla^2\Psi + \mathrm{k}^2\Psi$ in spherical coordinates for the function Ψ

$$\frac{1}{\mathrm{r}^2}\frac{\partial}{\partial \mathrm{r}}\left(\mathrm{r}^2\frac{\partial\Psi}{\partial \mathrm{r}}\right) + \frac{1}{\mathrm{r}^2\sin\theta}\frac{\partial}{\partial\theta}\left(\sin\theta\frac{\partial\Psi}{\partial\theta}\right) + \frac{1}{\mathrm{r}^2\sin^2\theta}\frac{\partial^2\Psi}{\partial\Psi^2} + \mathrm{k}^2\Psi = 0 \tag{2.27}$$

The scalar function Ψ is used to reconstruct the vector fields afterwards. All fields are assumed to be time-harmonic ($\mathrm{e}^{i(\mathbf{kr}-\omega\mathrm{t})}$). The wavevector k in medium is defined as

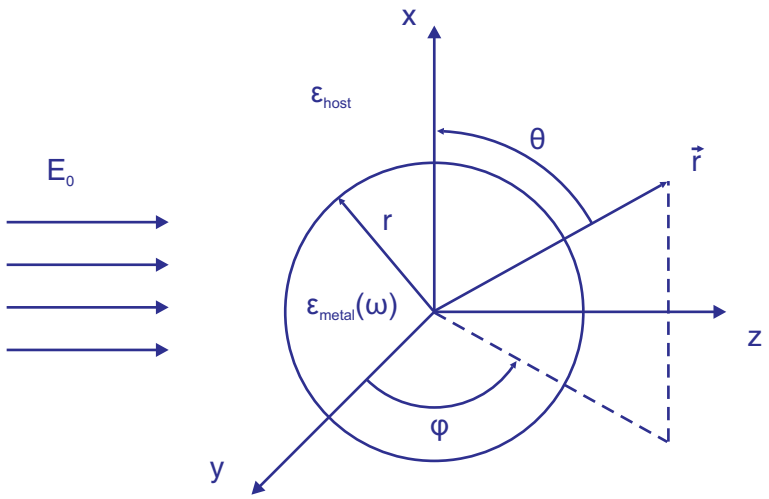

Figure 2.7: Sketch of the scattering problem of a sphere with radius r in spherical coordinates r, θ and ϕ. The incoming electric field E_0 and the permittivity of the host ε_{host} and metal $\varepsilon_{metal}(\omega)$ are indicated as well.

$$\mathrm{k} = \frac{\omega}{\mathrm{c}} = \omega\sqrt{\varepsilon\mu} = \omega\sqrt{\varepsilon_0\varepsilon_\mathrm{r}\mu_0\mu_\mathrm{r}}. \tag{2.28}$$

Expanding a plane wave in spherical harmonics and inserting it in Eq. (2.27) gives expressions for the scattering coefficients $\mathrm{a_n}$ and $\mathrm{b_n}$ that are the expansion coefficients for the plane wave in spherical harmonics:

$$\mathrm{a_n} = \frac{\mathrm{m}\Psi_\mathrm{n}(\mathrm{mx})\Psi'_\mathrm{n}(\mathrm{x}) - \Psi(\mathrm{x})\Psi'_\mathrm{n}(\mathrm{mx})}{\mathrm{m}\Psi_\mathrm{n}(\mathrm{mx})\xi'_\mathrm{n}(\mathrm{x}) - \xi_\mathrm{n}(\mathrm{x})\Psi'_\mathrm{n}(\mathrm{mx})}, \tag{2.29}$$

$$\mathrm{b_n} = \frac{\Psi_\mathrm{n}(\mathrm{mx})\Psi'_\mathrm{n}(\mathrm{x}) - \mathrm{m}\Psi(\mathrm{x})\Psi'_\mathrm{n}(\mathrm{mx})}{\Psi_\mathrm{n}(\mathrm{mx})\xi'_\mathrm{n}(\mathrm{x}) - \mathrm{m}\xi_\mathrm{n}(\mathrm{x})\Psi'_\mathrm{n}(\mathrm{mx})} \tag{2.30}$$

with the relative refractive index $\mathrm{m} = n_{metal}/n_{host}$, the size parameter $x = 2\pi r n_{host}/\lambda$ and the Riccati-Bessel functions $\Psi_n(r) = r j_n(r)$ and $\xi_n(r) = r h_n^{(1)}(r)$. It follows that the required scattering and extinction cross sections are

$$\mathrm{C_{scat}} = \frac{2\pi}{\mathrm{k}^2}\sum_{\mathrm{n=1}}^{\mathrm{inf}}(2\mathrm{n}+1)(|\mathrm{a_n}|^2 + |\mathrm{b_n}|^2), \tag{2.31}$$

$$\mathrm{C_{ext}} = \frac{2\pi}{\mathrm{k}^2}\sum_{\mathrm{n=1}}^{\mathrm{inf}}(2\mathrm{n}+1)\Re\{\mathrm{a_n} + \mathrm{b_n}\}. \tag{2.32}$$

The absorption cross section is obtained using the following relationship [28]

$$C_{ext} = C_{abs} + C_{scat}. \tag{2.33}$$

Extinction is thus defined as the sum of scattering and absorption. Depending on the size of the metal nanoparticle either scattering or absorption is the dominant mechanism. For larger spheres, scattering is more pronounced than absorption as shown in Fig. 2.9. It is sometimes useful for comparison to use the scattering and absorption efficiencies instead of the cross sections as the former are normalised with respect to the sphere's surface area

$$Q_{scat} = \frac{C_{scat}}{\pi a^2}, \tag{2.34}$$

$$Q_{abs} = \frac{C_{abs}}{\pi a^2}. \tag{2.35}$$

The peak of the efficiencies, so therefore the peak of the plasmon resonance, shifts towards the red (lower frequencies) with increasing particle size. In Fig. 2.9 the peak of the scattering efficiency shifts from 541nm over 559nm to 579nm for a 60nm, 80nm and 100nm sized gold sphere in water. The numerical values of the cross sections can be determined using software such as Mathematica for example.

2.2.4 Results and discussion

In the two preceding sections we presented the two most common approaches to describe and calculate the resonance of metal nanoparticles. We are now comparing their validity, in particular with respect to our real experimental situation.

The quasi-static approximation holds true in the Rayleigh regime when $d \ll \lambda$. This condition is often generously stretched and even 100nm spheres exposed to 1064nm laser light are considered within this limit. For dielectric particles without plasmonic resonances this approach is most likely justified. However for metal nanoparticles we have to employ this approach with caution. The position of the resonance shifts towards the red (longer wavelengths) for particles beyond the Rayleigh regime, which is not taken into account by the quasi-static approximation. There has been a suggestion to improve the result of the polarisability description for larger spheres by accounting for the bigger volume [7], but this gives only a size factor in the strength of the resonance and does not account for the red-shifting.

We illustrate the main shortcoming of the quasi-static approximation in Fig. 2.8. Despite the increase in particle size, the peak of the polarisability and thus the resonance remains at the same wavelength position. In reality, the resonance shifts to longer wavelengths and broadens for larger particles. The quasi-static model does not account for the interaction of the scattered field with the particle itself. This is only achieved when the problem of the oscillating dipole is solved in a self-consistent fashion. The quasi-static model also neglects retardation effects and thus

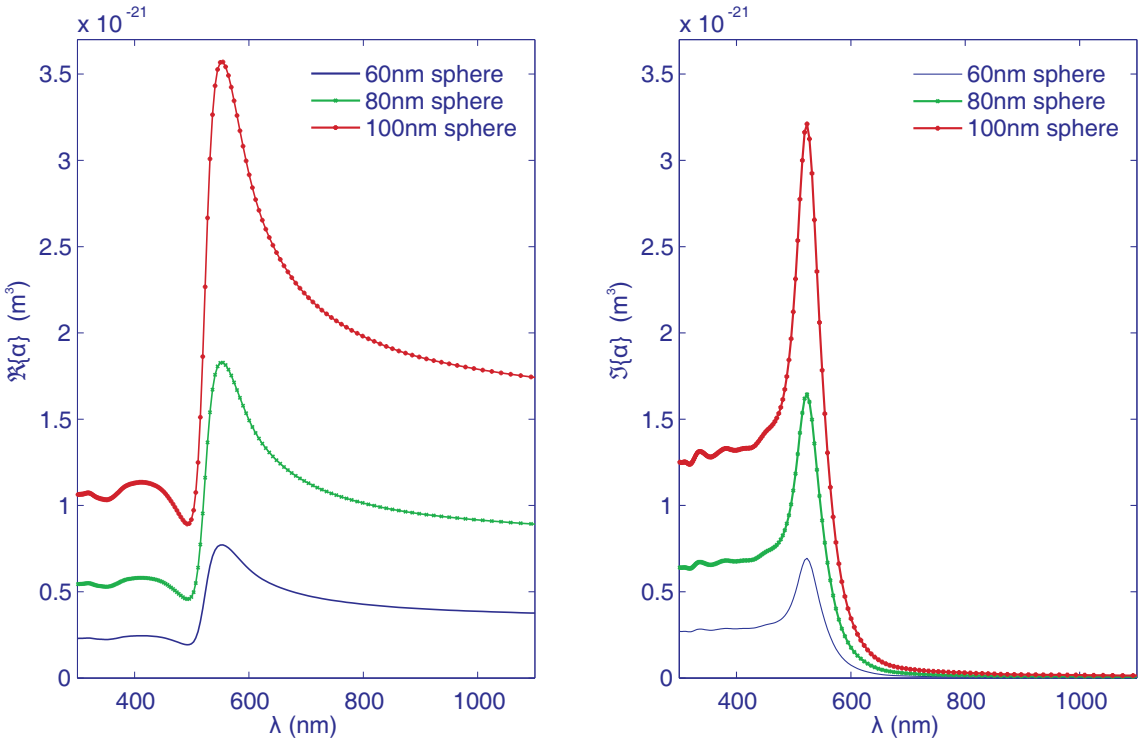

Figure 2.8: *Left* - To highlight the main shortcomings of the quasi-static approximation we calculated the real part of the polarisability $\Re\{\alpha\}$ for gold spheres of 60nm, 80nm and 100nm diameter with the Clausius-Mossotti equation (Eq. (2.24)). We see that the resonance only increases in magnitude and does not broaden nor shift towards longer wavelengths as it does in reality. *Right* - The same effect appears in the imaginary part of the polarisability $\Im\{\alpha\}$: there is no shift of the resonance for increasing particle sizes.

all electrons are deemed to respond simultaneously to the incoming electromagnetic field. The retardation of the exciting and the depolarisation field inside the particle cause the red-shift of the resonance for larger particles [26,39]. Increasing the particle volume results in a larger distance between the charges at opposing interfaces of the particle. The restoring force of the system is therefore reduced which lowers the resonance frequency.

In addition to the losses in the metal itself (see Sec. 2.1.2), the particle plasmon exhibits its own loss mechanism leading to the broadening of the plasmon resonance. The main loss mechanism of the dipolar plasmon resonance is radiation damping. The coherent electron oscillations are able to decay directly into photons. This effect increases for larger particles and thus broadens the resonance with increasing particle size [40, 41].

The broadening and red-shifting of the resonance is nicely illustrated in Fig. 2.9 where we calculated the scattering cross section with Mie Theory. It is not a higher order multipole effect but present for each resonance (dipolar, quadrupolar,..) it-

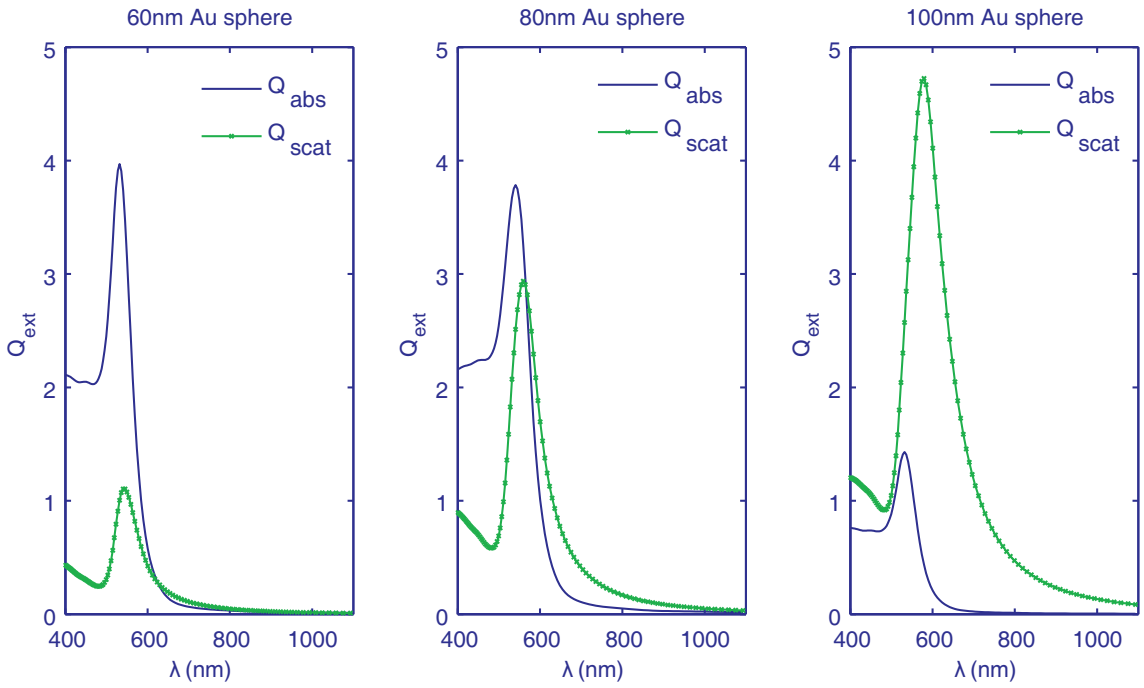

Figure 2.9: The scattering efficiency Q_{scat} (green) increases significantly over the absorption efficiency Q_{abs} (blue) for larger gold nanoparticles. Additionally the resonance peak shifts towards longer wavelengths for larger particles and broadens.

self [39]. In addition to the strictly dipolar resonance of a 20nm silver sphere, we see higher order resonance first appearing in the absorption cross section for larger particles (plotted in Fig. 2.10). The quadrupolar resonance also appears in the scattering cross section for even larger particles. Higher order resonances do not appear in the Clausius-Mossotti equation at all. The quasi-static approximation is by definition a dipolar approximation, higher order resonances are not accounted for.

Nevertheless, the quasi-static approximation presented in Sec. 2.2.2 is used very frequently in optical trapping to predict and describe the strength of the trapping force (see Sec. 2.3.2). As we can see from Mie theory, the quasi-static approximation is not a good model for the commonly trapped particle sizes. But it provides a value for the polarisability α that is inserted directly in the gradient force expression as we are going to show in Sec. 2.3.2. This seems to explain the popularity of the model [7, 9, 10, 13, 14, 16, 25, 38].

Even though Mie theory does not provide the polarisability α directly there is a way to retrieve this parameter from the cross sections, provided some conditions are fulfilled. This method is also an approximation for a dipole in an electric field varying in space and time. Here we take the interaction of the scattered field with the sphere itself into account as Mie solves the problem in a self-consistent fashion. Although this method provides again only a solution to the limit where the particle

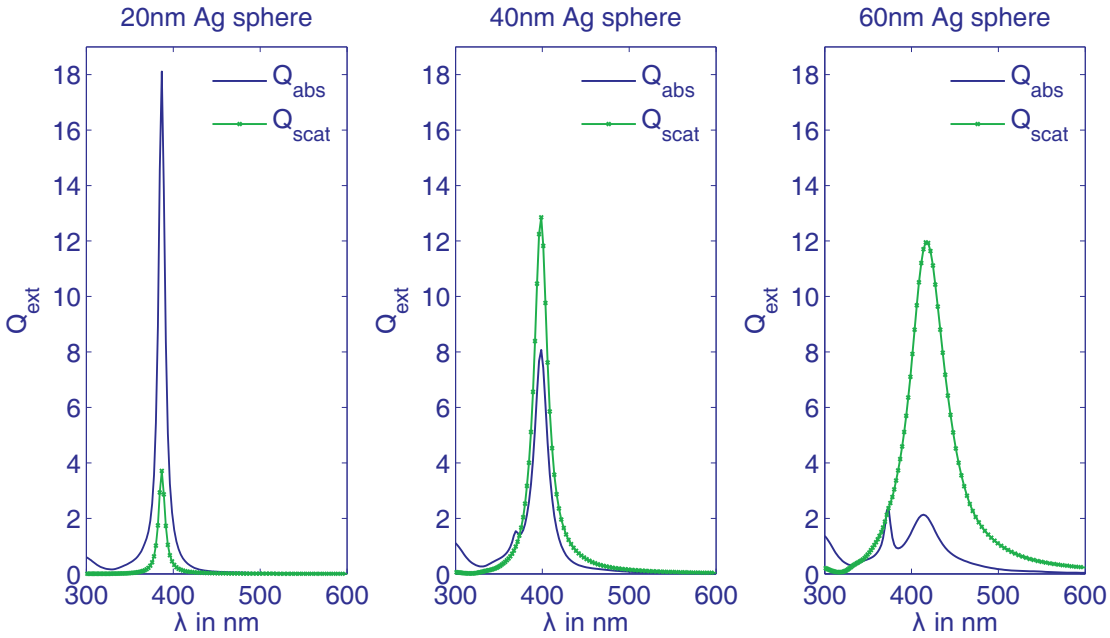

Figure 2.10: Contrary to the quasi-static approximation, the resonance of the scattering and absorption efficiency calculated with Mie theory (Eq. (2.34)-(2.35)) broadens and redshifts for spheres with increasing diameter. As mentioned in Sec. 2.2.3, the scattering dominates over absorption for larger particles. Higher order resonances show up first in the absorption efficiency and appear in the scattering efficiency only for larger particles (in this case for a 80nm silver sphere).

is small compared to the incident wavelength, we now take the broadening and redshifting of the resonance into account. When the size parameter $x = 2\pi r n_{host}/\lambda$ is $x \ll 1$ and the product with the absolute value of the relative refractive index fulfils $|\mathrm{m}|x \ll 1$, the scattering and absorption cross section are written as

$$\mathrm{C_{abs}} = \mathrm{k_{host}} \cdot \Im\{\alpha\} = \mathrm{k_{host}}\alpha'', \tag{2.36}$$

$$\mathrm{C_{scat}} = \frac{\mathrm{k_{host}^4}}{6\pi}|\alpha|^2 = \frac{\mathrm{k_{host}^4}}{6\pi}(\alpha'^2 + \alpha''^2) \tag{2.37}$$

$$\text{with} \quad \alpha = \alpha' + \imath\alpha'' \qquad \text{and} \qquad \mathrm{k_{host}} = \frac{2\pi \mathrm{n_{host}}}{\lambda_0}. \tag{2.38}$$

Reordering Eq. (2.36) - (2.37) leads to an expression for the real and imaginary part of the polarisability expressed in terms of the cross sections

$$\alpha' = \pm\sqrt{\frac{6\pi \mathrm{C_{scat}}}{\mathrm{k_{host}^4}} - \frac{\mathrm{C_{abs}^2}}{\mathrm{k_{host}^2}}}, \tag{2.39}$$

$$\alpha'' = \frac{\mathrm{C_{abs}}}{\mathrm{k_{host}}}. \tag{2.40}$$

However, the sign of the real part of the polarisability is not unambiguously defined in this approach. For some metal nanoparticles, $\Re\{\alpha\}$ is negative in certain regions of the spectrum, more precisely below the resonance wavelength. In that situation we would have to take the negative square root in Eq. (2.39). But there is no strict rule when to chose which sign, making the whole approach rather ad hoc.

A precise determination of the sign via Kramers-Kronig relations proves difficult because of the following argument: The range over which we are able to obtain values for α, in particular for the imaginary part $\Im\{\alpha\}$, is determined by the range of values we have for the permittivity of the metal. Theoretically these can be calculated for $\omega = 0 \rightarrow \infty$, however as discussed in Sec. 2.1.2 the Drude model does not model the real metal's behaviour across the entire spectrum and we have to divert back to experimental values [31]. These are not given for the complete range $\omega = 0 \rightarrow \infty$ and thus the Kramers-Kronig relations cannot be applied as they require a function to be defined for $\omega = 0 \rightarrow \infty$, or at least starting from $\omega = 0$. Therefore we are not able to integrate the imaginary part of α as shown in the following equations which would provide the sign correctly:

$$\alpha'(\omega) = \frac{2}{\pi}\mathcal{P}\int_0^\infty \frac{\omega'\alpha''(\omega')}{\omega'^2 - \omega^2}\, d\omega' \qquad \text{and} \tag{2.41}$$

$$\alpha''(\omega) = \frac{2}{\pi}\mathcal{P}\int_0^\infty \frac{\omega\alpha'(\omega')}{\omega'^2 - \omega^2}\, d\omega' \qquad \text{with } \alpha(\omega) = \alpha'(\omega) + i\alpha''(\omega). \tag{2.42}$$

In order to decide whether the retrieval of the polarisability α from the Mie cross sections is applicable for our experiments, we have to take a closer look at the values for the size parameter x and its product with the relative refractive index $|\mathrm{m}|x$. These are plotted in Fig. 2.11. Trapping gold and silver nanoparticles 60nm - 100nm with laser light ranging from 400-1100nm does not fulfil the required conditions $x \ll 1$ and $|\mathrm{m}|x \ll 1$. Therefore we are not able to use Eq. (2.36) - (2.40) to describe our experiments adequately. These conditions obtained from Mie Theory provide a more precise limitation than $r \ll \lambda$ which is often cited for the quasi-static approximation. Inserting the polarisability α as presented in Sec. 2.2.2 and in the equations above into the gradient force expression (see Eq. (2.57) in Sec. 2.3) is thus questionable.

Efforts have been made to improve the polarisability description beyond the Rayleigh limit ($d \ll \lambda$) and include the above mentioned shortcomings (red-shifting and broadening of the resonance for larger particles) [39, 42]. By expanding the

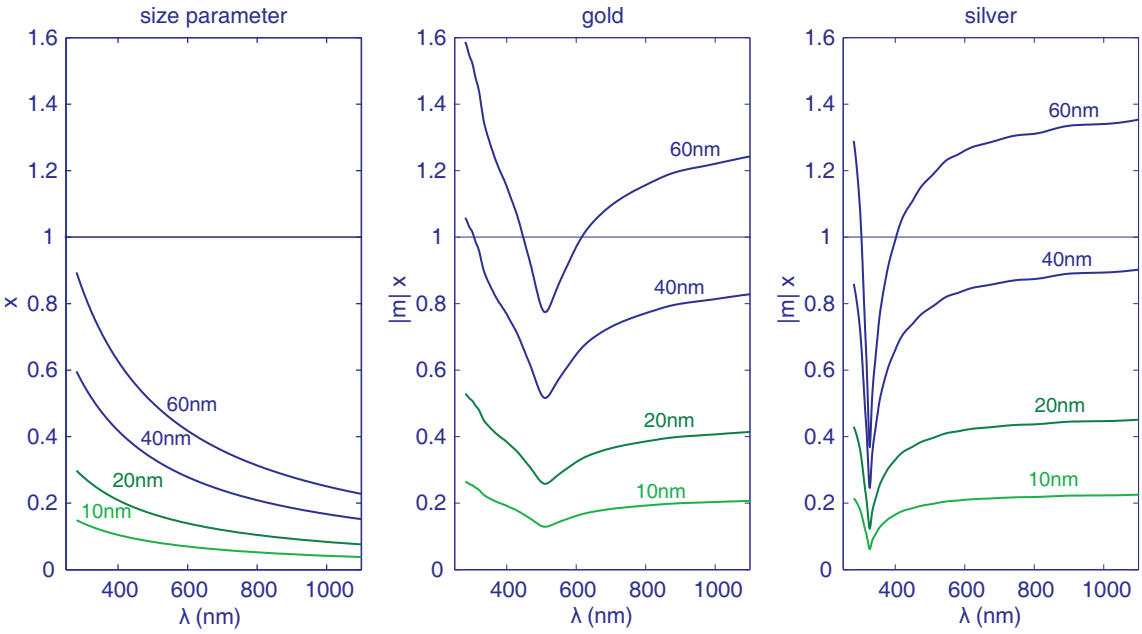

Figure 2.11: The size parameter $x = 2\pi a n_{host}/\lambda$ (left) and its product with the relative refractive index $|\mathrm{m}|x$ for gold (middle) and silver (right) spheres do not fulfil the required conditions $x \ll 1$ and $|\mathrm{m}|x \ll 1$ of the quasi-static approximation for the particle sizes we use in our experiments (60-100nm).

first TM mode of Mie's Theory, an extended expression for the polarisability α is obtained

$$\alpha_{\mathrm{ext}} = \mathrm{V}\frac{1-\frac{1}{10}(\varepsilon_{\mathrm{metal}}+\varepsilon_{\mathrm{host}})\mathrm{x}^2+O(\mathrm{x}^4)}{\left(\frac{1}{3}+\frac{\varepsilon_{\mathrm{host}}}{\varepsilon_{\mathrm{metal}}-\varepsilon_{\mathrm{host}}}\right)-\frac{1}{30}(\varepsilon_{\mathrm{metal}}+10\varepsilon_{\mathrm{host}})\mathrm{x}^2-i\frac{4\pi^2\varepsilon_{\mathrm{host}}^{2/3}}{3}\frac{\mathrm{V}}{\lambda_0^3}+O(\mathrm{x}^4)}. \quad (2.43)$$

Compared to the original Clausius-Mossotti equation (Eq. (2.24)), this expression now includes several new components. The numerator contains the retardation of the exciting field across the particle volume (x^2 term). The second term in the denominator addresses the retardation of the depolarisation field. The latter was not included in the quasi-static approximation at all (see Eq. (2.24)). The depolarisation field exists additionally to the applied field and is created by the polarised matter of the sphere. Including the retardation of the depolarisation field, results in a shift of the resonance to longer wavelengths (lower energies) for larger particle volumes. The third term in the denominator accounts for radiation damping. It is purely imaginary and leads to broadening and decreasing magnitude of the resonance for larger particle volumes. Increasing the particle volume decreases intrinsic damping due to interband transitions as the resonance of the particle moves away from the frequency of this transition. However this non-radiative damping process is coun-

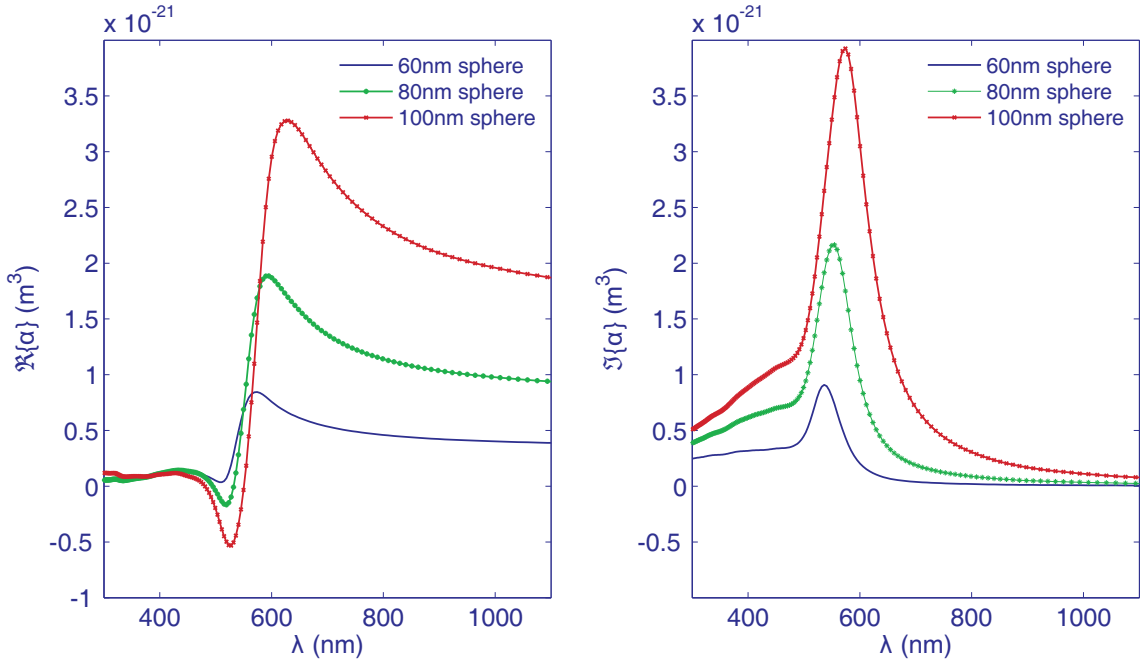

Figure 2.12: We calculated the polarisability α_{ext} for gold nanospheres with various diameters from Eq. (2.43). The red-shifting and broadening of the resonance indicate that dynamic depolarisation and damping effects are included in this model. Another important change compared to the polarisability obtained with the static model (Eq. (2.24) and Fig. 2.8) is the negative real part below the resonance. We analyse the implications of this sign change in Chapter 5.

teracted by the increasing radiative damping for larger particles (third term of the denominator). The reader can find a more quantitative discussion of the various damping mechanisms in [26, 39].

Altogether we can observe the red-shifting and broadening of the resonance for increasing particle size in Fig. 2.12. Interestingly, the real part of the polarisability is now negative below the resonance wavelength as opposed to earlier calculations with the simple Clausius-Mossotti formula (see Eq. (2.24) and Fig. 2.8). This is a very important difference as it implies significant changes for the trapping force. A negative real part of the polarisability means repulsion of the particle from high intensity regions of the trapping laser whereas a positive real part of the polarisability leads to attraction of the sphere to high intensity. The extended model for the polarisability (Eq. (2.43)) provides us with a striking example how different the interpretation of the interaction process between light and metal nanoparticle is compared to the quasi-static approximation. This is particularly important for the interpretation of our blue-detuned trapping results in Chapter 5 where we trap gold nanospheres just below their resonance, exactly in the just described critical region. We conclude that great care has to be taken when using the quasi-static

approximation for trapping metal nanoparticles, in particular close to resonance.

Overall the extended expression for the polarisability α_{ext} seems to address all of the before mentioned shortcomings of the Clausius-Mossotti formula. It does compare well with experimental values for gold and silver nanorods [42]. However deriving this expression required that the size parameter $x \ll 1$ [39]. Is Eq. (2.43) still applicable in our experiments? Including depolarisation and radiation damping is certainly a step in the right direction but whether we have to include even higher order terms (for quadrupolar resonances) or find a different approach not relying on the dipole polarisability α remains to be explored.

2.3 Forces in optical trapping

Subsequent to our introduction on the basics of optical trapping (see Sec. 2.1.3) we now discuss the forces exerted by light in more detail. There are various forces acting on the particle in a trap according to the different processes of scattering, absorption and electric field gradients. The magnitude of the force depends upon the power of the trapping laser, its beam shape at the trap site as well as the material (relative refractive index) and size of the trapped particle.

The main differences between metal and dielectric particles are their material properties. For metal, the polarisability α varies drastically for different trapping wavelengths, in particular close to the metal nanoparticle's plasmon resonance. Dielectric particles are considered to have a constant polarisability for the trapping experiments we study. Consequently the force acting on a metal nanoparticle changes significantly when applying a different trapping wavelength, not only in its absolute value but also its direction. It is possible to attract or repel a particle by simply changing the laser wavelength. This effect is well-known in the field of atom optics where the atomic resonance is used to either attract or repel atoms into or from laser beams. This technique is often referred to as blue and red-detuning of an optical trap. Red-detuning means to use a laser wavelength longer than the trapped particle's resonance whereas blue-detuned employs a laser wavelength shorter than its resonance. In our case of metal nanoparticles, similarly to atom trapping, the force is repulsive on the blue-detuned side of the resonance and attractive on the red-detuned side. We conducted experiments on both sides of the resonance and present the red-detuned experiment in Chapter 4 and the blue-detuned trap in Chapter 5.

This section discusses two concepts describing the forces occurring in optical trapping. The first part presents a method to calculate the total force acting on a particle in an electromagnetic field. As there are no approximations based on the size of the particle, this is a very general method and valid for any size regime. Nevertheless the total force description does not reveal any detailed information about the competing force mechanisms that are present simultaneously in any real experiment. Thus in the second part we discuss the popular gradient and scattering force decomposition

which gives us further insight to the various force mechanism present in an optical trap.

2.3.1 Maxwell stress tensor and Lorentz force

The Maxwell stress tensor offers a complete solution to the problem of a nanoparticle interacting with an electromagnetic field. Once the electromagnetic field distribution of the incoming and the scattered field is known, it is possible to calculate the total force acting on the particle without further approximations. Depending on how accurately we are able to model the incoming field, the result is accordingly exact. The generality of this approach is a powerful tool and hence increasingly applied for describing optical forces on metal nanoparticles more accurately [16, 43, 44].

The Maxwell stress tensor $\mathrm{T_{ij}}$ is based on the conservation of linear momentum in electromagnetic fields. It is derived from Maxwell's equations [32] and gives the momentum density in a medium with permittivity $\varepsilon = \varepsilon_0\varepsilon_{\mathrm{host}}$ and permeability $\mu = \mu_0\mu_{\mathrm{host}}$

$$\overleftrightarrow{\mathbf{T}} = [\varepsilon\mathbf{EE} + \mu\mathbf{HH} - \frac{1}{2}(\varepsilon \mathrm{E}^2 + \mu \mathrm{H}^2)\overleftrightarrow{\mathbf{I}}], \tag{2.44}$$

$$\mathrm{T_{ij}} = \sum_{\mathrm{k}} \varepsilon \mathrm{E_i E_j^*} + \mu \mathrm{H_i H_j^*} - \frac{1}{2}\delta_{\mathrm{ij}}(\varepsilon \mathrm{E_k E_k^*} + \mu \mathrm{H_k H_k^*}) \tag{2.45}$$

with the unit tensor $\overleftrightarrow{\mathbf{I}}$. The complex conjugate is denoted with the star and the second expression gives the Maxwell stress tensor in Cartesian coordinates. Integrating the Maxwell stress tensor over a surface S including the particle of interest and averaging over one optical cycle leads to the expression for the total optical force exerted by the incident electromagnetic field onto the particle

$$\langle \mathbf{F} \rangle = \int_{\mathrm{S}} \langle \overleftrightarrow{\mathbf{T}}(\mathbf{r}, \mathrm{t}) \rangle \cdot \mathbf{n}(\mathbf{r}) \mathrm{ds}, \tag{2.46}$$

$$\langle \mathrm{F_i} \rangle = \frac{1}{2} \Re \Big\{ \int_{\mathrm{S}} \mathrm{T_{ij} n_j ds} \Big\} \tag{2.47}$$

with the second expression in component form again. Note that the total force depends solely on the properties of the electromagnetic fields as they contain the entire information about the physical processes. Consequently, this method is very general as the particle of interest can have any shape or size. The surface of the integration is arbitrary and can either be situated directly on the surface of the particle or in the far field. However, as mentioned before, the electromagnetic fields have to be self-consistent, they are a superposition of the incident and scattered fields and have to be known in order to find the total force. In most cases this

condition requires extensive full numerical calculation with finite element or finite difference time domain methods. Modelling a tightly focussed Gaussian beam has its own challenges [45] and we have to remember that it is crucial to focus the beam tightly. Metal nanoparticles are only trapped using high NA objectives (NA=1.3 or larger); resorting to a weakly focussed paraxial beam approximation would not represent the experimental conditions.

Alternatively, we can approach the problem of force calculation via the Lorentz force

$$\mathbf{F}_{\mathrm{Lorentz}} = \mathrm{q}\Big(\mathbf{E}(\mathbf{r},\mathrm{t}) + \mathbf{v}(\mathbf{r},\mathrm{t}) \times \mu\mathbf{H}(\mathbf{r},\mathrm{t})\Big). \tag{2.48}$$

Deriving the optical force density from Eq. (2.48) and integrating over the volume of the particle again leads to the total optical force [46, 47]. This procedure requires a complete description of the incoming field and also the polarisation of the particle as a result of these fields. Both methods presented in this section thus require solving Maxwell's equations for the problem in full, finding solutions to the incident field and the scattered field by the particle. We demonstrate in the next section how the Lorentz force is used as a starting point to obtain the well-known force expressions for the small particle limit.

2.3.2 Gradient and scattering force decomposition

In most publications on optical trapping, the total force is decomposed into gradient, scattering and absorption forces. This decomposition is the common method to calculate forces for trapping atoms and micron-sized dielectric spheres alike. Historically, trapping forces have been derived first for atoms as they can be treated in the dipole limit [48]. Later on it was shown that large micron sized dielectric spheres can also be treated in this manner of gradient and scattering forces [35]. Geometrical optics proves helpful to determine the force components for dielectric particles of the order of the wavelength or larger.

For Rayleigh particles one may derive concise equations starting with the Lorentz force (2.48). In the small-particle limit it is possible to define the dipole moment $\mathbf{p}$ of the particle depending on its macroscopic polarisability α and the incident electric field $\mathbf{E}$

$$\mathbf{p} = \varepsilon\alpha\mathbf{E} \tag{2.49}$$

with the permittivity of the host medium $\varepsilon = \varepsilon_0\varepsilon_{\mathrm{host}}$. The force exerted on the dipole follows from the Lorentz force (2.48), the dipole moment and a Taylor expansion up to the second term (dipole approximation) of the incident electric and magnetic fields, $\mathbf{E}$ and $\mathbf{H}$:

$$\mathbf{F}_{\mathrm{tot}} = (\mathbf{p}\cdot\nabla)\mathbf{E} + \mu\frac{\mathrm{d}\mathbf{p}}{\mathrm{d}\,\mathrm{t}} \times \mathbf{H} \tag{2.50}$$

The permeability of the host medium is defined as $\mu = \mu_0\mu_{\text{host}} = \mu_0$ for $\mu_{\text{host}} = 1$. Applying the vector equality

$$(\mathbf{E}\cdot\nabla)\mathbf{E} + \mathbf{E}\times(\nabla\times\mathbf{E}) = \sum_{\text{j}} \text{E}_{\text{j}}\nabla\text{E}_{\text{j}}, \tag{2.51}$$

the dipole moment

$$\mathbf{p} = \varepsilon_0\varepsilon_{\text{host}}\alpha\mathbf{E}, \tag{2.52}$$

Maxwell's equations

$$\nabla\times\mathbf{E} = -\mu_0\frac{\partial}{\partial\text{t}}\mathbf{H} \quad \text{and} \tag{2.53}$$

$$\frac{\partial}{\partial\text{t}}(\mathbf{E}\times\mathbf{H}) = (\frac{\partial}{\partial\text{t}}\mathbf{E})\times\mathbf{H} + \mathbf{E}\times(\frac{\partial}{\partial\text{t}}\mathbf{H}) \tag{2.54}$$

Eq. (2.50) is rewritten as [48]

$$\mathbf{F}_{\text{tot}} = \varepsilon_0\varepsilon_{\text{host}}\alpha\Big[\sum_{\text{j}}\text{E}_{\text{j}}\nabla\text{E}_{\text{j}} + \mu_0\frac{\partial}{\partial\text{t}}(\mathbf{E}\times\mathbf{H})\Big]. \tag{2.55}$$

Averaging the total force (Eq. (2.55) over one optical cycle ($\langle\rangle$ notation) and including the fact that the fields as well as the polarisability ($\alpha = \alpha' + i\alpha''$) are complex quantities leads to

$$\langle\mathbf{F}_{\text{tot}}\rangle = \frac{1}{4}\varepsilon_0\varepsilon_{\text{r}}\alpha'\nabla(\mathbf{E}^*\mathbf{E}) + \frac{1}{2}\varepsilon_0\varepsilon_{\text{r}}\alpha''\Im\{\sum_{\text{j}}\text{E}_{\text{j}}^*\nabla\text{E}_{\text{j}}\}. \tag{2.56}$$

In contrast to the general formalism presented in Sec. 2.3.1, the fields $\mathbf{E}$ and $\mathbf{H}$ entering this calculation are only the incident fields. The dipole is assumed to be too small to disturb the incoming fields and thus no self-consistent field calculations are required. This is the major advantage of this approach as it is significantly easier to calculate the forces involved. We can now decompose the total force in its individual force components: the gradient, absorption and scattering force [32, 49] from Eq. (2.56)

$$\langle\mathbf{F}_{\text{grad}}\rangle = \frac{1}{4}\varepsilon_0\varepsilon_{\text{r}}\alpha'\nabla(\mathbf{E}^*\mathbf{E}), \tag{2.57}$$

$$\langle\mathbf{F}_{\text{scat}}\rangle = \frac{\text{n}_{\text{host}}}{\text{c}}\text{C}_{\text{scat}}\langle\mathbf{S}\rangle, \tag{2.58}$$

$$\langle\mathbf{F}_{\text{abs}}\rangle = \frac{\text{n}_{\text{host}}}{\text{c}}\text{C}_{\text{abs}}\langle\mathbf{S}\rangle. \tag{2.59}$$

The scattering and absorption cross section (C_{scat}, C_{abs}) have been discussed in Sec. 2.2 and $\mathbf{S}$ is the Poynting vector. The gradient force is a conservative force.

The scattering force is not, as its work done is always path dependent [35, 50, 51]. Eq. (2.57)-(2.59) are almost exclusively used in the literature to describe optical trapping. The absorption force is usually neglected for dielectric objects. The popularity of this concept is based on the easy and fast applicability of this force decomposition as only the incident field and some material parameters have to be known. Also, using these equations already implies the underlying physical processes. Optical trapping only occurs when the gradient force is strong enough to overcome the scattering and absorption force. They thus give a picture of what is happening to the particle in the trap. Ashkin even used these to give a limit of the smallest particles one can possibly trap [17]. Of course, all this information is included in the total force description of Sec. 2.3.1 as well. However, it does not show in a clear manner how trapping actually works.

2.3.3 Limits and open questions

In the beginning of this chapter we discussed the possibilities to describe the response of a metal nanoparticle to an electromagnetic field in terms of polarisability and cross sections. Analysing the assumptions made in order to develop expressions for the polarisability α, we found that this model is not adequate for our experimental situation. Expressing the metal nanoparticle's response in terms of α is based on the idea that the particle is small enough to be considered as a dipole. We are investigating 40-100nm sized gold and silver spheres exposed to visible laser light in our work which definitely do not fall into this range. We presented an approach to improve the Clausius-Mossotti approximation by including depolarising fields and retardation. However, it is always assumed that the particle is small enough to be approximated by a dipole. Alternatively, the description resulting from Mie theory in terms of cross sections has no such limitations and can therefore be seen as exact.

These findings directly affect how we calculate the forces acting on the metal nanoparticle in the trap. The commonly used decomposition in gradient, scattering and absorption force should be applied with great care for metal nanoparticles of the size ranges discussed here, in particular close to the plasmonic resonance. The derivation of the gradient force requires the particle to be treated as a dipole in the incident field. The gradient force is per definition the force on a dipole, hence sometimes called dipole force (in particular in the field of atom optics). The generalisation made in [35] to apply this concept to large Mie-sized dielectric particles cannot be applied in our case as light is not propagating through metal nanoparticles and we cannot use the geometric optics approach. Even if we could assume the gradient force description to be almost correct, we have limited means to model the polarisability α exactly.

Yet the gradient force description remains the prevailing method used to date describing optical trapping of metal nanoparticles [7, 9, 10, 13, 14, 16, 22]. One could argue that this is good enough for a qualitative description of trapping far from

resonance of the metal nanoparticles (in the infrared). At 1064nm, silver and gold nanoparticles are approximately acting like absorbing dielectrics with a large refractive index. Also their size compared to the wavelength is smaller. However, close to the particle plasmon resonance the force decomposition approach and therefore the convenient description of the various processes of scattering and gradient force interaction is not applicable any longer. We discuss this issue further in Chapter 5 where we show that the interpretation of the physical process of the particle in the trap is not uniquely defined when using this force decomposition approach. As mentioned before, the calculation of the forces with Maxwell's stress tensor or the Lorentz force is rather cumbersome requiring full solutions to Maxwell's equations. It only gives the total force and no indication of the ratio of the different physical processes involved and thus no physical intuition. These could be the reasons why everyone keeps referring to the gradient and scattering force however questionable this description is.

The open challenge remains to develop a force description for a metal nanoparticle in a tightly focussed electromagnetic field. Is it possible to achieve a concise form as proposed by the gradient and scattering force decomposition? Would the expansion into higher orders be sufficient or do we need an entire new concept? Or is the total force obtained through Maxwell's stress tensor method meaningful enough?

Additionally, until now only linear processes are taken into account. Silver and gold nanoparticles show nonlinear optical responses and the field intensities close to nanoparticles are enhanced significantly. It would not be surprising if nonlinear processes occur at the centre of the trap where a (sometimes even pulsed) laser beam is focussed onto the metal nanoparticle. Recent experimental investigations confirmed the occurrence of nonlinearities in gold nanoparticles [4, 52, 53].

2.4 Conclusions

This chapter introduced the theoretical foundation for our work. In the first section we presented the permittivity $\varepsilon(\omega)$ and the skin depth δ as parameters to describe metal-light interactions. We continued with the concept of the particle plasmon, the distinct feature of metal nanoparticles. Based on this knowledge we established the polarisability α as a key concept to describe the metal nanoparticle's resonance and response to an incident light field. We discussed three different methods to determine the polarisability of a spherical particle: the quasi-static approximation (Clausius-Mossotti), the retrieval from Mie's cross sections and an extension of the quasi-static approximation.

The importance of the polarisability for optical trapping becomes clear in the third section where we examine two force models for optical trapping. First we present a very general method of calculating the total force acting on a particle in the trap with the Maxwell stress tensor. Second we derive the equations for the commonly used

force decomposition model from the Lorentz force. The polarisability is a central quantity for the gradient force in this model.

We analysed the conceptual challenges we face for interpreting our experiments with the presented models. Although the polarisability is used almost exclusively to describe the particle's response in optical trapping [7,9,10,13,14,16,22] we discovered that we do not remain in the range of its validity for metal nanoparticles. The polarisability is per definition a charge distribution of a dipole. Due to the size of our metal nanoparticles their excitation is likely to contain higher orders and their interaction with the incident field cannot be neglected. However the polarisability models discussed in this work and the force decomposition are the only tools to date helping to understand the underlying physical processes in the trap. We therefore stick to these methods, but with caution, and demonstrate their ambiguous outcome in Chapter 5.

3 Experimental setup

We aim to give the reader detailed technical insight in our work with this chapter. Presenting the methods employed throughout our experiments helps to separate technical discussion and the result analysis of the following chapters. In the beginning we review the optical setups for different trapping geometries. The single-beam trap is likely to be familiar to the reader and is the central part of our experiment described in Chapter 4. Furthermore, it provides the basis of the Laguerre-Gaussian ring trap used for the experiment described in Chapter 5. We also discuss a dual beam trap which we tested for trapping metal nanoparticles. Due to the wavelength dependence of the metal nanoparticle resonance we use a variety of laser sources supplying different wavelengths according to the specific experimental requirements. The experimental setups discussed in here are specifically designed and built for nanoparticle manipulation; there has been no nanoparticle trapping system prior to this study in our group.

The main focus of this chapter is on nanoparticle imaging. This is one of the challenging parts, in particular in combination with optical trapping. Metal nanoparticles smaller than 100nm cannot be resolved with standard brightfield transmission microscopy. Other groups have tried various elaborate methods [13,14] or abstained from imaging entirely [7, 15]. We developed a very practical and simple technique that allows us to image metal nanoparticles down to 40nm without interefering with the performance of the optical trap as reported elsewhere [9].

The last part of this chapter describes our detection system. We used two different types of particle tracking throughout this work - video and electronic detection. We give a short introduction to the electronic detection using a quadrant photodiode (QPD) that has been researched extensively [54, 55]. Finally we describe the calibration techniques we used for both systems.

3.1 Materials and sample preparation

All experiments in this thesis investigated gold and silver nanospheres in solution. We purchased nanoparticles from British Biocell International (BBInternational [56]). They are suspended in water (H_2O) with concentrations depending on the particle size. For our imaging experiments we used gold spheres with 40nm, 60nm, 80nm, 100nm and 250nm in diameter as well as silver spheres with 40nm, 60nm and 80nm in diameter. These particles did not need any additional stabilising

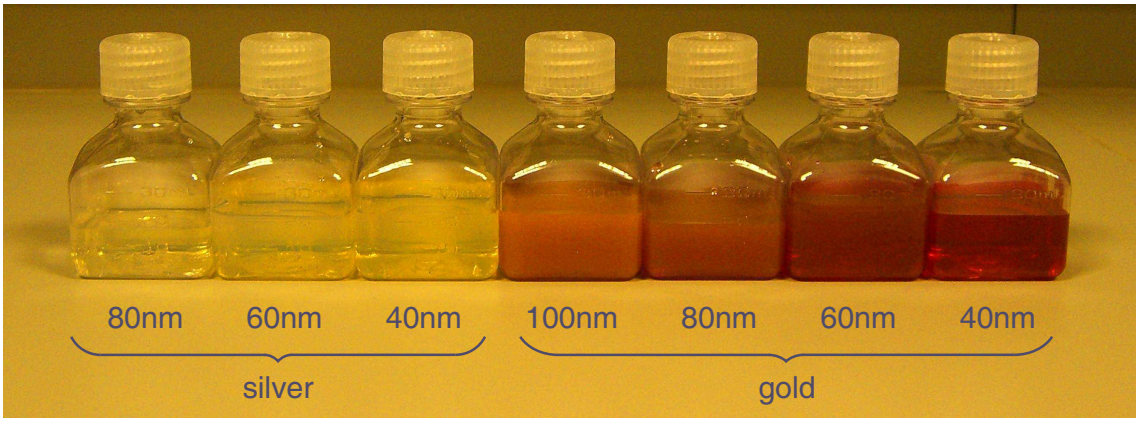

Figure 3.1: The metal nanoparticles we used for our experiments vary in colour and transparency depending on their size. Gold and silver have different particle plasmon resonances and thus absorb and scatter in different regions of the visible spectrum which gives them their distinct colour. We purchased all samples from British Biocell International (BBInternational [56]).

coating.

Nanoparticles are commonly dispersed in aqueous solutions. A practical consequence is the damping of the particle motion, thus decreasing the Brownian motion of the nanoparticles. Also, the nanoparticles are small enough to float in solution and do not settle due to gravity. The particles are therefore able to diffuse into the optical trap solely on the basis of their Brownian motion.

Figure 3.1 displays the particles in solution as purchased from BBI. The gold nanoparticles show the effect of absorption and scattering depending on particle size as we discussed in the previous chapter. Mie theory suggested that scattering becomes comparable to absorption for gold spheres around 80nm and is dominant

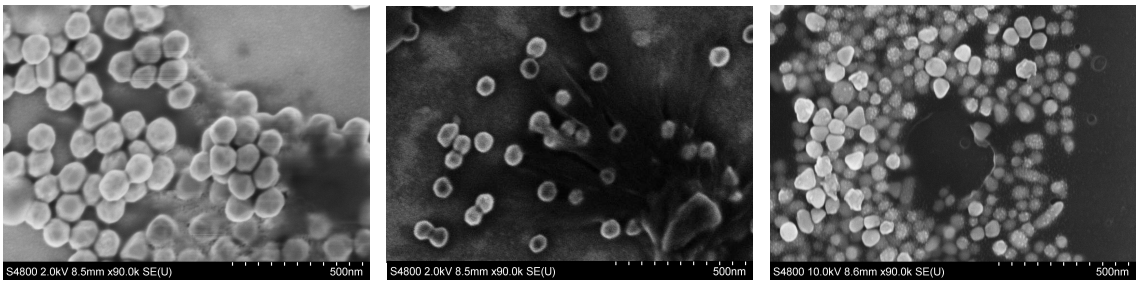

Figure 3.2: The high resolution SEM (scanning electron microscope) images helped to determine the true size distribution in the purchased nanoparticle sample solutions. We dried a droplet of solution containing the nanoparticles on an ITO (indium tin oxide) coated coverslip and acquired sample pictures from 100nm gold (left), 80nm gold (middle) and 80nm silver (right) nanoparticles.

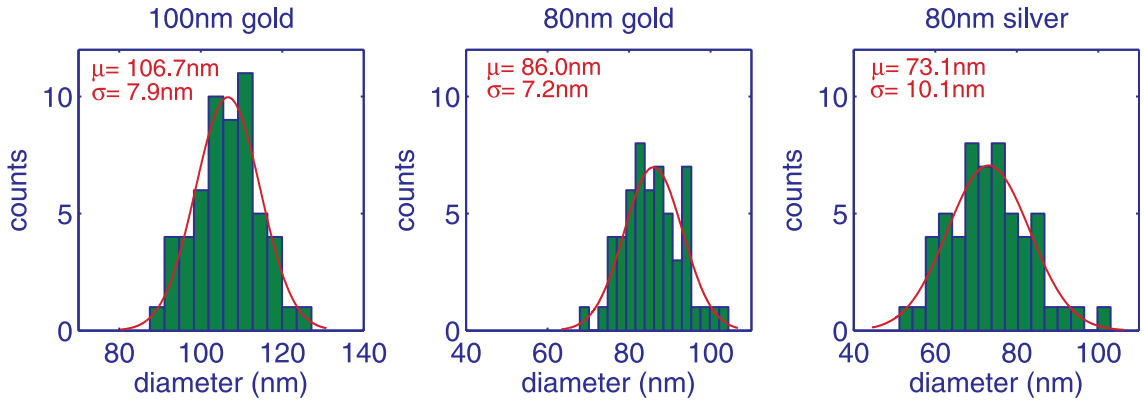

Figure 3.3: We measured the size of 100nm and 80nm gold as well as 80nm silver nanoparticles (60 each). The histograms show the size distribution of the purchased samples with the mean diameter μ and the standard deviation σ. The gold particles are slightly larger than expected; the silver particles are smaller than indicated and vary significantly in size and shape.

for 100nm gold spheres. As we see in the picture, the solutions with gold spheres 40nm and 60nm are transparent; the ones with 80nm and 100nm are cloudy. The red colour stems from absorption. The nanoparticle's resonance is in the green, which is absorbed and renders the transmitted light red as the green parts are missing. For silver these effects are not as obvious, because their resonance is in the blue and the concentration of the particles in solution is smaller than for gold. The manufacturer does not give any particle concentration.

We are interested in the size distribution of the metal nanoparticles for our experiments. The manufacturer only provides approximate values (for example: 60nm ± 5nm). Therefore we analysed the size distribution of our sample solutions further with an SEM (scanning electron microscope). We measured the particle size for 80nm silver spheres as well as for 80nm and 100nm gold spheres, the particles we used for our experiments in Chapters 4-5. Figure 3.3 presents the resulting particle size distributions. After taking an image of the particles in the SEM with the according scale bar we subsequently analysed the diameter of each individual sphere and determined the size distribution in a custom made software programme. The pictures show that the nanoparticles do not only vary in size but also shape (see Fig. 3.2). Shape aberrations are not as critical as they result in a clear abnormal scattering and absorption behaviour. Our advanced imaging system enables us to distinguish and preselect those irregular particles. Small particle size variations are a source of error for precision measurements as they lead to broadening trap stiffness data.

Glass coverslips (50mm x 20mm, thickness No.1 - 0.16mm) form our sample chambers, holding approximately 10 microlitres of nanoparticle solution. Depending on the depth of the sample chamber required we put a vinyl spacer (adhesive sticker)

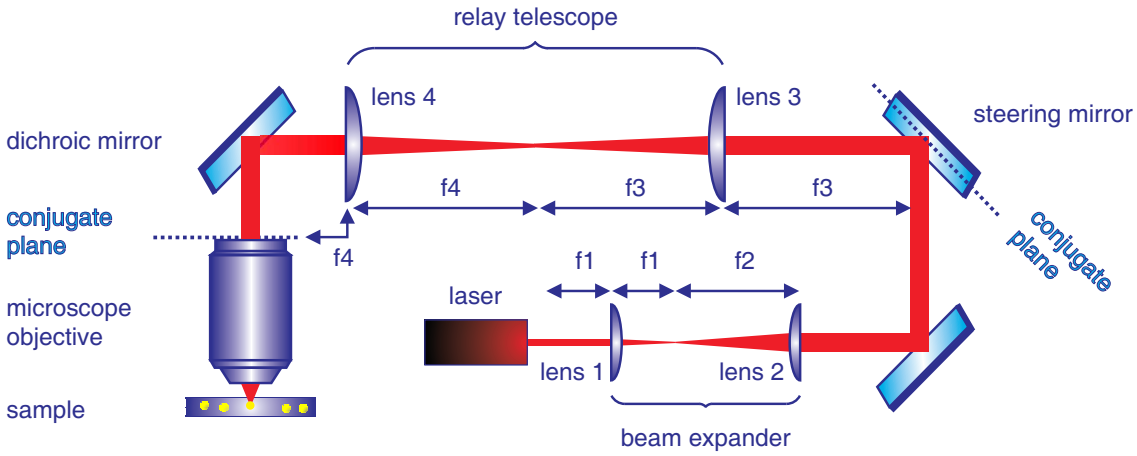

Figure 3.4: Conventional optical tweezers are composed of a laser tightly focussed by a high numerical aperture (NA) objective. The relay telescope creates conjugate planes to steer the beam focus in the sample plane. Quite often the relay telescope works in combination with the beam expander to achieve the required beam diameter matching the back aperture of the trapping objective.

between two slides. Without spacer, we vary the chamber depth with the amount of nanoparticle solution put in between the two slides. Evaporation of the sample solution was not a problem with the plastic spacer which sealed the contained solution all by itself. Once prepared, we were able to use the sample for several days. We inserted the sample into the sample plane of the optical trap which is situated at the focus of the trapping microscope objective (see Fig. 3.4).

3.2 The optical setup

Building an optical trap for metal nanoparticles is in many ways identical to setting up a standard trap for micron-sized particles. We dedicate separate sections to the illumination and detection as these two topics become more challenging for nanoparticles. We start this section describing conventional optical tweezers that are the central part of our red-detuned tweezing experiments presented in Chapter 4. A dual beam trap has been suggested to be advantageous for metal nanoparticle trapping [13], thus we present our experiments with this trapping geometry here. Depending on the trapping geometry, we have to consider adequate objectives with the right choice of numerical aperture (NA), the types of lasers and the beam delivery. We would like to stress that we trap the metal nanoparticles in 3 dimensions deep in the sample chamber to avoid proximity effects that distort the trap stiffness measurements. This is harder to achieve and different to 2D trapping where the confinement along the beam axis is accomplished by pushing the trapped sphere against the glass coverslip of the sample chamber [9].

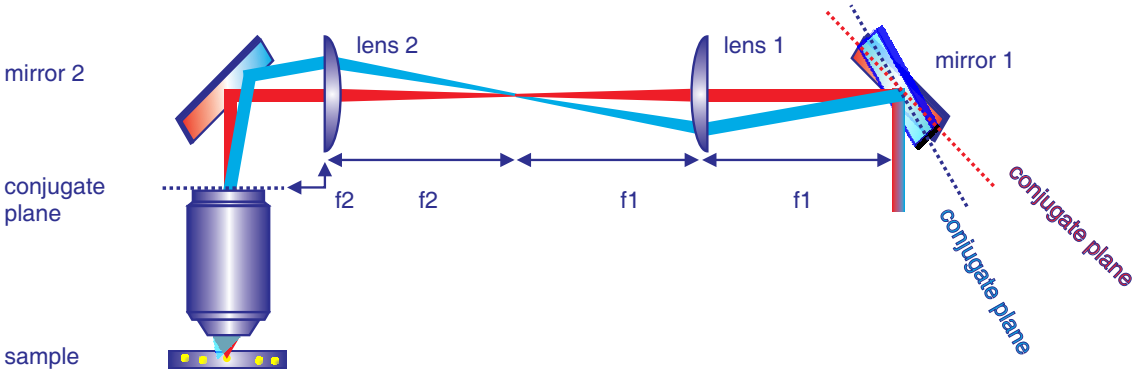

Figure 3.5: This is a detailed view of the beam steering mechanism provided by the relay telescope. The two lenses image the beam steering mirror onto the back aperture of the objective. In that way we can move the laser focus in the sample plane without the beam walking off the entrance pupil of the back aperture of our trapping objective.

3.2.1 The single-beam trap: Optical tweezers

The standard optical tweezers is composed of a laser trapping the particle, a high NA objective to focus the trapping laser tightly, beam resizing optics to acquire a suitable laser beam diameter and beam steering optics such as mirrors coated appropriately to the applied laser wavelength. We provide a diagram of a generic tweezers setup in Fig. 3.4 including the key elements essential to control the position and form of a single laser beam. We implemented our tweezers setup around a basic microscope (Nikon Eclipse LV100) to benefit from the robustness and fine-steering of the microscope stage.

To optically tweeze a nanoparticle we require a strong trap stiffness, which means to focus a Gaussian laser beam as tightly as possible to achieve high intensity gradients in all directions in space (x-y-z). We chose an oil immersion microscope objective with a high numerical aperture and focussing abilities (Nikon CFI Plan Fluor, 100x oil, NA 1.3) for our experiment. The diameter of the trapping beam has to match the back aperture of the microscope objective in order to get the steepest field gradient at the focus of the trap. For trapping metal nanoparticles this is particularly important as a slight decrease in trapping efficiency potentially renders trapping impossible. The input beam should neither be clipped nor underfill the back aperture. The lens systems of the beam expander and relay telescope serve to adjust the beam diameter according to our needs (see Fig 3.4). Depending on the laser output, the beam expander may be redundant. We found that using high refractive index immersion oil, not matched to the index of refraction of the glass coverslip, increased the trapping abilities along the beam axis according to [57].

The relay telescope is not always used for beam resizing as it serves yet another, more important purpose. Two lenses (lens 3 and lens 4 in Fig. 3.4), spaced the sum of their focal lengths apart, form the relay telescope. The objective back aperture

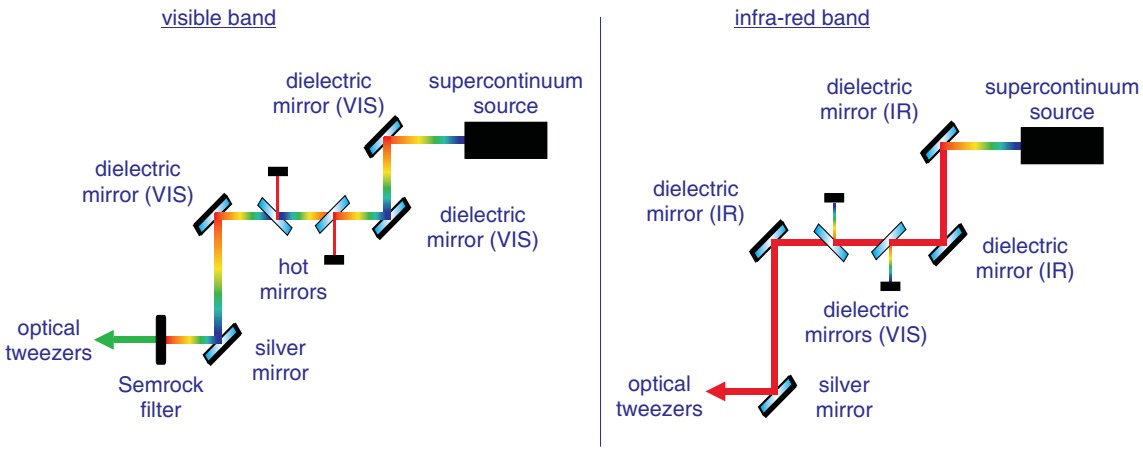

Figure 3.6: We passed the broadband supercontinuum through a range of wavelength specific reflection and filtering optics. *Left* - The combination of 3 dielectric mirrors (Thorlabs EO2, 400-750nm reflective) and 2 hot mirrors (Thorlabs, 750-1200nm reflective) filtered out the infrared part of the spectrum. Inserting a Semrock brightline filter allowed us to select 40nm out of the visible part of the spectrum, depending on the filter. *Right* - Combining 3 dielectric mirrors (Thorlabs EO3, 750-1100nm reflective) to reflect part of the infrared spectrum and 2 dielectric mirrors (Comar, 400-900nm reflective), specifically coated to filter out the remaining visible parts of the spectrum, helped us to select a band (900-1100nm) for our in infrared experiments.

and the steering mirror (mirror 1 Fig. 3.4) form optical conjugate planes. That way, the trapping beam can move in the sample plane without being displaced off the back aperture of the objective. The position of the beam at the conjugate planes remains fixed as these are imaged onto each other with the relay telescope. However, the position of the beam focus in the sample plane as well as the beam path change according to the movement of the steering mirror. Figure 3.5 shows a more detailed diagram of the beam path between the steering mirror and the sample plane through a relay telescope.

We chose appropriate anti-reflection coated lenses (visible 450-900nm, infrared 630-1100nm) for all experiments to minimise back reflection and power losses. Our laser source for the single-beam trap is a supercontinuum laser from Fianium, providing a pulsed (10ps, 40MHz repetition rate) output covering the entire spectrum between 470nm-1750nm. We took specific narrow wavelength bands out of this broad spectrum by exploiting this one laser as a multi-line source. We selected the relevant wavelength bands with a combination of dielectric mirrors and Semrock brightline filters. The wavelength band for our infrared experiments was 200nm broad, whereas the selected visible bands were only 40nm wide. The latter provided just enough power after all filtering steps for optical trapping. The two diagrams in Fig. 3.6 show more details of the filtering beam path before entering the optical tweezers.

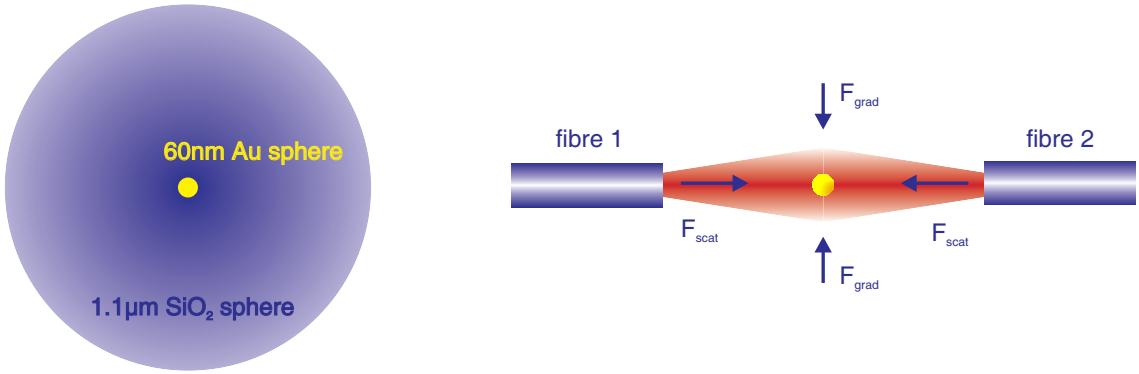

Figure 3.7: *Left* - The two pictured objects have the same scattering cross section, although the 60nm gold sphere is a lot smaller compared to the 1.1μm silica sphere. This sketch illustrates that metal nanoparticles have a much larger scattering cross section than their same-sized dielectric counterparts. *Right* - The dual beam fibre trap holds a particle at the point where the scattering forces F_{scat} of the two counter propagating laser beams balance out. The gradient force F_{grad} of the Gaussian beam profile provides confinement orthogonal to the beam axis.

3.2.2 The dual beam trap: Fibre trap

Metal nanoparticles scatter more light than dielectric beads as a result of their larger scattering cross section (see Fig. 3.7). Consequently the scattering force F_{scat} exerted on a metal particle in a laser beam is larger than the force upon dielectrics of the same size. In an optical tweezers configuration the scattering force destabilises trapping. Thus it has been suggested to design an optical trap taking advantage of the increased scattering force [13]. A dual beam trap takes advantage of the scattering force by holding a particle in the middle of two counter propagating beams. Stable trapping occurs at the position where the scattering force components of both beams along the optical axis cancel out. The confinement perpendicular to the propagation axis is realised by the gradient force F_{grad} present due the Gaussian beam profile. Figure 3.7 shows a diagram of a dual beam fibre trap. Optical fibres deliver the trapping beams into the sample chamber.

We tested a dual beam fibre setup, which has been used successfully before in our group, for various studies on micron sized dielectric beads [58, 59]. We implemented the fibre trap in a standard microscope setup taking advantage of the imaging and illumination system of the microscope. A dual beam trap needs fewer optics and beam alignment compared to single beam tweezers. We chose a linearly polarised 1070nm fibre laser (IPG photonics VLM-5-1070-LP) for our experiment. The laser coupled through a microscope objective (Newport, 10x) into a single mode fibre suitable for this wavelength (Thorlabs, 6.6μm core size, single mode). A fibre launch stage (Elliot Scientific MDE510) turned out to be helpful for aligning the input beam and achieving better coupling efficiency. A single mode fibre coupler with a

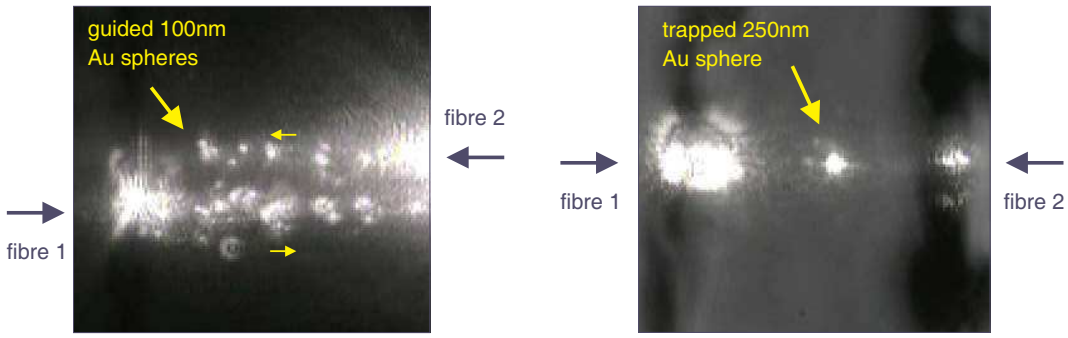

Figure 3.8: *Left* - The two fibres of the dual beam trap are not aligned on the same axis which results in guiding of the 100nm gold spheres rather than trapping. *Right* - We achieved trapping of a 250nm gold sphere in the dual beam fibre trap.

50:50 split ratio divided the incoming fibre into two arms for the dual fibre trap (Thorlabs, FC1064-50B). The power output at both fibre ends was the same and could be adjusted by slightly bending one fibre.

The two opposing optical fibres are directly inserted into the sample chamber. We imaged the sample chamber in brightfield transmission microscopy, perpendicular to the fibre axes. We fixed one fibre on the glass coverslip of the bottom of the sample chamber. We used a spacer (adhesive sticker) of the same thickness as the fibre diameter so we were able to place a second glass coverslip on top to prevent the sample from evaporating. The spacer had two opposing gaps to insert the fibres. Attaching the second fibre to an x-y-z stage gave us full control of its positioning and its alignment with the fixed fibre. We experimented with 100nm and 250nm gold nanoparticles. We also added ethylene glycol to the nanoparticle buffer solution to delay the evaporation of the sample. This made the buffer solution more viscous, damping the particle motion even further which helped to achieve trapping.

The alignment of both fibres proved to be the critical part of the experiment. As the fibre output has a weakly diverging Gaussian profile, the beam will spread with propagation distance. Consequently the gradient across the profile decreases which results in less effective transverse trapping. Hence the gradient force is rather weak and the trapping of the particle is dominated by the scattering force. The slightest offset of the two fibres causes the scattering forces of the opposing beams not to be along the same axis and the weak transverse trapping is not able to hold the particle. The gold spheres are guided away from the trap site, along the beam from one fibre end to the other as shown in Figure 3.8 on the left side.

It was straightforward to achieve guiding of 100nm and 250nm gold spheres as pictured in Fig. 3.8. However, we only managed trapping of 250nm gold spheres occasionally and never for 100nm gold spheres. The gradient of the Gaussian fibre output was too weak to produce a strong enough gradient force to hold 100nm gold spheres. Once trapped, we were able to move the position of the 250nm gold

sphere between the fibres towards one or the other by varying the laser power in one of the fibres. In addition to positioning the fibres along the same axis, the angle towards each other had to be exactly 180° to create a trap site where the scattering forces would cancel out and the gradient force would be strong enough for transverse trapping. The particles entered the propagating laser beam transversely from all directions and accelerated along the axial beam propagation path. With no correctly aligned opposing beam they would speed up towards the other fibre and eventually fall out of the guiding beam as the gradient force weakened over distance.

For micron-sized particles alignment is not as critical as the particles are larger. Their Brownian motion is too small to disturb trapping as substantially as it does for nanometer-sized particles and thus less force is needed to stably trap micron-sized spheres. The ratio of scattering and gradient force for micron-sized dielectrics is also completely different to the one for nanometre-sized metal particles. For micron-sized dielectrics, a slight misalignment of the fibres usually only degrades trapping a little resulting in a trap site off-axis. Additionally light is able to propagate through a dielectric particle which then acts as a lens and supports the gradient force for trapping.

Overall we found that this trapping geometry works in principle but poses challenging technical issues. Designing a setup with nanometre-precise fibre alignment is necessary to achieve trapping for 100nm metal particles. Additionally the issue of sample evaporation need to be addressed. A sealed sample chamber, still allowing the movement of one fibre would certainly be beneficial. We suggest increasing the transverse gradient force by using lensed fibres in the future. Because of these difficulties we did not pursue the fibre trapping geometry any further. However, there have been investigations showing a dual beam trap created with two opposing objectives instead of optical fibres to work satisfactory [60]. This certainly solves the issue of week transverse gradient forces and adds additional gradient forces towards the common focus, though this setup is more complex than single beam tweezers.

3.3 Imaging nanoparticles

Imaging metal nanoparticles smaller than 100nm in real time is difficult. The reason is simply that metal nanoparticles are smaller than the diffraction limit. In standard brightfield microscopy, the smallest gold particles we are able to image have a diameter around 100nm. However, we would like to experiment with particles much smaller than this.

The resolving power of an optical system determines the ability to distinguish between fine features and visualise tiny objects. The numerical aperture (NA) of the involved objectives is not the only factor affecting the resolution of a setup but also the coherence of the illumination, the refractive index of the object compared to the host medium or contrast enhancing techniques. In the past, investigators have

been very inventive to trick the diffraction limit and still be able to visualise trapped nanoparticles. Commonly this involves more elaborate techniques such as differential interference contrast microscopy (DIC) [13], confocal microscopy [14] or using an additional laser source to excite nonlinear luminescence [10, 15, 61]. Alternatively many experiments leave out direct imaging altogether and rely solely on electronic detection via a quadrant photodiode (QPD) [7, 22, 38]. A more detailed summary of these techniques is given in [47].

We investigated various imaging systems to find a suitable solution for our trapping experiments. We aimed to visualise metal nanoparticles smaller than 100nm, to image in real time while trapping and to be able to distinguish if one or more particles are trapped. For our first experiment, the blue-detuned trap (see Capter 5), we improved brightfield microscopy with Köhler illumination in transmission as far as possible. We were able to see gold spheres as small as 80nm. Later on we explored brightfield microscopy illuminating our sample in reflection (episcopic). This technique is considered as very basic and in general not the first choice. But we discovered that episcopic brightfield microscopy is by far the best imaging technique for our purpose. We were able to visualise gold and silver spheres as small as 40nm. Additionally our system allowed us to distinguish between one or several particles in a trap. At the end of this section we present our results for darkfield microscopy which seemed a very promising choice. However, in combination with optical tweezers, darkfield microscopy did not turn out to be practical.

3.3.1 Brightfield microscopy in transmission - diascopic illumination

The standard imaging technique in optical trapping is brightfield microscopy with the sample illuminated in transmission. This method is flexible, easily implemented in a home-built system and provides good contrast and brightness control of the image. The sample is either illuminated from the top (inverted microscope) or from the bottom (upright microscope) depending upon the type of setup. In both cases, the trapping laser is opposing the illumination beam throughout the sample. The trapping objective is fixed, the sample stage, the condenser objective and the laser beam can be moved.

To image metal nanoparticles most effectively we have to increase the resolution of the entire imaging system as much as possible. The total resolution of a lens system depends on the NA of the entire system (condenser and trapping objective) as well as other factors such as wavelength and coherence of the illumination, contrast and brightness. For trapping and imaging nanoparticles we require a high NA trapping objective (see Sec. 3.2) which is best complemented by a condenser objective instead of a simple lens to increase the total resolution of the system. The illumination path is best set up according to Köhler as this provides an even illumination with

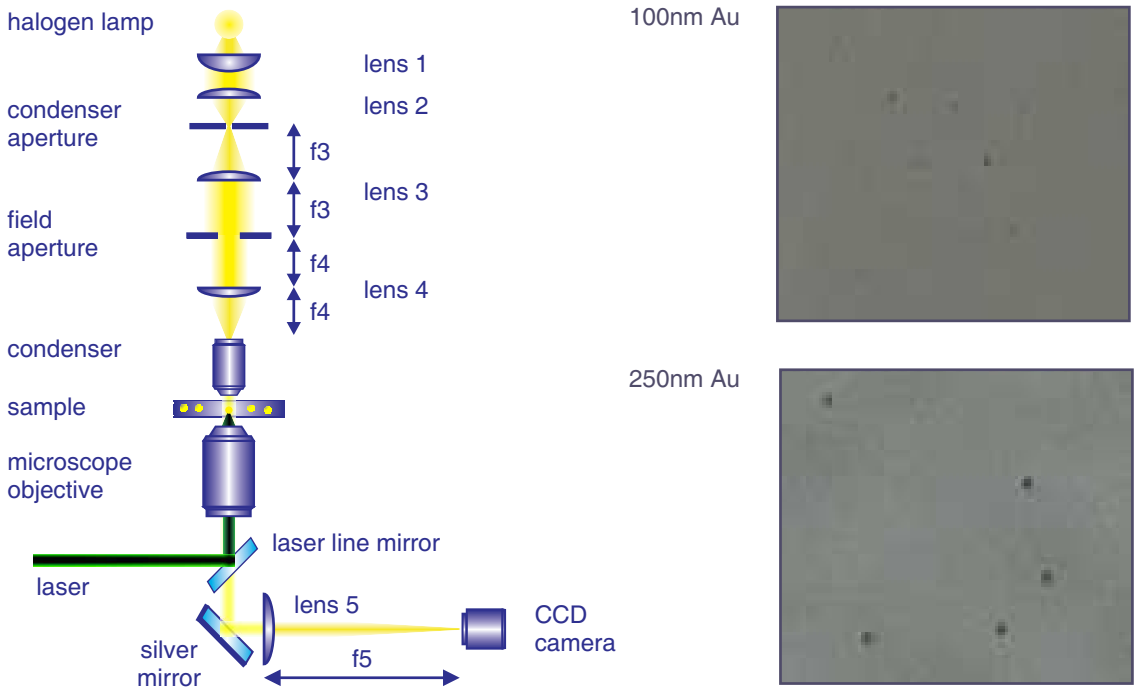

Figure 3.9: *Left* - The Köhler illumination of our inverted trap setup is at the top. Light passes through the condenser (Zeiss, 40x, NA 0.65) and the sample to get recollected by the trapping objective (Nikon Plan, 50x oil, NA 0.9) and then imaged onto the CCD (Watec, WAT250D) camera. *Right* - These two pictures are samples showing 100nm (top) and 250nm (bottom) gold spheres imaged in diascopic brightfield illumination. This technique is not suitable for nanoparticles smaller than 100nm.

maximal contrast and resolution. In the simplest case, Köhler illumination includes a condenser and a field aperture, a collector and focussing lens as well as a condenser lens or objective. Figure 3.9 explains the illumination path in more detail.

We extended our system with two lenses to collect more light from the fibre illuminator (150W, Thorlabs OSL1) and to position the condenser aperture precisely. The fibre illuminator is imaged by a two lens system (lens 1 and lens 2) on the condenser aperture. The condenser aperture is adjustable to set the contrast required for the sample. As we show in Fig. 3.9, lens 3 and lens 4 image the condenser aperture into the back focal plane of the condenser objective (Zeiss, 40x, NA 0.65). This allows us to position an image of the condenser aperture in the correct place which may even lay inside the objective body, depending on the objective used. The second aperture is the field aperture which is a focal length away from each lens either side. The field aperture is seen sharply in focus in the sample plane if the condenser objective is at the correct working distance away from the sample. After passing the sample, the illumination beam is recollected by the trapping objective (Nikon Plan, 50x oil, NA 0.9) and subsequently imaged with a lens on a CCD camera

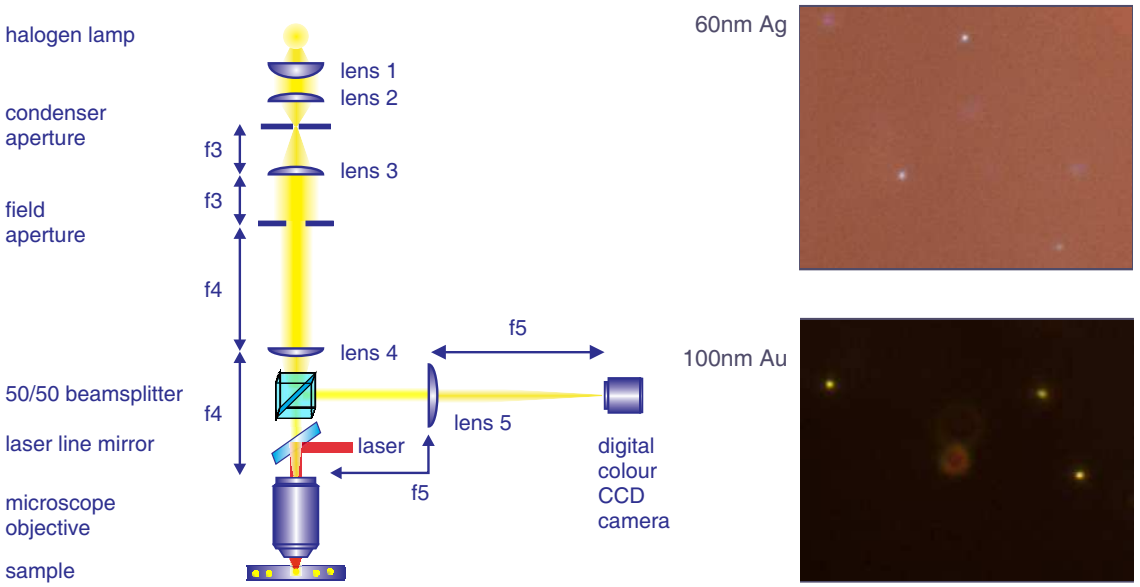

Figure 3.10: *Left* - This diagram shows an upright tweezers system with brightfield Köhler illumination in reflection. One microscope objective is sufficient to image and trap the metal nanoparticles. The sample stage is the only component of the system with three dimensional position adjustment; the rest is fixed. *Right* - Two sample pictures demonstrate the versatility of this imaging system. In both cases the particles are freely floating in solution, neither fixed nor trapped. We simply change the opening size of the apertures in the light beam path to switch between brightfield and darkfield-like (see also Sec. 3.3.3) illumination.

(Watec, WAT250D).

We used this form of illumination for our ringtrap experiment (see Chapter 5). At this stage we only experimented with 100nm gold particles (see sample pictures in Fig 3.9). The diascopic brightfield microscopy is just about powerful enough to visualise metal nanoparticles of this size. However, we did encounter difficulties during video detection caused by the low contrast. Therefore we continued investigating other illumination techniques to further improve our imaging.

3.3.2 Brightfield microscopy in reflection - episcopic illumination

In this section we revive an imaging technique that seems rather basic at first but turns to be the best and most practical solution for imaging optically trapped metal nanoparticles. We use brightfield Köhler illumination of our sample as discussed before but instead of looking at our sample in transmission, we imaged in reflection. To our knowledge this technique has not been used in trapping experiments with metal nanoparticles to date. Based on a single microscope objective, the optical setup is simplified and the imaging quality improved tremendously at the same

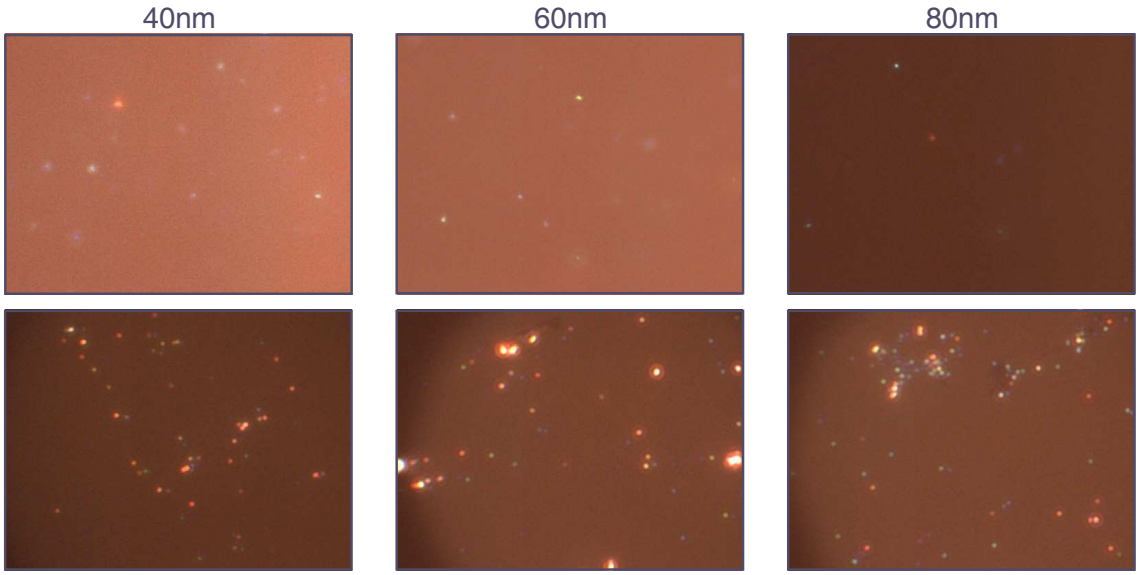

Figure 3.11: We imaged 40nm, 60nm and 80nm silver nanospheres moving freely in solution (top row) and fixed on a glass coverslip (bottom row). The fixed particles are easier to image as they are all in the same plane and thus in focus simultaneously. We also imaged freely moving particles in solution to demonstrate the capabilities of this imaging system in a normal experimental situation. Only some particles are in focus, yet still very well visible even the smallest ones (40nm). The colour variation of the particles in the same solution gives an indication of the size and shape variation within the sample (see also Sec. 3.1).

time. Physically, the much improved imaging of metal nanoparticles in episcopic brightfield microscopy is founded in the nanoparticles' specific plasmonic properties that facilitate imaging in a way similar to fluorescence. Imaging is not based on transmitted light; we rely on the back scattering of the metal nanoparticles.

Metal nanoparticles sustain particle plasmons. These can be excited with daylight and lead to enhanced scattering of incident light close to the plasmon resonance. This property is extremely practical as it offers the possibility to image nanoparticles much smaller than the diffraction limit. Compared to fluorescence, the particle plasmon resonance has several advantages. It is an inherent property so we do not need to apply tags to the nanoparticles prior to an experiment. It does not bleach nor blink and the resonance wavelength depends on size, shape and material of the particle. Taking advantage of the particle plasmon for imaging seems an obvious choice, although only few experiments in optical trapping have done this so far using darkfield microscopy [9, 20].

Figures 3.10-3.15 provide sample pictures of our episcopic brightfield imaging technique. The flexibility of Köhler illumination allows us to vary the brightness and contrast settings over a wide range as we demonstrate in Fig 3.10. We were able

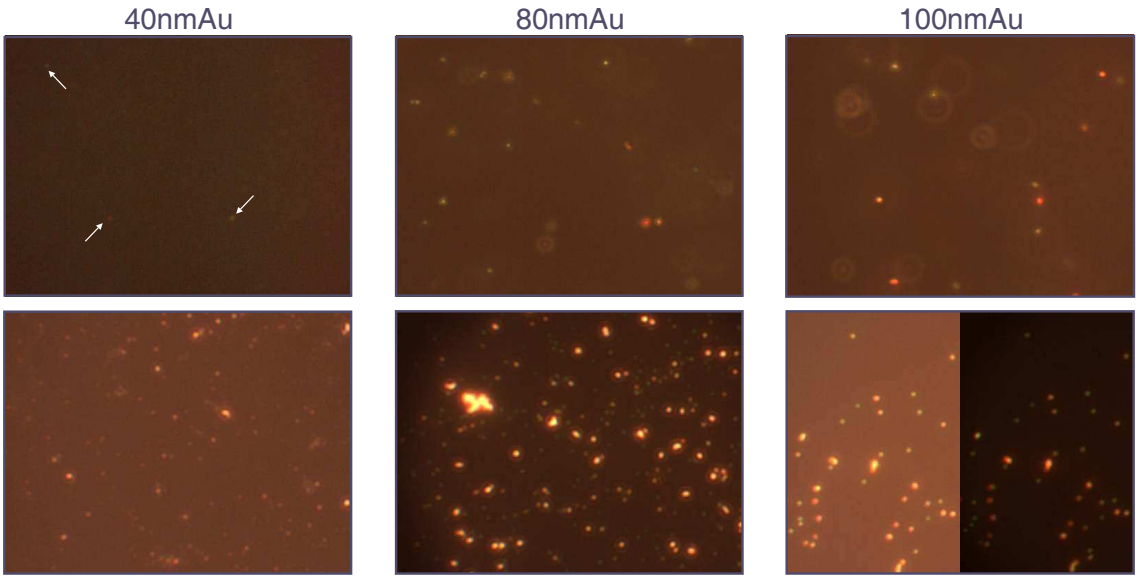

Figure 3.12: The plasmon resonance of gold nanoparticles is less pronounced than the resonance of silver nanoparticles. It is thus slightly harder to visualise gold nanoparticles and the colour of the resonance is not as obvious. Again, it is easier to image fixed nanoparticles (bottom row) as they are all in the same plane than freely moving ones (top row). We show samples of 40nm, 80nm and 100nm gold spheres. The pictures of the fixed sample appear redder than the moving ones as there are more aggregates forming which shifts the resonance. The pale green spots are single gold spheres. The fixed 100nm sample picture compares the bright-and darkfield setting for the same sample.

to image silver and gold particles as small as 40nm. During a trapping experiment the particles float freely in the 90μm deep sample chamber. Therefore we only see a tiny fraction of particles in or close to the focal plane and the sample seems almost empty as shown in the top row of Fig. 3.11 and Fig. 3.12. The colour variation from blue to red of the silver sample is very clear and stems from the large shape and size variation of the silver nanoparticles. For imaging purposes we also fixed nanoparticles on the bottom glass coverslip. These pictures are displayed in the bottom row of Fig. 3.11 and Fig. 3.12. It is a lot easier to image fixed metal nanoparticles as they stay in focus and do not perform Brownian motion.

Figure 3.10 shows a diagram of the imaging and illumination optics for the episcopic brightfield setup. As before, Köhler illumination is the central part of our illumination path. The two apertures give full control of the brightness and contrast adjustment, even to a degree where we are able to obtain darkfield-like images. The condenser objective is the trapping objective at the same time. It is fixed, only the sample stage moves in three dimensions. This reduces the setup by an objective and an x-y-z stage. We insert a 50/50 beamsplitter (Thorlabs) in the illumination path to direct the back reflected image on our CCD camera.

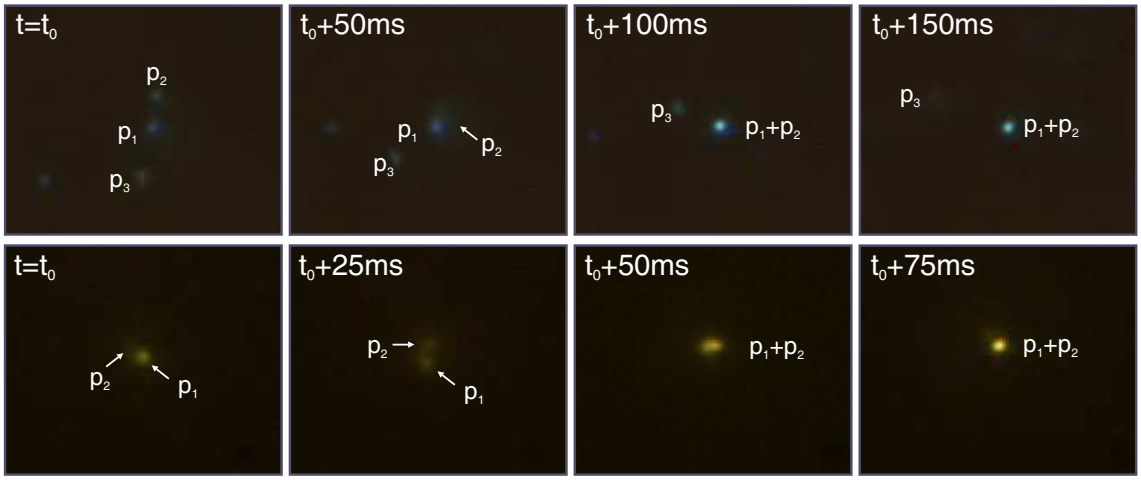

Figure 3.13: Both time sequences show how a trapped particle is joined by a second one in the optical trap. All images are recorded at a rate of 39 frames per second. *Top* - The top row shows snapshots of 60nm silver spheres. Particle p_1 is trapped and subsequently joined by particle p_2. Because both particles are below the diffraction limit we are not able to resolve them once they are both trapped. However, the trap site appears much brighter and slightly greener once the second particle joined in (after 100ms). *Bottom* - A 100nm gold sphere (p_1) is joined by a second sphere (p_2) in the trap. In the first image, particle p_2 is still out of focus and only just visible. In the subsequent image p_1 and p_2 are in the same plane. The moment both particles are trapped, the colour of the trap site red-shifts from green to yellow and appears brighter.

For this experiment we used a digital colour CCD camera (Basler piA640-210gc), taking advantage of the colour dependence of the plasmon resonance. This was particularly useful for our silver samples. Their shape and size distribution is relatively wide spread. A 60nm silver sphere should appear blue. A red particle in the same solution was thus attributed to an elongated (rod) or otherwise shaped (pyramid) particle. This distinction is impossible in transmission microscopy as the particles are much smaller than the diffraction limit. Another advantageous property is the ability to visualise the plasmonic interaction of two nanoparticles close to each other. Trapping more than one particle leads to a colour change, usually a shift towards the red, because of the interacting plasmon resonances of the particles. Figure 3.13 shows a time sequence of a trapped particle which is joined by another particle resulting in a colour change of the trapped object. These attributes were extremely helpful during data acquisition where we had to make sure we only trap one spherical particle. Of course this is only a rough visual guide, small size and shape variations would have to be determined spectroscopically.

Figure 3.13 illustrates the colour change of trapped particles caused by interacting particle plasmons. In both cases the trapped particle is joined by another particle in the trap resulting in a brighter and red-shifted image at the trap site. We present

Figure 3.14: Silver nanoparticles held in a single beam trap with 40nm, 60nm and 80nm diameter (from left to right). The scattered light from the nanoparticle increases with size. The colour of the silver nanoparticles changes from blue to green due to the redshifting of the resonance for larger particle sizes.

more images of trapped silver and gold nanoparticles in Fig. 3.14 and Fig. 3.15, exploiting the dark-field like imaging capabilities of our episcopic brightfield illumination. The trapped particles are sharp and in focus. Particularly the silver particles show an apparent change in colour for increasing particle sizes.

Closing the field aperture in the light path reduces the amount of light entering the objective. The brightness of the image is reduced. We used a high intensity fibre illuminator (150W, Thorlabs OSL1) with variable intensity for our experiment. Its spectrum covered the plasmon resonance of our metal nanoparticles and easily excited the resonance. We thus only needed relatively small amounts of light to get a strong scattering signal form the metal nanoparticles. Closing the field aperture almost entirely eliminated the background illumination. The condenser aperture remained open enough to ensure filling of the back aperture of our objective.

A large fraction of the light reflected from the top glass coverslip of our sample chamber and we always saw a bright image of the field condenser before lifting the sample chamber further up to image the sample itself. Inside the sample the metal nanoparticles are the only source of backscattering as there is no other interface. The resulting image has therefore a strongly reduced background illumination and shows the bright scattering of the plasmon resonance. If the latter is strong enough the field condenser can be closed far enough to produce a darkfield-like image.

Using this illumination technique to produce darkfield-likes images works best for larger nanoparticles (>80nm). The resonance is strong enough to reduce the illumination sufficiently in order to acquire a dark background image and thus large contrast. Smaller nanoparticles are still visible, yet the background remains rather bright (see sample pictures in Sec. 3.3.2). With a dark background, the contrast is even better and the colour of the plasmonic resonance becomes more obvious.

When trapped, the particles remain in focus of the imaging system providing a sharp image of the trap site. We present examples for trapped silver and gold nanoparticles in Fig. 3.14 and Fig. 3.15. We already discussed the advantage of being

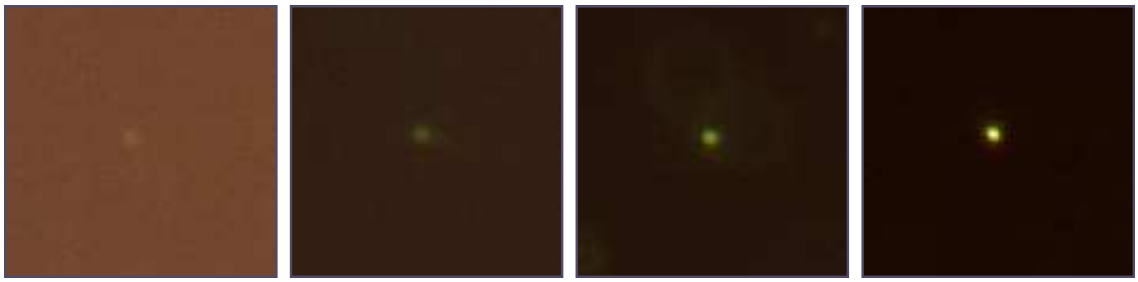

Figure 3.15: Gold nanoparticles trapped in three dimensions with 40nm, 60nm, 80nm and 100nm diameter (from left to right). Gold nanoparticles are harder to visualise than silver nanoparticles because their resonance is not as pronounced and more damped than silver's. With increasing particle size the scattering becomes stronger and we were able to increase the contrast by reducing the background illumination. The colour changes from green to yellow, being redshifted by the increasing particle size.

able to see the colour of the particles. This is one way of directly distinguishing if the trapped particle has the expected dimensions. Larger and non-spherical particles have a red-shifted resonance. Trapping 60nm silver spheres should give an image of a blue spot in the trap. If the spot is green or even red we either trapped a rod or several particles at once.

3.3.3 Darkfield microscopy

Darkfield microscopy is a special imaging technique to render transparent and unstained objects visible, particular if their size is below the diffraction limit. It is also employed investigating plasmonic properties of metal nanoparticles [62–64]. Only light scattering off optical discontinuities such as media boundaries or edges contributes to the image, unscattered light is not collected by the viewing objective. The resulting image shows the bright structures of the object of interest on a contrasting dark background. Darkfield imaging is achieved either in transmission or reflection. Reflective darkfield microscopy requires specialised objectives with outer and inner beam paths as well as special darkfield cubes (mirrors with circular clearance in the centre) in the illumination beam path. We used transmission darkfield imaging as pictured in Fig 3.16.

In a standard darkfield configuration, an aperture blocking the central part of the illumination is placed in the beam path. The condenser focuses a hollow cone of light into the sample chamber. With no sample present the light rays miss the viewing objective and the field of view remains dark. Inserting a sample at the tip of the inverted hollow light cone scatters the incident light at the sample. The scattered light is collected by the viewing objective while the oblique illumination of the hollow cone keeps missing the objective. We used an oil immersion darkfield condenser from Nikon (NA 1.20-1.43) for our experiment. There are more sophisti-

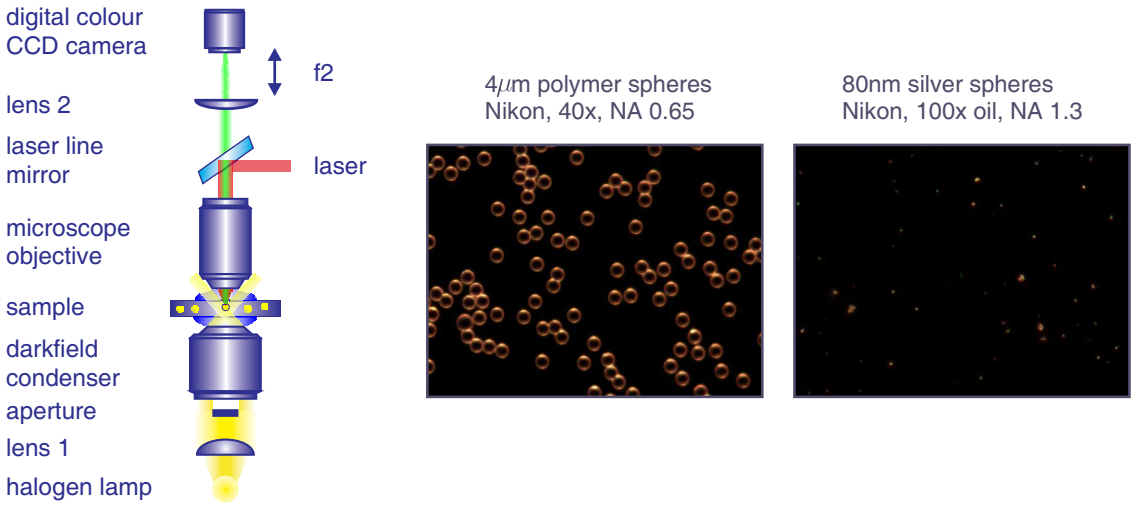

Figure 3.16: *Left* - The diagram pictures the illumination beam path for darkfield microscopy in transmission. The central part of the light beam is blocked before it enters the darkfield condenser. The so-created hollow cone of light is then focussed into the sample chamber where it scatters off the metal nanoparticles. The scattered light enters the viewing objective while the direct illumination misses it. We use the viewing objective as trapping objective at the same time. *Right* - We present two sample pictures acquired with our darkfield setup. The 4μm polymer spheres are imaged with a 40x objective (Nikon Plan Apo, NA 0.65). The 80nm silver spheres are imaged with a 100x objective (Nikon CFI Plan Fluor, oil, NA 0.7-1.3) which we used for trapping later on.

cated systems available to improve the quality of the image, in particular for high NA applications [65, 66].

Regardless of the darkfield condenser used, it is critical to match the condenser and the viewing objective. The best darkfield condenser is ineffective if the NA of the viewing objective is larger than the NA of the darkfield condenser. The direct illumination is then collected by the viewing objective and no dark background can be achieved. To optically trap metal nanoparticles we use a trapping objective with an NA as large as possible in order to focus the trapping laser as tightly as possible. The trapping objective is necessarily the viewing objective in a darkfield configuration as the darkfield condenser block would disturb the laser beam path. Keeping all these factors in mind, we find that despite aiming for the largest NA possible for our trapping/viewing objective we have to keep it smaller then the NA of the darkfield condenser.

In our experiment we used a Nikon oil immersion darkfield condenser (NA 1.20-1.43) and an oil immersion Nikon CFI Plan Fluor 100x objective (NA 0.7-1.3 adjustable). There have been trapping studies with lower NA objectives, but these only investigated optical trapping of metal nanoparticles in two dimensions as real three dimensional trapping cannot be achieved with low NA objectives [9]. We achieved

3D trapping of metal nanoparticles while imaging with the above described darkfield illumination (as pictured in Fig. 3.16). However, we do not consider this kind of darkfield illumination practical to use in conjunction with optical trapping, mainly because of two reasons. First, the sample is enclosed by two oil immersion objectives. That renders a sample exchange rather delicate and introduces additional aberrations of the oil films (the oil for the darkfield condenser was very viscous). Second, the only way to add a quadrant photodiode to this system for position detection (see Sec. 3.4.2) is in back reflection. It turns out that this type of particle detection is already difficult enough for metal nanoparticles in a forward scattering configuration and practically impossible in a back scattering setup.

We thus proceeded in a different way to image metal nanoparticles in an optical trap. The best way of illuminating metal nanoparticles while trapping them turned out to be the brightfield episcopic imaging system we described in the previous section. Brightness and contrast are adjusted as described before with the condenser and field aperture of the Köhler illumination beam path. Including Köhler illumination in our setup ensures the best possible illumination providing an evenly illuminated field of view as well as best possible contrast and resolution.

3.4 Detecting nanoparticles

So far we discussed methods to visualise metal nanoparticles. To determine their behaviour in the trap we need to characterise their motion quantitatively. Position sensing of a trapped particle is used to measure its displacement in a trap and even the applied force on the object. The latter can be deduced from the displacement over time as explained thoroughly in section 4.1.

Video imaging is only one technique for position sensing. Because of its simple practicality it is often used in the field of optical trapping, in particular with large micron-sized objects. However, imaging nanoparticles is challenging and the convenient analysis of the optically tweezed particle by recording a video sequence and subsequently particle tracking the motion is not suitable any longer. Even advanced video analysing techniques [67] that would in principle be applicable to the demands of nanometre-sized particles, fail if the object of interest is hardly visible.

In addition to imaging, the speed of data acquisition plays an important role as well. The trap stiffness and corner frequency of metal nanoparticles are larger compared to micron-sized dielectric beads. Consequently the data acquisition rate has to be faster. Standard CCD cameras record at 30Hz (30 frames per second) and are thus only suitable to track the large scale motion of metal nanoparticles over long time periods. We require exact position measurements for trap stiffness analysis which can be accomplished with either a high-speed camera or a quadrant photodiode (QPD). High-speed cameras with kHz frame rates compare with QPD precision for micron-sized trapped particles, however they decrease in accuracy as

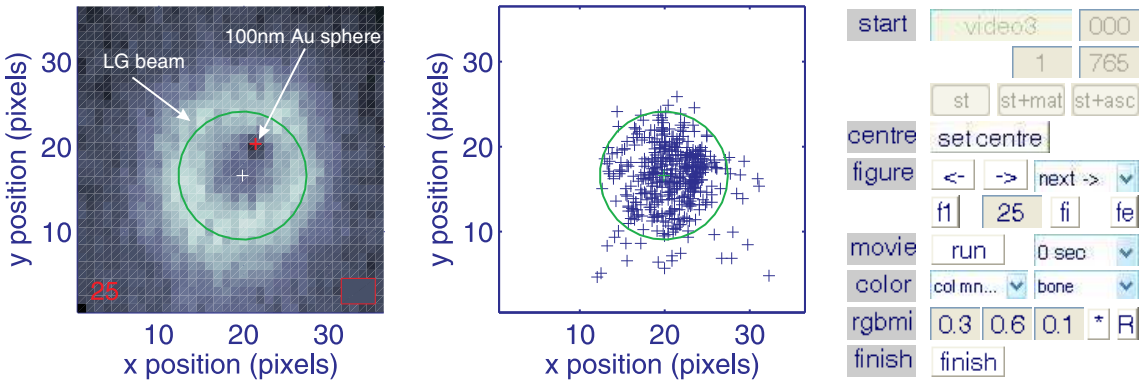

Figure 3.17: This screenshot of our Matlab programme demonstrates our particle tracking routine. We converted the video frames into a stream of bitmaps and individually analysed these as displayed on the left. By adjusting the colour mode and contrast setting of the bitmap (control panel on the right) the 100nm gold nanoparticle is easier to distinguish. The green ring is the position of the Laguerre-Gaussian beam. We plot the particle's position with respect to the Laguerre-Gaussian trap of all tracked frames in the middle graph. This position data is subsequently read out to a data file.

the trap stiffness increases [67] . It has yet to be explored if high-speed cameras are as suitable for metal nanoparticle tracking as QPDs.

We discuss video detection in more detail in the first paragraph of this section. Subsequently we present the second method to detect a particle's motion in a trap; a non-imaging technique utilising a QPD. This is more cumbersome in terms of equipment and data analysis than video detection but provides the immense advantages of much higher bandwidth and eventually better signal-to-noise ratio. The non-imaging technique also provides higher temporal and spatial resolution.

3.4.1 Video detection: Particle tracking

The video detection method described in the following is straightforward to implement and does not require any additional equipment safe the already present CCD camera. We used this technique for our Laguerre-Gaussian trap (see Chapter 5) to record the motion of 100nm gold spheres. We were interested in the positions visited by the trapped particle over time and did not aim to perform precision measurements of applied forces. In this case, video detection was the perfect method to use considering the ease of implementation.

We monitored the particle motion in diascopic brightfield illumination and recorded the image with a CCD camera (Watec, WAT250D) at a speed of 25 frames per second. The recorded video images of the particle motion were then further processed with our own particle tracking software programmed in Matlab. We calibrated the size of each recorded pixel with a stage graticule (see Sec. 3.4.3). Our programme

allowed us to monitor the tracking process frame by frame to avoid false detections. This happened rather easily because the image of one gold sphere only measured 1-3 pixels across and the contrast compared to the background was rather weak. We show a screenshot of out tracking interface in Fig. 3.17. Adjusting the colour mode and contrast of the images helped to recognise and track the particles. We also determined the size of the trap site in the Laguerre-Gaussian beam with this programme.

The accuracy of this method is limited by the image quality. The gold nanoparticles are below the diffraction limit and thus difficult to image anyway. Increasing the image size on the camera would not increase the resolution but may improve the particle recognition for tracking. As we already optimised this kind of illumination for optimal contrast we had no room for improvement in imaging.

3.4.2 Electronic detection: Quadrant photodiode

Detecting the position of a trapped particle electronically with a quadrant photodiode (QPD) is very fast with acquisition rates up to 50kHz. This circumvents the inherent low-pass filtering of video detection which conceals detailed information about the fast moving metal nanoparticles. Therefore we decided to use a QPD for position detection and trap stiffness measurements of our tweezing experiments described in more detail in Chapter 4. Contrary to our Laguerre-Gaussian trap experiment, we aimed to measure the precise position of the trapped particle. The particle was confined to a much smaller space in our tweezing experiments that would have been even harder to detect with video analysis. A QPD is a photo detector made up of four individual photodiodes shaped as quadrants that form a circle. Figure 3.18 shows a picture of the InGaAs quadrant photodiode (infrared sensitive) we used in our experiment.

Implementing a QPD in our setup requires an additional optical train for detection. After passing the sample chamber, the trapping laser is collected by a second objective (Nikon Plan Apo, 40x,NA 0.65). A telescope relays the condenser back focal plane on the QPD (the QPD is in a position optically conjugate to the condenser back focal plane) and matches the size of the back aperture to the diameter of the photo detector. This technique is called back focal plane interferometry and used in most nanoparticle detection experiments [13, 14, 22, 38].

Back focal plane interferometry images the far field interference pattern of the trapping laser and the scattered laser light from the trapped object on the QPD. This method measures the particle's position relative to the trap. As the trapping laser is also the detection laser, large temporal bandwidths are achievable. This is one of the key advantages compared to video detection of trapped particles. Metal nanoparticles with diameters of 80-100nm move very rapidly due to their Brownian motion. Using only one laser to trap and to detect leaves the detection system automatically aligned with the trap. The position of the trap can be anywhere in

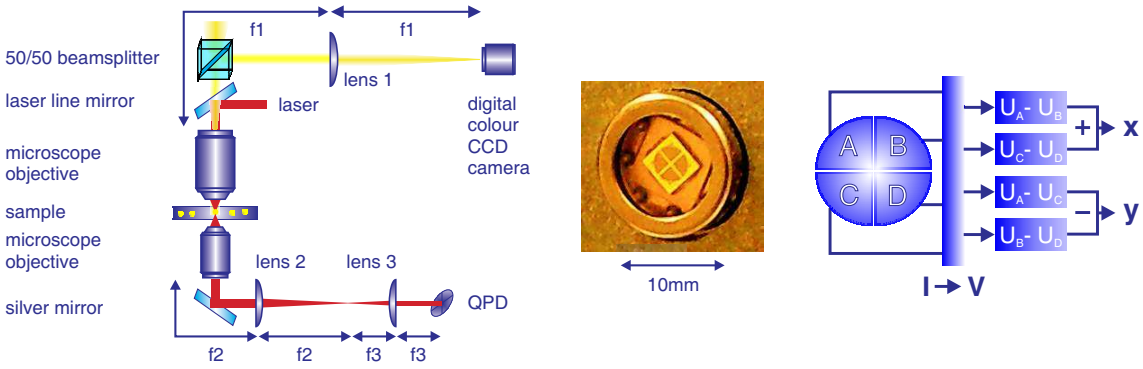

Figure 3.18: We expanded our previously described tweezing setup with a quadrant photodiode (QPD) for electronic detection of particle motion. The diagram on the left shows this addition to the setup. The image in the middle is a photograph of the InGaAs QPD we used. The graph on the right side illustrates the functionality of the photo detector (see also Eq. (3.1)-(3.3)).

the field of view of the detection objective as the interference pattern is a far field effect. All light passing through the focus is imaged onto the QPD.

The QPD converts the output current from each quadrant photodiode to a voltage. The signal of the four quadrants gives precise information about the position of the interference pattern on the QPD. The intensity of the interference pattern is compared in each half (consisting of two quadrants) of the detector, vertically and horizontally. If the interference pattern is perfectly symmetrical and exactly positioned at the centre of the QPD, the x and y values (see Eq. (3.1)-(3.3)) are zero. Displacements of the trapped particle in x and y result in lateral intensity shifts in the interference pattern. Therefore we obtain the position data of the trapped particle by adding and subtracting the individual voltages as follows:

$$U_x = \frac{(U_A + U_C) - (U_B + U_D)}{U_A + U_B + U_C + U_D} \tag{3.1}$$

$$U_y = \frac{(U_A + U_B) - (U_C + U_D)}{U_A + U_B + U_C + U_D} \tag{3.2}$$

$$U_z = U_A + U_B + U_C + U_D \tag{3.3}$$

The x and y position values are normalised with the total voltage of all four quadrants (z coordinate). The sign of x and y indicates the direction of the displacement. The QPD measurement is precise for position detection provided the voltage response of the QPD is linear to the intensity. It is possible to detect the movement in z direction, which may require additional adjustment, depending on the system [68]. We acquired the voltage data for all three coordinates with our own LABVIEW programme. The subsequent data analysis is discussed in detail in

Chapter 4. Calibrating the QPD enabled us to assign real physical units of length to the position data which is delivered in volts by the QDP.

We would like to point out some specific challenges connected with nanoparticle position detection. The amount of light interacting with the nanoparticle is a lot smaller than for a large micron sized bead. The scattered and refracted light is the laser light that interferes with the unperturbed trapping beam and hence gives the information about the position of the trapped object. As the interacting laser light for particles of nanometre dimensions is only a fraction of the unperturbed beam, the signal containing the relevant position information is thus only a fraction of the laser light impinging on the QPD. A good signal to noise ratio is therefore essential to pick up this relatively weak signal containing valuable information.

The z position of the trap influences the detection of the trapped particle's movement and subsequent data analysis. The deeper the trapping position is inside the sample chamber, the more aberrations occur at the trapping focus. Therefore the trap deep inside the sample is weaker compared to just below the top coverslip. However, trapping too close to the sample coverslip leads to interference with back reflections from the coverslip and a significant change in the particle's viscosity [69]. As the aberration of the focus and thus the deterioration of the trap can be corrected by using the appropriate immersion oil for the trapping objective [57] we were able to trap 10μm away from the top glass coverslip. The particle's diameter (80-100nm) was thus negligible in comparison to this distance and we did not need to include hydrodynamic corrections (Faxen's law) in our data analysis. We aimed to trap the particle at the same depth at all times to obtain comparable measurements.

We made an effort to eliminate noise from the system in order to achieve the best possible signal to noise ratio. We took a dark spectrum (power spectrum of the position data with the laser switched off) to measure the electronic noise of our system. This turned out to be negligible. However, electronic noise is not the only noise in the system. Mechanical (and even acoustical) noise is transmitted via the sample solution onto the sphere and can only be seen in the final motion of the trapped particle. We tried to circumvent mechanical noise sources by floating the optical table and taking measurements out of normal working hours when the building was quiet.

The largest source of noise to our system turned out to be the laser itself. We measured the light spectrum (power spectrum of the position data), with only the laser beam shining on the photo detector without a particle in the trap, to check for beam pointing instabilities. Significant contributions in the low frequency regime (<20Hz) indicated low pointing stability. By replacing the QPD with a camera for a test we were able to see movements of the entire interference pattern and hence the laser beam in space from time to time. As the beam remained stable for seconds in between movements, this was not a problem for the trap stiffness measurement (see Chapter 4) because the data acquisition only took 5s at the longest. However, to calibrate our QPD with a nanopositioning stage turned out to be impossible as

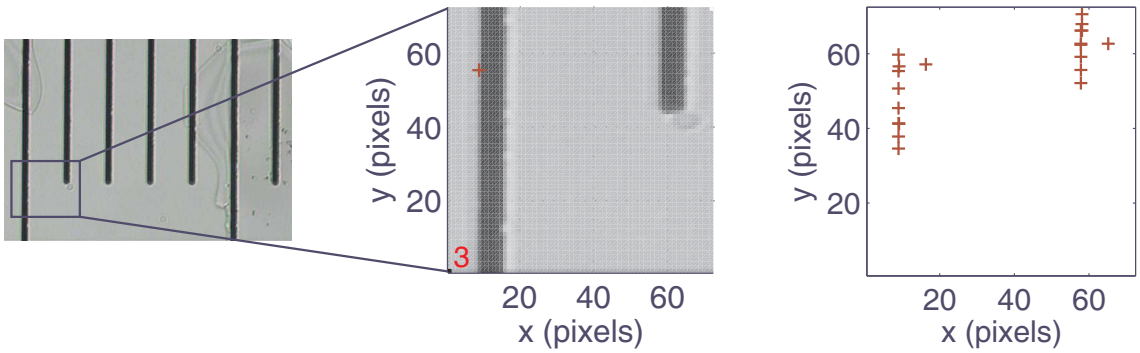

Figure 3.19: We analysed a section (left) of an imaged grid ruler (Comar, 11GG76) with our particle tracking programme to allocate a physical length scale to each pixel. The graph on the right shows a summary after analysing several different images to minimise errors. In this example 1 pixel equals 200nm.

this requires the beam to remain stationary for at least a couple of minutes (see the following section).

3.4.3 Calibrating the detection system

The presented detection techniques both require calibration to attribute meaningful physical units of length to the position data. For video detection we have to convert pixels from the video image to a metric distance. The electronic detection with the QPD gives out voltages which we convert to nm as well. There a several ways to calibrate a QPD, we present a selection of methods in the second half of this section.

The calibration of the video detection system is comparatively simple. We inserted a grid ruler (Comar, 11GG76) in the sample plane and subsequently used our particle tracking software to determine the distance of the grids in pixels (pictured in Fig. 3.19). Knowing the exact distance in nm from the manufacturer of the grid ruler, we are able to derive the relationship between pixels and nm. In our experiment 1 pixel equals 200nm. The calibration is specific to each condenser and trapping objective configuration we used.

There a several ways to calibrate a QPD detection system, all with their own advantages and precision [69]. Nowadays it is common to calibrate the photo detector with the help of a piezo nanopositioning stage. This method is very accurate and does not require the knowledge of sample parameters such as the local temperature or viscosity.

We fitted a piezo nanopositioning stage (Physikinstrumente (PI), P-733.3 XYZ) directly on top of our microscope stage with custom built adapters. Immobilising a previously trapped particle on the bottom glass coverslip of our sample chamber provided the point of reference for the calibration measurement. We drove the piezo stage holding the sample chamber at known steps, scanning the stuck particle

through the focus of the trapping beam and simultaneously recording the voltage signal from the quadrant photodiode. As a result we obtained position-related voltage data for the stuck particle instead of the motion data of a trapped particle. We controlled these procedures with our own LABVIEW programme.

To analyse the so acquired data we compared the experimental QPD data with the theoretically expected interference pattern. The theory of position sensing using the forward scattered light has been discussed in detail elsewhere [54,70]. It is possible to explain the intensity changes in the back focal plane of the condenser objective with minimal interference calculations. Assuming a Gaussian beam propagating through the sample and the particle to be a Rayleigh scatterer is sufficient to obtain results with good accuracy [71]. For the one-dimensional case, the signal on the QPD is theoretically predicted to be [54]

$$\frac{\mathrm{I_x}}{\mathrm{I}}(\mathrm{x}') = \frac{16\mathrm{k}\alpha}{\sqrt{\pi}\mathrm{w}_0^2}\left(\frac{\mathrm{x}'}{\mathrm{w}_0}\right)\mathrm{e}^{-\left(\frac{\mathrm{x}'}{\mathrm{w}_0}\right)^2}. \tag{3.4}$$

$\mathrm{I_x}$ refers to the x signal from the QPD and x' is the displacement of the immobilised sphere. The detector response is a function of the particle's polarisability α according to the Clausius Mossotti approximation (see Sec. 2.2.2), the wavenumber $\mathrm{k} = |\mathrm{k}| = 2\pi\mathrm{n}_{\mathrm{host}}/\lambda$ and the beam-waist radius in the focus w_0.

The two-dimensional expression for the detector response is best expressed in cylindrical coordinates [54]:

$$\frac{\mathrm{I_x}}{\mathrm{I}}(\rho', \phi') = \frac{16\mathrm{k}\alpha}{\sqrt{\pi}\mathrm{w}_0^2}\,\cos\phi'\,\left(\frac{\rho'}{\mathrm{w}_0}\right)\mathrm{e}^{-\left(\frac{\rho'}{\mathrm{w}_0}\right)^2} \tag{3.5}$$

with the displacement ρ' at an angle ϕ' in the focal plane (z=0).

We fitted Eq. (3.5) to the acquired position data of the stuck particle by varying the beam-waist radius w_0 and the prefactor $\mathrm{b} = \frac{16\mathrm{k}\alpha}{\sqrt{\pi}\mathrm{w}_0^2}$. That way we did not rely on accurate values for the polarisability α of the nanoparticles which would have been difficult to obtain in our case (see the discussion in Sec 2.3.3). Figure 3.20 shows the data and the fitted graph (Eq. (3.5)) of the QPD signal recorded for a 80nm gold particle. We moved the nanopositioning stage at a step rate of 100nm in two dimensions (x and y) and averaged the QPD signal over 0.2s at each step. As the QPD measures the farfield interference pattern and not the image of the gold sphere, the sphere's position is in the middle between the two maxima of the voltage signal. The linear slope between the two maxima is the calibration factor linking the voltage of the QPD with a metric length scale.

The data set presented in Fig. 3.20 is only one of very few that is usable for detector calibration. Unfortunately the laser was unstable most of the time and we were not able to take measurements as presented in Fig. 3.20 repeatedly. We tested our system by recording data sets with no stuck particle in the beam. Instead of recording a regular flat signal as expected, we generally obtained very noisy data.

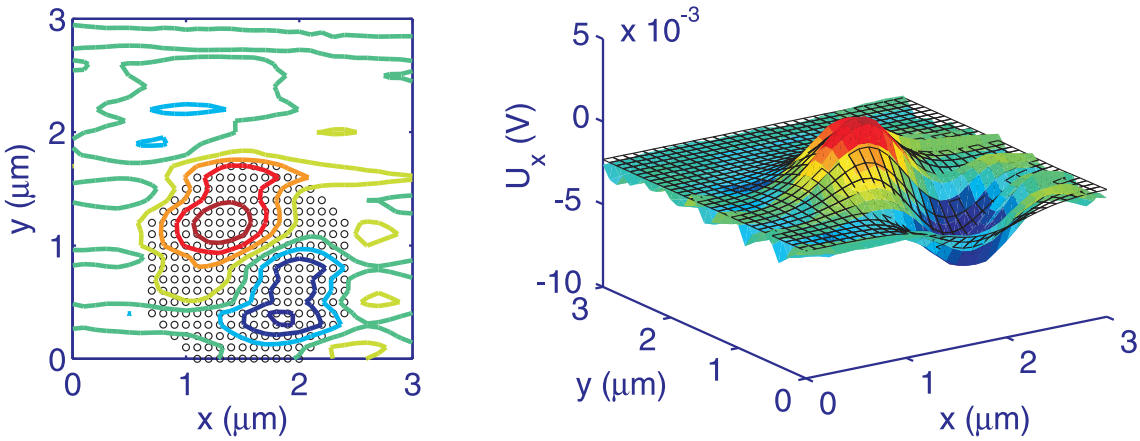

Figure 3.20: *Left* - The experimentally obtained QPD signal for U_x (Eq. (3.1)) is displayed in colour. The black circles indicate the fitting range. *Right* - We fitted the theoretical detector response of Eq. (3.5) plotted as black mesh to the QPD data (colour). The z axis shows the value of U_x at each x and y position in space. The signal is obtained from a 80nm gold sphere stuck to the bottom glass coverslip. At each step we averaged the QPD signal for 0.2s and scanned the stage at 100nm steps across the area of the stuck particle.

The voltage outputs were rising or falling over time, indicating significant movement of the laser beam itself.

Consequently we chose a different technique to calibrate the QPD in our setup. We decided to combine the power spectrum analysis and the equipartition theorem. Both methods deliver an independent value for the trap stiffness of the same measurement in complementary units. The trap stiffness result from the power spectrum analysis is given in J/m^2 and the trap stiffness calculated with the equipartition theorem is given in J/V^2. As both techniques are applied to the same data set, both trap stiffness values have to be identical. The conversion factor to link both values is the required calibration factor, providing the relationship between voltage from the detector and displacement in metres of the particle in the trap.

In the following Chapter we are going to discuss the variables and data analysing techniques in much greater detail. In this paragraph we briefly describe only the equations necessary for calibration. The raw data from the QPD of a trapped nanoparticle gives voltage values for all 3 directions in space: U_x, U_y and U_z (see Eq. (3.1)-(3.1)). These positions are normally distributed over time and we are able to determine the variance σ_x^2 for the distribution of position in x direction. According to the Equipartition theorem (see Sec. 4.2.3), the variance is linked to the stiffness κ_{Equip} of the optical trap as

$$\sigma_x^2 = \frac{k_B T}{\kappa_{\text{Equip}}}. \tag{3.6}$$

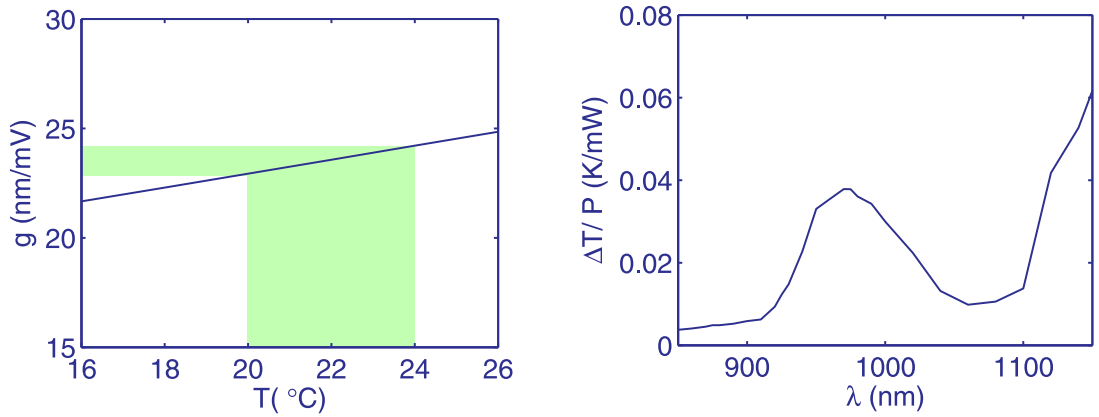

Figure 3.21: *Left* - We calculated the temperature dependence of the calibration factor g. Our experiments were all conducted at room temperature (T=22°C). Even assuming a temperature error of ±2°C the calibration factor turns out rather small g=23.6±0.7nm/mV (see highlighted area). *Right* - Water absorption is wavelength dependent. The trapping laser in our experiment spans a wavelength band of 900-1100nm. We calculated the involved heating effect of the sample solution as result of laser exposure (see Eq. (3.10)). This graph shows the temperature dependence of water per mW laser power at the focus over the laser wavelength which turned out to be negligible for our experiments.

This equation includes the temperature T of the sample and the Boltzmann constant k_B. The power spectrum analysis provides the corner frequency f_c of the optical trap which is expressed in terms of the drag coefficient γ and the trap stiffness κ_{Pow}

$$f_c = \frac{\kappa_{Pow}}{2\pi\gamma}. \tag{3.7}$$

The trap stiffness values are linked by the calibration factor g as

$$\kappa_{Equip} = g^2\,\kappa_{Pow}. \tag{3.8}$$

Inserting the equation for the drag coefficient $\gamma = 3\pi d\eta$ with the particle diameter d and the dynamic viscosity of the sample solution η leads to our final equation for the calibration factor:

$$g^2 = \frac{k_B T}{\sigma_x^2 f_c 6\pi^2 d\eta} \qquad \text{with g given in} \frac{V}{m} \tag{3.9}$$

Without a piezo nanopositioning stage available, calibrating the QPD this way is a practical solution as there is no additional measuring equipment required. However we have to be cautious about some aspects of this method. The temperature T and the viscosity η of the solution medium cannot be determined precisely in this experiment. Therefore we have to choose the values for the temperature T and the

viscosity of the medium carefully. The viscosity of the sample medium (water) is temperature dependent and documented elsewhere [72]. In Fig. 3.21 we plotted the calibration factor g over the temperature T, including the temperature dependence of the viscosity. We kept our setup at a constant temperature of T=22°C throughout all experiments. The calibration factor g varies less than 4nm/mV over a 10°C temperature range. Thus we expect an error of 3% for a 4°C temperature fluctuation: T=22±2°C results in g=23.6±0.7nm/mV. This precision is absolutely acceptable for our experiments and we did not investigate further in temperature measurements of our samples.

There have been investigations about significant temperature increase at the trap site when trapping metal nanoparticles [22] that in turn may lead to inaccurate trap stiffness values. Seol et al. also pointed out that these effects are negligible for trapping powers below 50mW. Our trapping powers only ranged from 25-40mW and we thus assume that there are no heating effects upon the metal nanoparticles.

However, Seol et al. did not take the heating of the sample solution into account as this is known to be very low for laser wavelengths at 1064nm. In our experiment we used a broad band from 900nm-1100nm of laser light. Therefore we calculated the laser induced heating of the sample medium (water) at the focus including the wavelength dependent absorption of water according to [73]. The temperature change ΔT over trapping power P is given as

$$\frac{\Delta \mathrm{T}}{P} = \frac{\alpha}{2\pi \mathrm{C}} \Big[\ln(2\pi \frac{\mathrm{R}}{\lambda}) - 1 \Big], \tag{3.10}$$

with the extinction coefficient α of water, the thermal conductivity for water C=0.6$\frac{\mathrm{W}}{\mathrm{m \cdot K}}$ and the distance of the trap site from the coverslip R=10μm. We see that the maximum heating due to the absorption of water occurs around 970nm and is less than 0.04K per mW laser power at the focus. We never exceeded 40mW laser power at the focus. This equals 0.2mW per 1nm wavelength band of the 200nm (900-1100nm) used. The absorptive heating of water at the trap site is at most 0.8K and can, according to the previous discussion, be neglected in our experiments.

Overall the temperature dependence of this calibration method does not interfere with our experiments. Our focus is the comparison of trap stiffness values for different metal nanoparticles and trapping powers. Assuming a "wrong" temperature would affect all measurements simultaneously and not deteriorate the overall result of our experiments. Other sources of error for calibrating the detection system with this calibration method are inherent to noise factors of the experiment itself. The value of the trap stiffness κ_{Equip} determined with Boltzmann statistics may be too low because the true position distribution might be broadened because of low frequency contributions (mechanical noise). Also, low pass filters can potentially narrow this distribution and lead to a larger trap stiffness [55]. As discussed before we tried to eliminate these factors as much as possible and did not find any significant mechanical noise sources or low pass filtering issues in our data.

3.5 Conclusions

In this chapter we summarised the experimental techniques used for this work. That way we separated technical questions and challenges from the actual physics discussion and result interpretation of the following experiments. We started describing the different trapping geometries we used to manipulate metal nanoparticles. The single beam optical tweezers is an excellent choice to trap metal nanoparticles above their resonance wavelengths. The system we developed is very versatile in choosing a trapping wavelength. By sending a supercontinuum laser source through appropriate optics we were able to deliver wavelengths ranging from 450nm-1100nm to the trap site. We took extra care to trap the particles in 3 dimensions by choosing a high NA objective and the correct immersion oil. The dual beam trap proved to be challenging and not as practical as the single beam trap. The optical setups discussed here provide the basis for our Laguerre-Gaussian trap presented in Chapter 5 which is ideal for trapping metal nanoparticles below their resonance wavelength.

We focussed particularly on the imaging of metal nanoparticles as we are not aware of other works presenting such an easy and straightforward system. Instead of using a complex imaging setup with additional imaging lasers or optical systems such as DIC microscopy, we showed how powerful reflection microscopy is. We were able to image metal nanoparticles as small as 40nm in diameter and obtained additional information about the quantity and shape of particles in the trap by using a colour camera. This method is very practical and easier to use than non-imaging techniques.

We also presented our experiments on transmission microscopy. Brightfield transmission microscopy combined with Köhler illumination enables us to visualise metal nanoparticles down to 100nm. The low contrast of this imaging technique prompted us to investigate transmission darkfield imaging. Although this is a very powerful technique for metal nanoparticle imaging it poses technical challenges when combined with optical trapping. The numerical aperture of the trapping objective has to be as large as possible to ensure 3 dimensional trapping. At the same time it has to remain smaller than the darkfield condenser in order to avoid collecting the direct illumination of the sample. We aimed to image and trap metal nanoparticles smaller than 100nm at the same time and thus proceeded to reflection microscopy. This turned out to be the best technique for our experimental needs. We were able to image metal nanoparticles as small as 40nm while trapping them in 3 dimensions.

Finally we discussed the relevant detection systems and how we recorded the motion of the trapped particles. Although video detection is more common for micron-sized objects, metal nanoparticles are more precisely monitored with quadrant photodiode (QPD) detection. We employed video detection to track large scale motion of metal nanoparticles within our Laguerre-Gaussian trap over extended periods of time. For this analysis the precision of the video images was adequate. We subsequently tracked the particle positions with our own custom made software in

MATLAB. Our trap stiffness measurements, which we discuss in the following chapter, required higher precision at large data acquisition rates. We chose back focal plane interferometry and added a QPD to our trapping system. We took great care to eliminate noise during our measurements as the signal to noise ratio is critical for nanoparticles.

In the last part of this chapter we examined different calibration techniques for our detection systems. We used a grid ruler for the video analysis to assign a metric quantity to the pixels of the video image. The calibration of the QPD proved more challenging. We originally chose a nanopositioning stage to calibrate the QPD. However the pointing stability of the laser turned out to be insufficient. We proceeded by combining power spectrum analysis with the equipartition theorem. These methods both provide values for the trap stiffness in complementary units. Here we had to take the temperature and viscosity of the sample solution into account. Therefore we analysed potential heating effects of our experiment and came to the conclusion that these are negligible in our experimental conditions.

In the following two chapters we present the experiments done with the here described methods and techniques. By discussing the technical aspects beforehand we now focus on the physics and interpretation of our results.

4 Optical trapping above resonance

Conventional single beam tweezers are a very popular tool for optically manipulating a wide range of objects - atoms, molecules, nanoparticles, micron-sized spheres, cells - to name only a few. The object of interest is held in the high intensity region of a tightly focussed Gaussian beam. Although the single beam trap has been invented more than 20 years ago, optical tweezing of metal nanoparticles was only demonstrated a decade later and is still regarded as difficult [8–10]. Currently there are no more than a few groups worldwide successfully trapping metal nanoparticles in 3 dimensions [10, 14, 22].

In Chapter 2 we investigated theoretically the forces applied to a particle in an electromagnetic field. Although quantitative force calculations for metal nanoparticles are complicated, the ideas discussed in Chapter 2 give us a qualitative indication about trapping forces [18]. However, experimental insight into the force mechanism close to the particle's resonance would be beneficial to help finding a suitable theoretical description. Despite their high reflectivity and large scattering cross section, we expect metal nanoparticles to trap better than their dielectric counterparts of similar size using a trapping laser in the infrared. We attribute this effect to the larger polarisability of metal nanoparticles.

In this chapter we present the results of our tweezing experiments - optical trapping of gold and silver nanoparticles. By trapping above resonance we mean that the wavelength of the trapping laser is longer than the wavelength of the trapped particle's plasmon resonance. This is sometimes referred to as red-detuned optical trapping (analogous to atom trapping). The plasmon resonance is situated around 400nm for silver and 550nm for gold nanospheres. We expose our 80nm gold and silver spheres to laser light far from resonance using a wavelength in the infrared (900-1100nm) forming our optical trap. In this wavelength range the metal nanoparticles act similarly to an absorbing dielectric particle with a high refractive index.

Over the past 4 years, this kind of nanoparticle trapping has been extensively investigated with respect to the particle size of gold and silver by Lene Oddershedde's group [13, 14, 38]. In addition to optimising the optical trap for metal nanoparticles, they also developed a detailed detection and characterisation setup [55], providing a solid basis for further research. So far, all experiments tweezing metal nanoparticles in 3 dimensions have been conducted with a continuous wave, infrared laser far from the plasmonic resonance of the particle. We used a pulsed supercontinuum laser source for our experiments. We started with the infrared part of the supercontinuum spectrum intending to change the wavelength of the trapping laser later on to

investigate the trap closer to resonance of the metal nanoparticle. The actual step changing the wavelength of the trapping laser proved difficult as we describe in the end of this chapter.

Optical trappping of metal nanoparticles close to resonance is an area that still requires experimental investigation. The material parameters change significantly close to resonance and we anticipate the trapping behaviour of metal nanoparticles to vary accordingly. Using a red-detuned trapping laser close to resonance we expect to attract metal nanoparticles to the high-intsity region of the laser beam. In this chapter we confirm this behaviour for wavelengths far from resonance in the infrared. We show in the following chapter how blue-detuned laser traps repel metal nanoparticles. In atom optics the intrinsic resonance is crucial to make optical trapping of atoms work. For metal nanoparticles we do not know yet how advantageous or possible trapping close to resonance is. The question remains whether there is an optimal wavelength for trapping a metal nanoparticle, either close to resonance or elsewhere in the optical spectrum.

This chapter focuses on our results for optical trapping of metal nanoparticles above resonance. First we provide a brief summary how to analyse an optical trap. The analysis refers to a mechanical model analogous to a Hookean spring. The restoring force of this system is the total force exerted by the incident laser beam on the trapped particle. We thoroughly discussed its nature and composition in terms of scattering, gradient force components in Chapter 2. We give a short overview how to interpret the data acquired with an electronic position detection system and then finally discuss our results. Optical manipulation below the resonance wavelength of metal nanoparticles is presented subsequently in Chapter 5.

4.1 The single-beam trap

Optical tweezers are a precise tool for measuring small forces. Their great advantage is the restoring force of the trapped particle being linearly proportional to the displacement of the particle. Mechanically, an optical trap is thus analogous to a spring obeying Hooke's law. This gives us the possibility to investigate the strength of the optical trap and hence the restoring force. The restoring force $\mathrm{F_r} = \kappa \mathrm{x}$ with the trap stiffness κ is supplied by the attractive electromagnetic force. More precisely, it is the result of a fine balance of scattering and attractive gradient force components. Only if the restoring force is strong enough, we can actually trap the particle.

The goal is thus to quantify the motion of the particle in the trap with the trap stiffness. This gives us a quantitative idea of the optical force exerted by the Gaussian beam. This force is wavelength dependent for metal nanoparticles. By means of the trap stiffness, we are able to compare the optical trap for varying particles sizes, materials, laser wavelengths and powers to derive more insights in the physical processes present at trapping. In our experiment we trap 80nm and 100nm sized

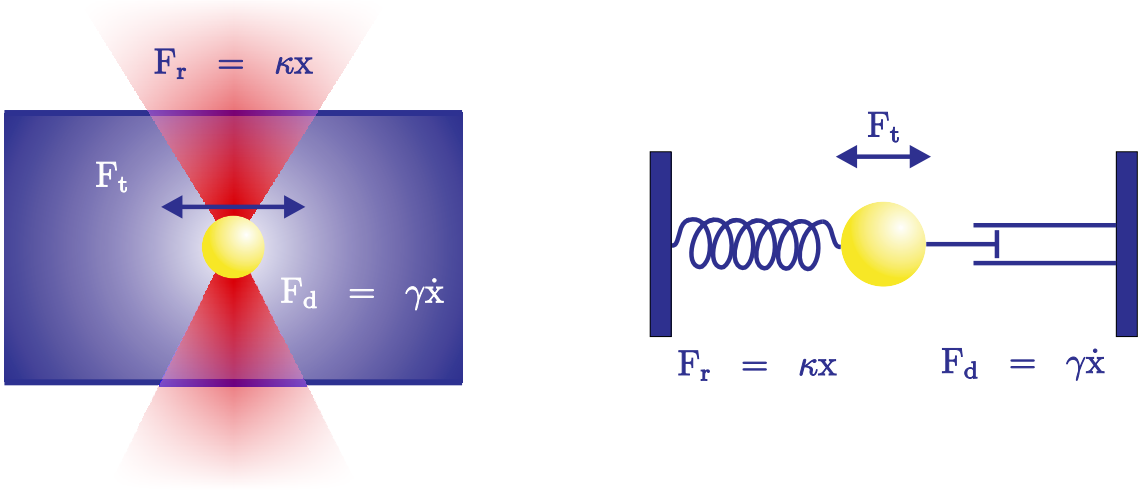

Figure 4.1: *Left* - The cartoon of an optical trap shows the forces we describe with the mechanical model. *Right* - For comparison we sketch a hookean spring: the mechanical analogue of optical tweezers.

metal nanoparticles. The fact they are metal makes them easier to trap as they are highly polarisable and hence have a larger polarisability than dielectric spheres. This property directly influences the gradient force as we discussed in Chapter 2.

The equation of motion of a particle in a trap is modelled by the following equation, describing the displacement x of a particle held in the trap:

$$\mathrm{F_d} + \mathrm{F_r} = \mathrm{F_t}, \tag{4.1}$$

$$\mathrm{m}\frac{\mathrm{d}^2\mathrm{x(t)}}{\mathrm{dt}^2} + \gamma\frac{\mathrm{dx(t)}}{\mathrm{dt}} + \kappa\mathrm{x(t)} = \sqrt{2\mathrm{k_B T}\gamma}\mathrm{R(t)}. \tag{4.2}$$

The right hand side represents the excitation force $\mathrm{F_t}$ pulling the particle out of the equilibrium position. This is a stochastic thermal force, usually the Langevin force, leading to a random Gaussian process describing Brownian motion in a potential with the temperature T, Boltzmann's constant $\mathrm{k_B}$ and a noise term R(t). The second time derivative on the left side of the equation can be neglected as we have an overdamped system. This means we neglect inertial forces because the Reynolds number of the trapped particle is very small. The second term accounts for damping by the viscous drag force $F_d = \gamma\frac{\mathrm{dx}}{\mathrm{dt}}$. The drag coefficient γ is defined by the medium viscosity η and the particle's radius r as $\gamma = 6\pi\eta\mathrm{r}$ (Stoke's law). The damping does not affect the distributions of positions of the particle in the trap but it does affect the behaviour of the particle over time. With the restoring force $\mathrm{F_r}$ we are able to determine the harmonic potential

$$\mathrm{U(x)} = \mathrm{F_r}\cdot\frac{\mathrm{x}}{2} = \frac{\kappa_\mathrm{x}}{2}\mathrm{x}^2. \tag{4.3}$$

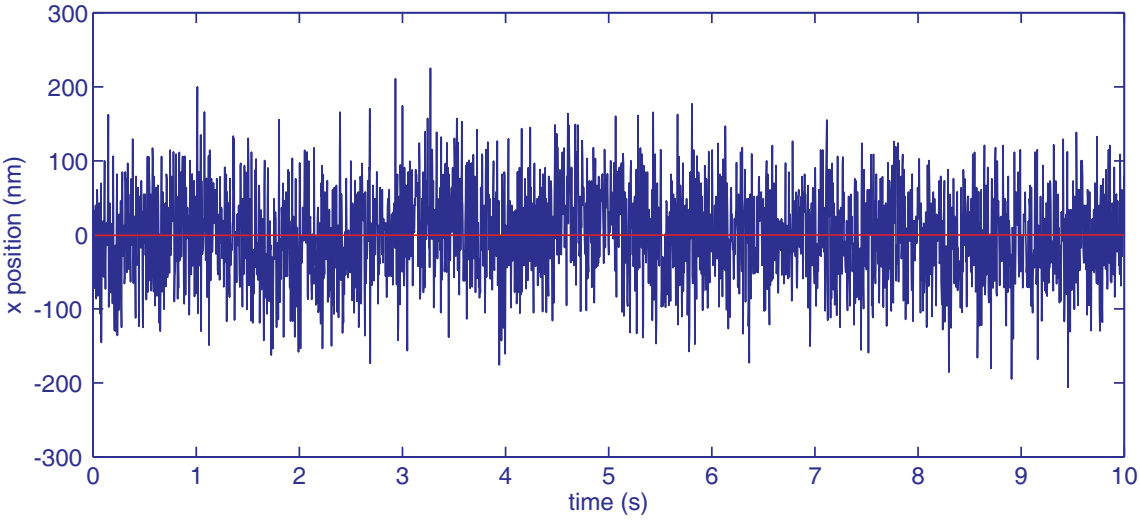

Figure 4.2: We show the raw data of the x position of a 100nm gold sphere trapped over time. In this experiment we used a continuous wave (cw) laser at 1064nm delivering 33mW at the trap site. We recorded the data at 50kHz for 10s but display only a fraction here for more clarity (every 200 points=250Hz).

At the centre of the Gaussian beam trap the potential is approximated by a parabolic potential well. In the one-dimensional case, κ_x is the lateral spring constant of the trap in x direction. The spring constant in y direction is the same if the beam is perfectly circular.

This mechanical model based on a harmonic potential and the linear dependence of the restoring force is the basis for all force measurements. In a stable trapping situation, the total force on the trapped particle in the focus is zero and any small displacement away from this equilibrium points results in a restoring force.

4.2 Characterising the optical trap

We described the technical parts of our experimental setup in Chapter 3. For characterising the optical trap we measure the trap stiffness using an electronic detection system based on a quadrant photodiode. This method is necessary for metal nanoparticles as they are too small and their corner frequency in the trap is too high to be tracked with conventional video techniques. We thus record the voltage change resulting from a signal change on the photodiode as explained in Sec. 3.4.2. The voltage signal gives the position of the particle with respect to the centre of the trap over time. This is the raw data we analyse in the subsequent sections in order to quantify the strength of our trap. Our analysis reveals the trap stiffness κ from the raw data which enables us to compare optical trapping for various power levels, particle sizes and materials. Figure 4.2 shows a sample data set of x positions

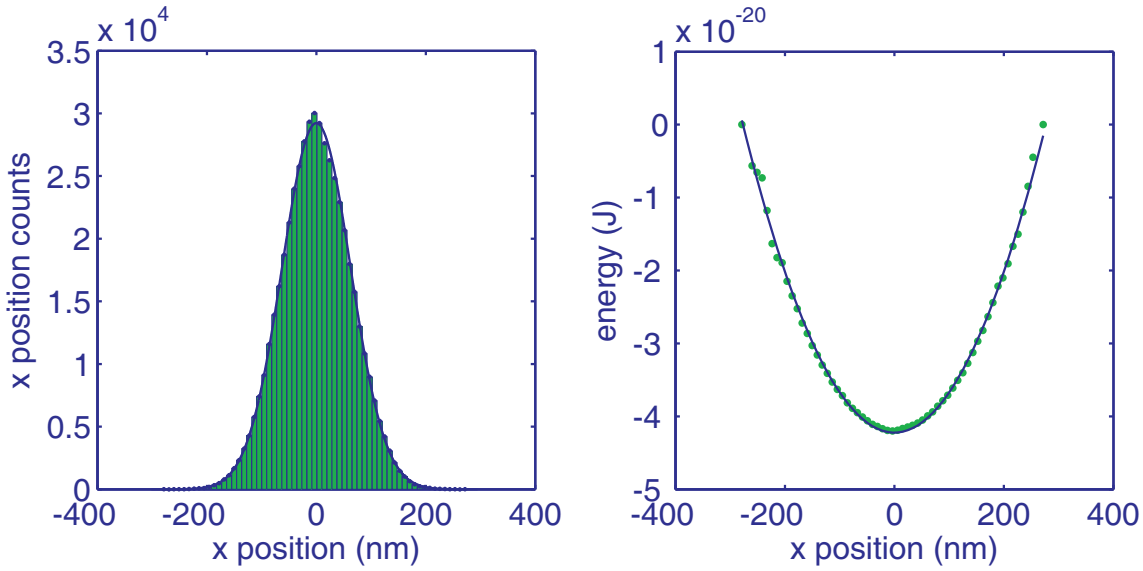

Figure 4.3: *Left* - Here we display the raw data of Fig 4.2 in a histogram using 60 bins. In the next step we fit a Gaussian distribution to the histogram as described in Eq. (4.4). *Right* - Fitting the potential energy of the gold sphere in the optical trap from Eq. (4.3) to the inverted histogram data gives us the trap stiffness κ_x.

visited by a 100nm gold sphere in a trap.

4.2.1 Histograms and potential energy

The distribution of positions of the trapped particle acquired with either a camera or quadrant photodiode is typically displayed in a histogram. The statistical distribution of position over time shows a Gaussian (or normal) distribution. The histogram's probability density function for the one-dimensional case is therefore

$$p(x) = \frac{1}{\sigma_x\sqrt{2\pi}} e^{-\frac{(x-\mu)^2}{2\sigma_x^2}}, \tag{4.4}$$

with the expected value μ and the variance in x direction σ_x^2. Of course this can be expanded for two dimensions as the trap is rotation symmetric for circular beams. We plot the probability density p(x) and the histogram in the left graph of Fig 4.3. The bin width of the histogram does not correspond to the resolution the intensity profile is probed with. We know from Boltzmann statistic that the potential energy U(x) of the particle is distributed as

$$p(x) = Ce^{-\frac{U(x)}{k_B T}}. \tag{4.5}$$

The constant factor C normalises the probability distribution with $\int p(x)dx = 1$ determining the offset of the potential and is usually neglected [69, 74]. The Boltz-

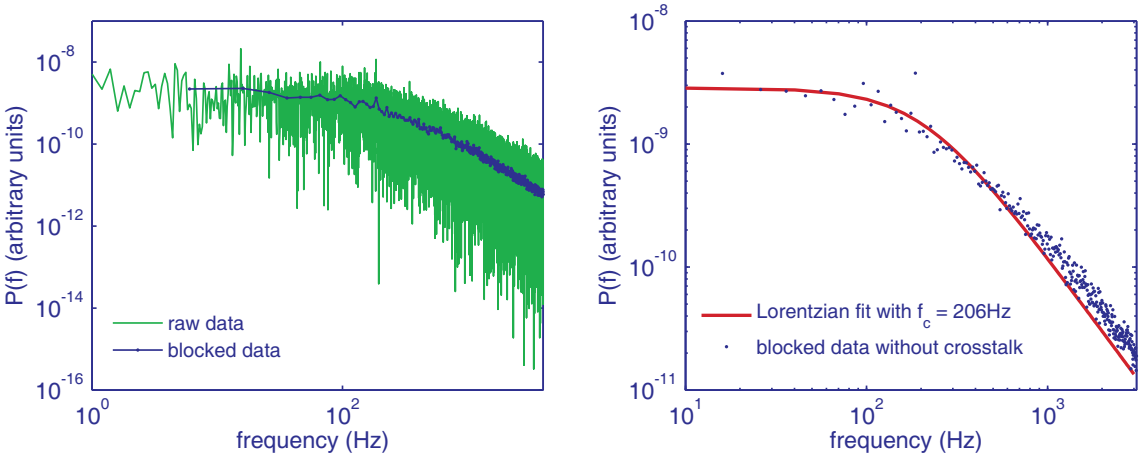

Figure 4.4: *Left* - We calculated the power spectrum from experimentally recorded positions of a trapped 100nm Au particle (see also Fig. 4.2 and 4.3). The blue dotted curve is the blocked power spectrum we use for further analysis. *Right* - We fitted a Lorentzian (Eq. (4.7)) to the blocked and crosstalk eliminated power spectrum. The corner frequency is determined by the fitting procedure.

mann distribution is defined by the absolute temperature T and the Boltzmann constant k_B. Plotting an inverted graph of the histogram in a log-lin fashion according to

$$U(x) = -k_B T \ln p(x) + k_B T \ln C, \tag{4.6}$$

gives the experimentally obtained potential U(x) of the optical trap as pictured in the right plot of Fig 4.3. The width of the distribution and thus the histogram depends on the temperature of the sample solution at the trap site and the trap stiffness κ_x (see also Eq. (4.9)).

We fit the harmonic potential $U(x) = \frac{1}{2}\kappa_x x^2$ (see Eq. (4.3)) to the experimentally obtained potential in Fig. 4.3 by varying the trap stiffness κ_x as fitting parameter [69]. This regression also provides us with an indication of the harmonicity of the trap.

4.2.2 Power spectrum and roll-off frequency

The power spectrum is the motion of the trapped particle translated from the time domain into the frequency domain. We Fourier transform our experimentally obtained position values and plot these over frequency as shown in Fig. 4.4. The acquired power spectral density is an exponentially distributed quantity. In order to be able to approximate this data with least-square fitting procedures to the theoretical model in Eq. (4.7), we apply a compressing technique called blocking. Here we average over a block of a certain number of data points and represent it as one single new data point. The so obtained blocked power spectrum is then Gaussian

distributed [55] and plotted in Fig. 4.4. Analysing the motion of the trapped particle in frequency domain enables us to determine the corner or roll-off frequency f_c. We need this quantity to calculate the trap stiffness later on.

The power spectrum of a particle trapped in a harmonic potential is theoretically described by a Lorentzian:

$$P(f) = \frac{P_0 f_c^2}{f_c^2 + f^2} = \frac{k_B T}{\pi^2 \gamma (f_c^2 + f^2)} \tag{4.7}$$

with the asymptotic power $P_0 = \frac{4\gamma k_B T}{\kappa^2}$. By fitting Eq. (4.7) to the experimentally obtained power spectrum we obtain the corner frequency f_c in terms of the drag coefficient $\gamma = 6\pi\eta r$ and the trap stiffness κ:

$$f_c = \frac{\kappa}{2\,\pi\,\gamma}. \tag{4.8}$$

Before fitting the Lorentzian to the power spectrum we eliminate any crosstalk from our data. Crosstalk between the x and y coordinates occurs due to the actual beam shape at the trap site or the electronic response of the quadrant photodiode. The trap itself should ideally be rotational symmetric. However, if the beam is slightly elliptical we have to align its major axes to the photodiode. Also the different quadrants may have varying sensitivity to the incident light and deliver an asymmetric output. Eliminating the crosstalk uncouples the x and y coordinate of the measured data. In Fig. 4.4 we fitted the Lorentzian from Eq. (4.7) to the blocked and crosstalk eliminated power spectrum of a 100nm trapped gold sphere by varying the corner frequency f_c and the asymptotic power P_0 as fitting parameter.

The described averaging and fitting procedure are the basis for our data analysis presented in Sec. 4.3. Some experimental factors have to be considered to acquire good data. It is important that the detection frequency exceeds the corner frequency to allow for exact measurements and reduce the risk of filtering errors such as aliasing. Although the Lorentzian is a low frequency approximation, it is well applicable for our experiments as the corner frequency f_c is much smaller than the Nyquist frequency $f_c \ll f_{Nyq}$ and we do not need to take high frequency contribution into account [55]. Additionally, the trapping potential of optical tweezers is only harmonic if the incident beam has a Gaussian beam profile and the displacement of the trapped particle from the centre is small. The mean-square displacement analysis as well as the corner frequency measurement rely on the equipartition theorem which predicts $1/2k_BT$ for harmonic potentials [69]. Analysing the trap with Boltzmann statistics gives a good check whether the actual potential in which the particle is held is harmonic.

4.2.3 Trap stiffness

We could use several variables to compare our analysed data. Ultimately, the corner frequency f_c being independent of any detector calibration gives a very precise and general means of characterising a trap. However, it is more common to compare the strength of the optical trap with the trap stiffness κ within the linear region of the trap. Here, the restoring force is linearly proportional to the displacement of the particle from the trap centre. There are various ways to determine κ experimentally. One method is to compare the trap force to another force such as Stokes friction force $F_{Stokes} = 3\pi d\eta v$ or the gravitational force. The former is obtained in an escape force measurement or simply by moving the sample or the particle at a certain velocity and measuring its displacement from the centre of the trap. We use a different method in our work, measuring the thermal fluctuations of the particle's position in the trap to determine the trap stiffness (see Sec. 4.2.1).

As described earlier, we obtain the trap stiffness κ by fitting a harmonic potential to the logarithmically displayed position values of the trapped particle. This is equivalent to employing the equipartition theorem ($\langle E_{pot}\rangle = \frac{1}{2}\kappa\langle x^2\rangle$) and gives κ in terms of the absolute temperature T:

$$\kappa = \frac{k_B T}{\langle x^2\rangle}. \tag{4.9}$$

This method requires a calibration of the detection system. The quadrant photodiode provides position values in volts which we have to convert in metres. We can either calibrate the quadrant photodiode independently as presented in Sec. 3.4.3. This is generally regarded as the most precise method [55, 69] if the trapping laser has a sufficient pointing stability and no other noise sources deteriorate the measurement. As discussed in Sec. 3.4.3 our system does not fulfil these requirements. Therefore we chose a different technique to calibrate our detection system. We are able to extract two independent values of the trap stiffness from our experimental data: one by applying the equipartition theorem (Eq. (4.9)), the other directly from the power spectrum. Knowing the viscosity of the buffer medium in which the nanoparticles are dispersed in, allows us to derive the trap stiffness from the corner frequency f_c of the power spectrum (Eq. (4.7)

$$\kappa = 2\pi\gamma f_c. \tag{4.10}$$

We calibrate the signal from the photodiode and convert a voltage into nanometers by comparing the values for κ found by these two methods (see Sec. 3.4.3). In addition we obtain the trap stiffness in the conventional form of pN/nm.

4.3 Results and discussion

In Chapter 3 we described our experimental setup. Our system is capable of trapping the particle, imaging the particle in the trap and measuring its position simulatenously. Being able to monitor the particles during trapping, both visually and electronically, proved extremely helpful as they are very small. They move position quickly due to their fast Brownian motion and are thus hard to find in the buffer solution. We can distinguish if there is more than one particle in the trap; even a preselection for size according to the colour of the particle's resonance is possible. This limits the spread of data to a certain extend as we are able to exclude particles that are not spherical or too large as these appear brighter and redder.

We conducted most experiments with a Fianium supercontinuum laser source, using a band of the infrared part of its spectrum (900-1100nm) to start with. This wavelength range is comparable to previous studies conducted on silver and gold nanoparticles using continuous wave (cw) lasers at 1064nm. The main difference of our setup is that the supercontinuum is a pulsed laser source, emitting picosecond pulses at 40MHz repetition rate. There are no comparative studies about pulsed trapping of metal nanoparticles versus cw trapping. Experiments trapping dielectric particles do not suggest any difference [75]. As we will see later on, our results with the pulsed source compare well to the cw trapping system of Oddershedde's group [13, 14]. However we observed some features indicating differences for optical trapping with pulsed lasers. One is the high frequency noise pictured in Fig. 4.5 and discussed later on. The other interesting observation is that we were not able to increase the trapping power beyond 50mW at the trap site as the metal nanoparticles would start to heavily oscillate or even disintegrate within seconds.

We trapped and characterised gold nanospheres with 80nm and 100nm in diameter as well as 80nm silver nanospheres. In addition, we varied the laser power in the trapping focus. The 100nm gold particles started to trap at 25mW up to 48mW. The 80nm gold and silver particles did not trap below 30mW. However, the gold particles would start to oscillate heavily and fall out of the trap after only 1-2s for powers above 50mW. The silver particles would even change colour and disintegrate at these power levels. Trapping powers of 50mW are too low to explain these observation with heating effects [22] alone. Even if we consider the slightly broader spectrum of the laser used and the associated water absorption, the heating effects should be similar to experiments where much higher power levels have been applied [13, 22]. There must be other mechanisms present, we believe these are likely to stem from induced nonlinearities [76] of the metal nanoparticle.

There are a couple of experimental factors that have to be mentioned. It is important that only one particle is present in the trap or near the trap site. Otherwise the histograms are distorted and an incorrect corner frequency is measured. Our imaging system was very advantageous at this point. It was possible to see straight away if an additional particle entered the trap site and we did not have to anal-

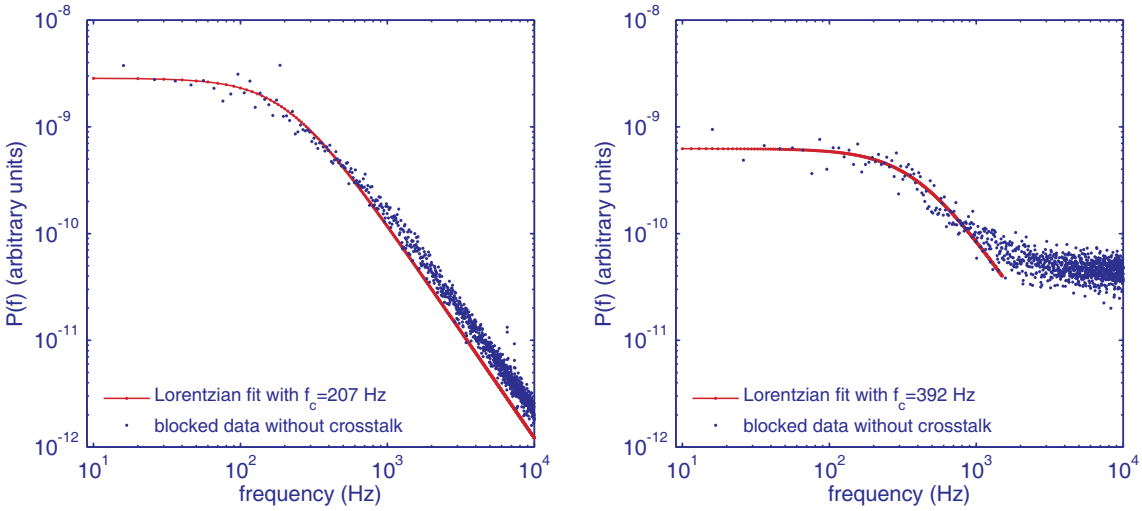

Figure 4.5: Comparing the recorded spectra for a trapped 100nm gold sphere (33mW) for a continuous wave laser source on the left and the pulsed supercontinuum source on the right shows significant differences in the high frequency region. The origin of this noise stems from the pulsed laser source. The Lorentzian is only fitted up to 1500Hz in the right plot as the large noise contributions prohibit high frequency fitting.

yse the data in order to see this. The laser focus and hence the actual trapping potential changes with propagation depth of the laser into the sample because of aberration. In order to be able to compare the acquired data we trapped the particles at the same sample depth. Positioning the trap about 10μm deep in the sample chamber, we avoided any interference with the glass coverslip and having to include hydrodynamic corrections for our data analysis (see Sec. 3.4.3).

Measuring the motion of the particle in the trap is very challenging for this nanometre size scale. The quadrant photodiode detects the far-field interference of the incident trapping laser and the scattered light of the trapped particle. The latter is accordingly small as it depends on the size of the nanoparticle. The intensity of the relevant part of the light field impinging on our photodiode is thus only a fraction compared to the unperturbed incident laser. The main challenge for all data acquisition has been to achieve a good signal to noise ratio. The smaller the particles, the harder it was to obtain satisfying data. Already the tiny increase in size between 80nm and 100nm made a large difference as we show in Fig. 4.6-4.7.

Additionally, an unexpected feature in the power spectrum of the supercontinuum showed up. At high frequencies (>1000Hz) the power spectra did not follow the expected decline. We did test measurements with a cw 1064nm laser and are therefore able to compare the spectra of the cw trap and the pulsed (supercontinuum) trap in Fig. 4.5. The setup we used for trapping and data acquisition was entirely identical, only the laser differed. We see the expected decline at high frequencies in the power spectra of the cw trap. Contrary, the spectra of the supercontinuum never showed

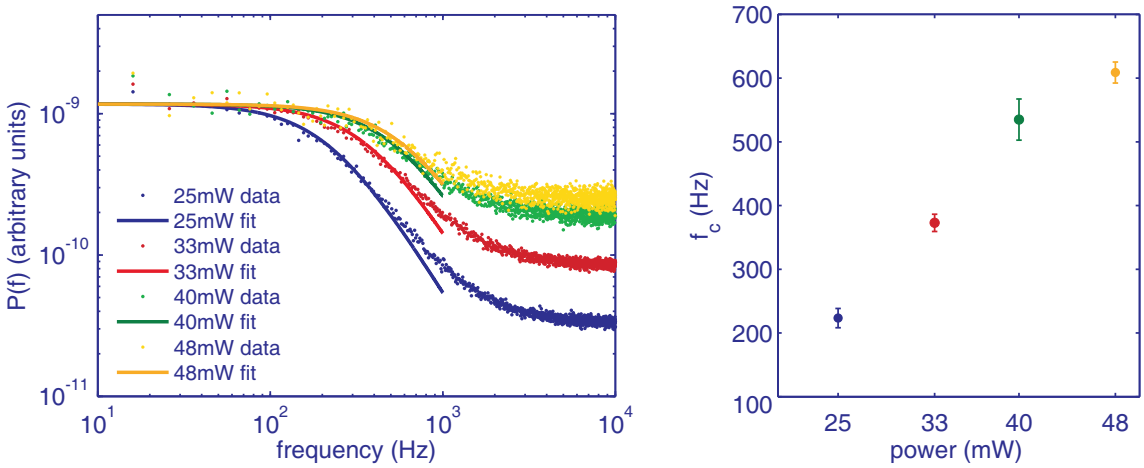

Figure 4.6: The corner frequency f_c and the trap stiffness κ increase linearly with power. Here, we trapped 100nm gold spheres at various power levels and recorded the data for 5s at 50kHz. *Left* - The power spectra are averaged over 5-20 data sets. After blocking and eliminating the crosstalk of the data we fitted a Lorentzian between 10-1000Hz to the spectra as described in earlier sections. *Right* - The resulting corner frequencies are plotted with respect to power. The error bars indicate a 95% confidence interval.

this characteristic decline and always ended up with a "high tail" as pictured on the right hand side of Fig. 4.5. We believe this effect originates from the pulsed laser source and not from electronic noise in the quadrant photodiode or any other noise source in the setup. However, to this point, we cannot say for certain what causes this large high frequency contribution. A beam pointing stability problem would appear in the low frequency region of the spectrum. Improving the signal to noise ratio could help circumventing this problem. For future experiments we suggest to filter out the unperturbed component of the trapping laser.

In our first study we investigated the power dependence of the corner frequency f_c. The previous section explained how to calculate the trap stiffness κ from f_c. We trapped a 100nm gold particle at 25mW, 33mW, 40mW and 48mW. The resulting power spectra and corner frequency along one axis of the trap are shown in Fig. 4.6. Increasing the power at the trap site increased the intensity of the trapping beam and the gradient force holding the particle. We averaged over 5-20 data sets recorded for 5s each at 50kHz.

We applied a least square fitting algorithm to fit the Lorentzian (see Eq. (4.7)) to the blocked and crosstalk removed power spectra. As we acquired data for a rather long time sequence (5s) we were able to average our data in blocks of 10 and even obtained a good representation of the trapping behaviour at low frequencies. This is important as the low frequency part does influence the position of the corner frequency significantly. Because of the large high frequency contribution to the power spectrum we only fitted the Lorentzian up to 1kHz. All data analysis was performed

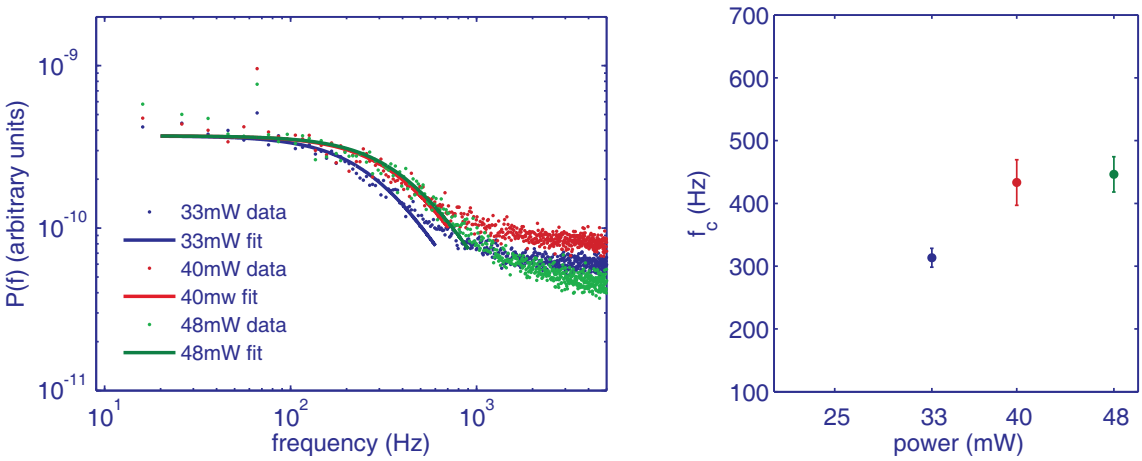

Figure 4.7: We trapped 80nm gold spheres at 33mW, 40mW and 48mW. *Left* - The power spectra are averaged over 5-8 data sets. After blocking and eliminating the crosstalk of the data we fitted a Lorentzian between 20-800Hz to the spectra as described in earlier sections. *Right* - The resulting corner frequencies are plotted with respect to power. The error bars indicate a 95% confidence interval.

with our own MATLAB programme. The corner frequency provided the quantity to calculate the trap stiffness according to Eq. (4.10). We kept the temperature T constant at $T = 22°$ for all experiments. The viscosity of water at $T = 22°$ is $\eta = 9.5 * 10^{-4}$Pa s. Heating effects are negligible at these low powers [22]. We refer the reader to Sec. 3.4.3 for a detailed discussion about viscosity. Figure 4.9 displays a summary of the so calculated trap stiffness for varying power levels and particles.

The increase in f_c with power became similarly evident for 80nm gold and silver particles, although the difference between the various power levels was not as significant as for 100nm gold spheres. We were not able to trap 80nm particles below 30mW. This indicates that we required more power to trap smaller particles, an expected result observed in earlier experiments [13, 17]. The results for 80nm gold and 80nm silver spheres are plotted in Fig. 4.7 and Fig. 4.8 respectively. Again we averaged over 7-14 data sets recorded for 5 s each at 50kHz and fitted a Lorentzian between 20Hz and 500-800Hz according to the spectra. We present the calculated trap stiffness values in Fig. 4.9 for all sphere sizes and power levels.

We were able to reproduce the size dependence of the trap stiffness as suggested in [13] for gold spheres. The trap stiffness increased for the 100nm gold spheres compared to the 80nm gold spheres for all measured power levels and is presented in Fig. 4.9. Overall there was no significant difference in trap stiffness between 80nm gold and silver spheres. At this trapping wavelength far from resonance the result is not surprising as the material parameters ($\varepsilon_{\text{gold}} = -51.5 + i3.4, \varepsilon_{\text{silver}} = -51.9 + i3.4$) and consequently refractive indices ($n_{\text{gold}} = 0.24 + i7.22, n_{\text{silver}} = 0.23 + i7.21$), polarisabilities($\alpha_{\text{gold}} = 9.5 \times 10^{-22} + i2.9 \times 10^{-23}\text{m}^3, \alpha_{\text{silver}} = 9.3 \times 10^{-22} + i1.9 \times$

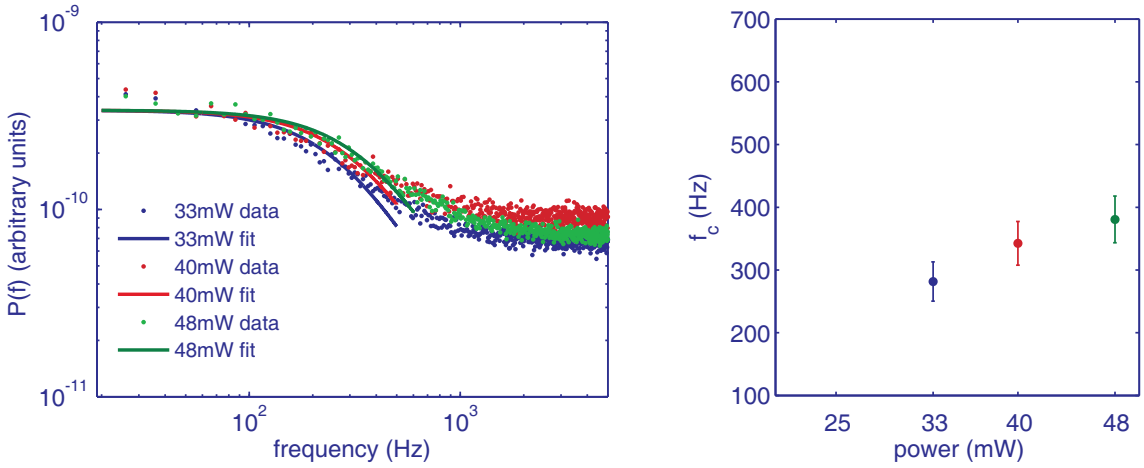

Figure 4.8: We trapped 80nm silver spheres at 33mW, 40mW and 48mW. *Left* - The power spectra are averaged over 7-14 data sets. After blocking and eliminating the crosstalk of the data we fitted a Lorentzian between 20-600Hz to the spectra as described in earlier sections. *Right* - The resulting corner frequencies are plotted with respect to power. The error bars indicate a 95% confidence interval.

$10^{-23}\mathrm{m}^3$) and scattering cross sections($\mathrm{C}_{\mathrm{scat-gold}} = 1.92 \times 10^{-16}\mathrm{m}^2, \mathrm{C}_{\mathrm{scat-silver}} = 1.85 \times 10^{-16}\mathrm{m}^2$) of both materials are almost identical. The forces affecting the particles in the trap are therefore comparable for gold and silver particles in the infrared.

As far as we aware, there is no study investigating the effect of trapping metal nanoparticles with a pulsed laser compared to a cw laser. Pulsed tweezing has been investigated for nonlinear lithium niobate (LiNbO32) crystals [77]. The high peak power of the pulsed trapping beam is exploited for maximal efficiency of the second harmonic generation. Using pulsed lasers is more advantageous than high power cw lasers as the average power at the trap site and therefore heating effects remain low [77]. Furthermore the high peak power enables trapping of very small nanoparticles such as quantum dots [78] that would need much higher average powers to be trapped with a cw laser. This might explain our low trapping powers compared to previous metal nanoparticle trapping experiments [13, 14]. There have been theoretical investigations suggesting that a too short pulsed laser may destabilise the trapping [79]. However, our supercontinuum source has a pulse duration of 10ps and which is according to [79] long enough to allow stable trapping. The only experimental study comparing pulsed versus cw trapping investigated 1.28μm silica spheres and found no difference in trap stiffness between the two laser sources [75].

Comparing our results obtained with a pulsed laser source to previous studies we believe that the achievable trap stiffness is the same as using a cw source. We do however see differences in the power spectrum and high power behaviour of the trapped particles. This could be due to nonlinear effects caused by the field

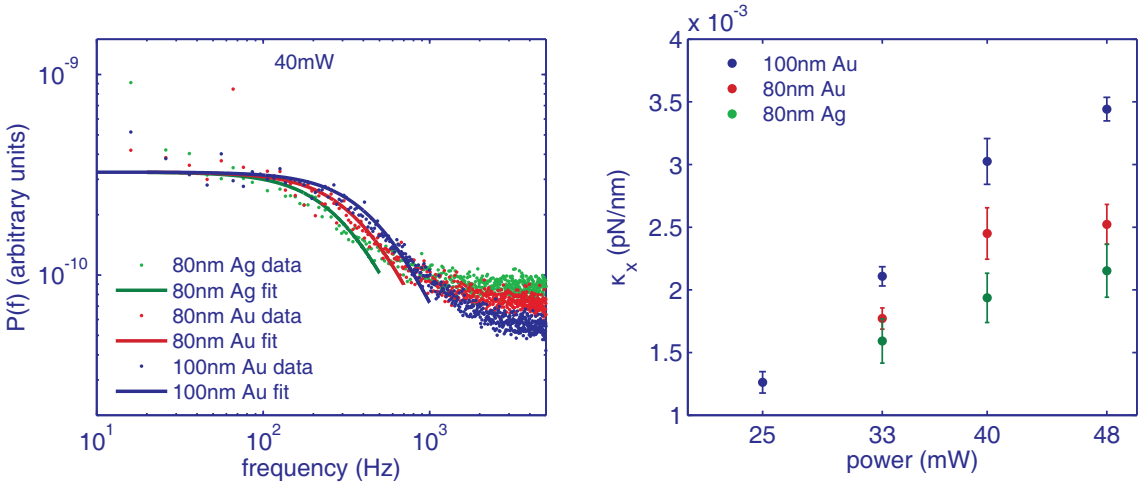

Figure 4.9: *Left* - We selected the power spectra of 100nm gold, 80nm gold and silver particles trapped at 40mW to show the differences in trapping at carying particle size and material. The larger 100nm spheres have a higher corner frequency f_c than the 80nm spheres, resulting in a larger trap stiffness. *Right* - This is a summarising plot comparing trap stiffness values calculated from the experimentally obtained corner frequencies f_c of all experiments described in this section. Each data point represents the average of 5-20 data sets recorded for 5s each at 50kHz. The error bars indicate a 95% confidence interval.

enhancements close to metal nanoparticles. These effects should increase closer to the plasmon resonance of the particles. Nevertheless, far from the plasmon resonance the trap stiffness this does not seem to be affected by the pulsed laser source.

4.4 Wavelength dependence of the trap stiffness

The forces acting on a trapped particle in a laser beam depend on several parameters such as the beam profile and power of the laser, size of the particle and the material parameters of the particle itself and the surrounding medium. We demonstrated in Chapter 2 that the material parameters of metal nanoparticles vary strongly with wavelength. Consequently the force exerted on such a particle in the trap changes for different wavelengths. According to this wavelength dependence, trapping metal nanoparticles may be seen in analogy to trapping atoms where the atomic resonance is crucial to achieve trapping. The essential gradient force is only strong enough to hold the atoms with a trapping laser wavelength slightly above the atomic resonance. This red-detuning of the trapping laser exploits the manifold enlarged polarisability of the atom at resonance while minimising scattering by slightly detuning the laser above resonance. Although metal nanoparticles are much larger than atoms, this concept still applies in principle, not only for red-detuning but also for blue-detuning as we demonstrate in Chapter 5.

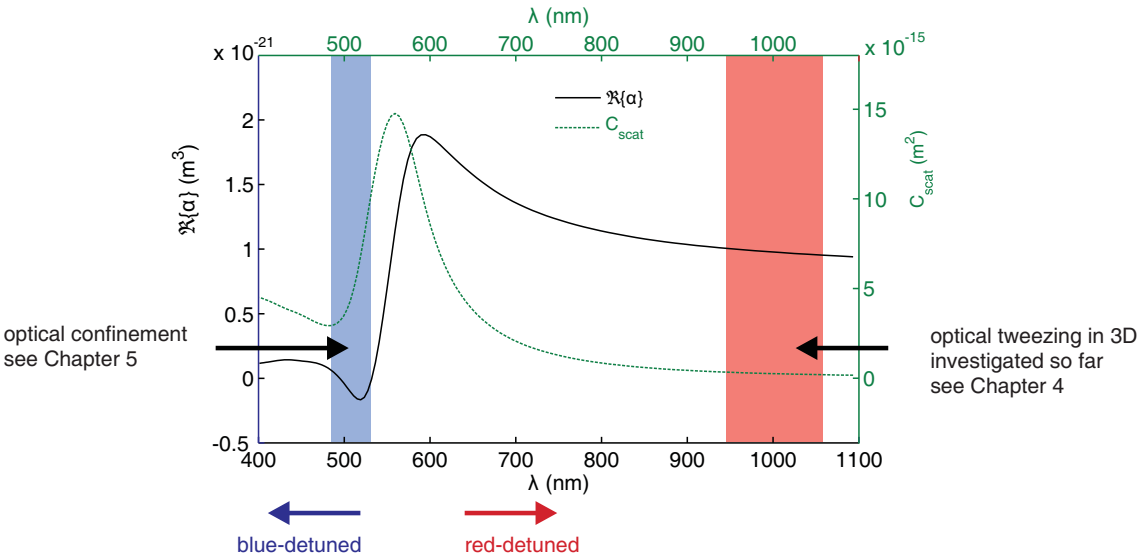

Figure 4.10: This graph illustrates the wavelenth dependence of the polarisability α (left axis) and scattering cross section C_{scat} (right axis) of a 80nm gold sphere. This wavelength dependence consequently appears in the trapping force, as it is the result of a fine balance between scattering and gradient force components. We marked the wavelength regions investigated so far. The wavelength region above the resonance is commonly referred to as red-detuned, below as blue-detuned. Experiments characterising trapping of metal nanoparticles on the red-detuned side close to resonance are still lacking to date.

The key idea of the experiment presented in this chapter is to quantify the wavelength dependence of the trapping force for metal nanoparticles. We started by analysing the optical trap with an infrared trapping laser. This has been done before and provides a solid starting point for our study. We aimed to subsequently lower the wavelength of the trapping laser, approaching the particle plasmon resonance of the gold and silver nanoparticles from the long-wavelength side (red-detuned). Following the theoretical discussion in Chapter 2, we anticipate an increase in scattering and absorption close to resonance. This alone would destabilise the trap and render tweezing impossible. However, we also found that the polarisability α and thus the attractive gradient force increases significantly at resonance, possibly balancing the increased scattering force. For clarity we illustrate these points once again in Fig. 4.10, plotting the scattering cross section and polarisability for a 80nm gold sphere. We marked the wavelength regions that have been investigated so far.

For this experiment to work it is crucial to keep other parameters influencing the trap stiffness as constant as possible. Using the same buffer solution and nanoparticles as before is evident. The challenging aspect of this experiment is to find a laser source providing wavelengths from the infrared (1100nm) down to the resonance of the nanoparticles around 500nm by keeping the same beam profile. We decided to use the supercontinuum source to minimise the variation in beam profile across

the wavelengths. The alternative approach, conducting the experiment with various different laser sources, seemed to pose an issue with respect to a constant beam profile.

Unfortunately the beam profile of our supercontinuum source is not constant over its spectrum. We found out that it is not even Gaussian in the visible spectrum as we discuss in the following section. This rendered optical trapping of metal nanoparticles at visible wavelengths impossible. We managed to trap 1μm silica spheres, but the requirements on the z-gradient of the beam in the focus of the trap are more stringent for smaller particles. With our current supercontinuum source we only achieved guiding along the beam axis and 2D trapping against the sample cover glass. For a quantitative analysis of the trap stiffness we require a Gaussian beam profile. The theory of modelling optical tweezers with a Hookean spring and retaining a trap stiffness as discussed earlier relies on the fact that the optical potential in the trap is harmonic to exert a linear displacement force on the trapped particle. Even if we would have been able to trap metal nanoparticles with a non-Gaussian beam profile, the analysis and comparison of the trap stiffness would have been rather cumbersome.

4.4.1 Supercontinuum beam profile

After characterising the optical trap for metal nanoparticles in the infrared band (900-1100nm) of the Fianium supercontinuum source, we started to select other wavelength bands of the laser spectrum. However we were not able to achieve stable trapping of metal nanoparticles in 3 dimensions for any of the selected bands in the visible. We analysed the output of the supercontinuum and recorded the beam profiles pictured in Fig. 4.11. In the infrared (900nm-1100nm) the output profile is Gaussian as expected. All other bands are 40nm wide and centred around the wavelength displayed in the top left corner of each beam profile. The output beam in the visible is doughnut-shaped with very low intensities in the centre of the beam. This region is most crucial for optical trapping and it is not surprising we were not able to trap any metal nanoparticles. In Fig. 4.12-4.14 we fit a Gaussian curve to the acquired beam profiles and show a sketch of our measurement setup.

In order to improve the available laser beam profile we investigated two methods of spatial filtering. In the first instance we focussed the visible part (400nm-750nm) of the beam with a 50mm lens and inserted a 100μm pinhole in the focal plane. A second lens, a focal length away, reformed the collimated beam. The result of this approach is pictured in Fig. 4.13. Although we did improve the beam quality, the output is still not Gaussian and it was not possible to trap metal nanoparticles. The flat top in the beam centre prevents the formation of a potential steep enough in the focus to hold metal nanoparticles.

In our second experiment we passed the visible part (400nm-750nm) of the beam through a photonic crystal fibre (Crystal Fibre, LMA-10 PCF, 10μm core diameter)

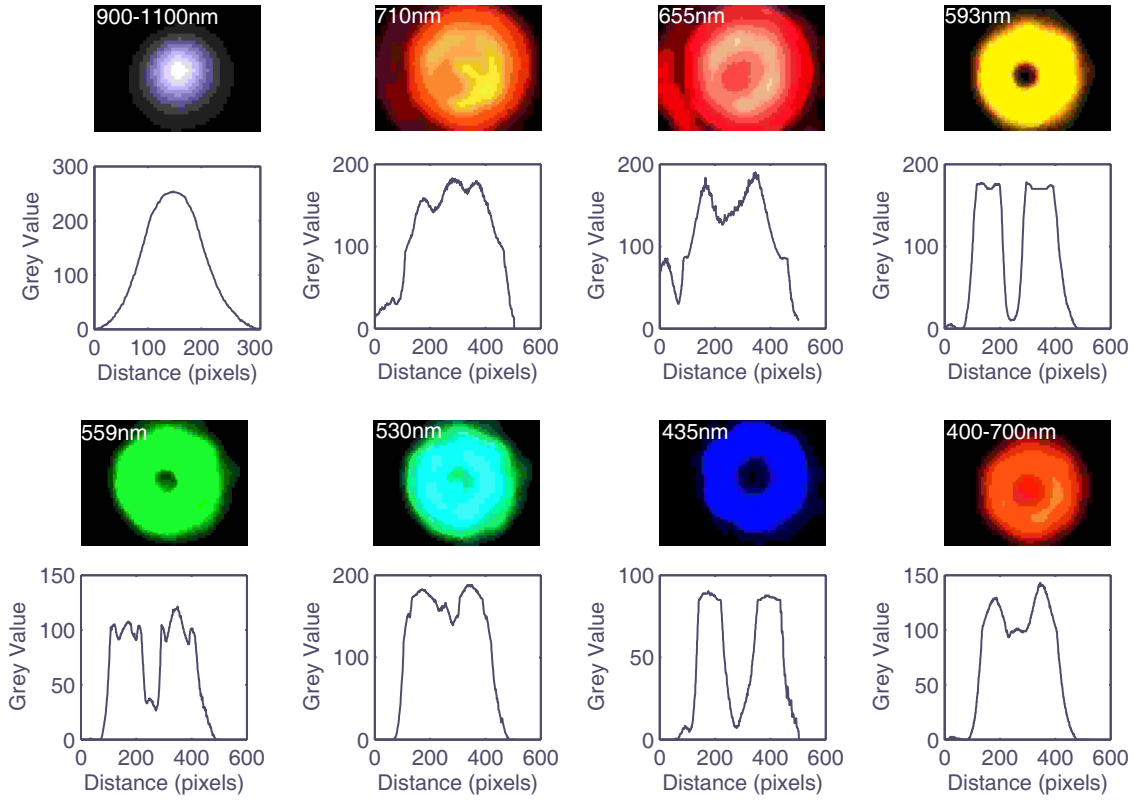

Figure 4.11: We recorded the beam profiles for various bands of the supercontinuum spectrum with a digital colour CCD camera. By inserting Semrock filters into the beam path we selected 40nm wide bands centred around the displayed wavelength. The graphs below the colour images display the intensity cross section of the beam. The bottom right profile shows the entire visible spectrum without inserting filtering optics in the beam path. The doughnut-shaped beam profile is present throughout the visible spectrum.

to clean up the beam profile. The fibre we used was optimised for the visible part of the spectrum. We achieved 50% efficiency in transmission through the fibre and both coupling objectives (Newport 10x), indicating very good coupling of the beam into the fibre. The outcome is pictured in Fig. 4.14. Again, the profile is not Gaussian and trapping could not be achieved for metal nanoparticles.

Overall we suggest either using a different laser source for this experiment or trying yet another method of spatial filtering. For example one could pass the supercontinuum through single mode fibres instead of bandwidth filters to select the desired wavelength band and clean up the mode profile. The fibre would need the appropriate core size for each desired wavelength band. Depending on the power output after the fibre and the bandwidth of the remaining beam this should provide a feasible option for future experiments.

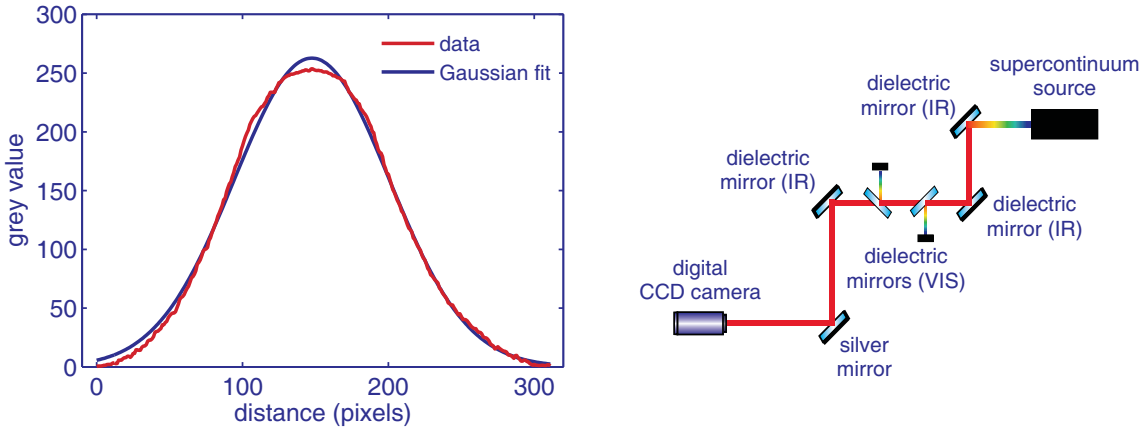

Figure 4.12: *Left* - We fit a Gaussian curve to the intensity cross section of the recorded beam profile (900-100nm). This demonstrates that the infrared band (900-100nm) of the supercontinuum spectrum has a Gaussian beam profile, ideal for optical trapping. *Right* - The sketch of the setup shows how we separated the infrared band from the supercontinuum spectrum. We used a combination of Thorlabs dielectric mirrors (EO3, 750-1100nm reflective) and Comar dielectric mirrors (400-900nm reflective) to filter out the visible parts of the spectrum.

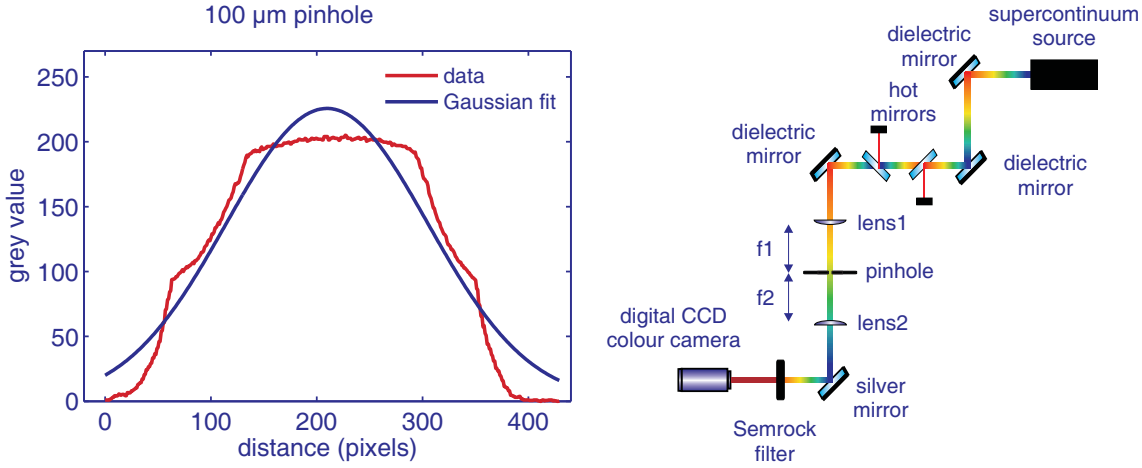

Figure 4.13: *Left* - The intensity cross section of the beam profile after passing through a 100μm pinhole resembles more a top-head function than a Gaussian. *Right* - We show a sketch of the setup separating the visible band from the supercontinuum spectrum and passing a spatial filter. The latter is formed by two 50mm lenses and a 100μm wide pinhole. We used a combination of Thorlabs dielectric mirrors (EO2, 400-750nm reflective) and hot mirrors (750-1200nm reflective) to filter out the infrared parts of the spectrum. Finally we pass the beam through a Semrock filter resulting in a beam with 40nm bandwidth centred around 710nm.

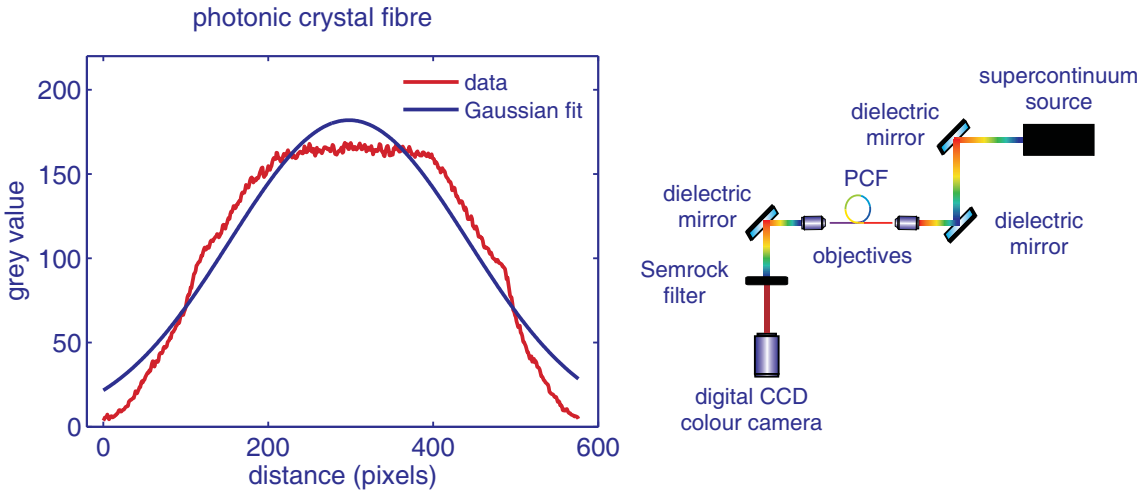

Figure 4.14: *Left* - The intensity cross section of the beam profile after passing through a photonic crystal fibre (Crystal Fibre, LMA-10 PCF, 10μm core diameter) is slightly better than the one achieved after a pinhole (see Fig. 4.13). However trapping was still not possible indicating that the beam profile is not Gaussian enough. *Right* - We show a sketch of the setup separating the visible band from the supercontinuum spectrum and passing the photonic crystal fibre. We used Thorlabs dielectric mirrors (EO2, 400-750nm reflective) to filter out the remaining infrared parts of the spectrum. Finally we pass the beam through a Semrock filter resulting in a beam with 40nm bandwidth centred around 710nm.

4.5 Conclusions

We started this chapter reviewing the data analysis techniques for the quadrant photodiode voltage outputs. We concentrated on the equipartition theorem and the power spectrum analysis. These two methods helped us to determine the trap stiffness κ and hence provided us with a means to quantitatively compare the trap stiffness of various systems.

We analysed optical trapping of 80nm gold and silver spheres as well as 100nm gold spheres at 4 different power levels. Contrary to previous experiments, we used a pulsed laser source to trap metal nanoparticles for the first time. The larger particles (100nm gold) had an increased trap stiffness compared to the smaller particles (80nm gold). Further we found that higher power levels at the trap site led to larger trap stiffness values. There was no significant distinction in the trapping behaviour comparing 80nm gold and silver spheres. These results confirm our expectations and compare well with previous experiments [13, 14].

We found out that trapping with a pulsed laser does not seem to affect the trap stiffness compared to a cw laser source within the investigated wavelength range (900-1100nm). However we observed new effects that require further investigation in the future. First, a high frequency contribution to the power spectrum of our

pulsed laser trap appeared. Second, the trapping power could not be increased to values reported elsewhere [13, 22] as the particles in the trap would oscillate heavily and could not be held longer than a few seconds.

Finally we discovered that the beam profile of our supercontinuum source varied significantly over its spectral range. We investigated in two different techniques to spatially filter the mode and achieve a Gaussian profile. With the improved beam profiles we were able to achieve optical trapping of micron sized beads. But optical trapping of metal nanoparticles imposes more stringent conditions on the beam profile than trapping micron sized dielectric objects. In the end, the beam profile of our laser source was not good enough to achieve stable 3 dimensional trapping of metal nanoparticles. The experimental investigation of the wavelength dependent trap stiffness remains to be explored.

5 Optical trapping below resonance

In this chapter we investigate the interplay of forces acting upon gold nanoparticles when exposed to laser light close to their plasmonic resonance. Choosing a wavelength below resonance, the particle is no longer attracted by the high intensity region of the trapping laser. In contrary, metal nanoparticles are repelled by laser light shorter than their resonance wavelength. We present the results of this experiment conducted with 100nm gold spheres in the following.

The effect is explained qualitatively with the dipolar model also employed for atom trapping. An atom has a negative polarisability α below its resonance. This renders the gradient force F_{grad} repulsive and results in repelling the atom from high intensity laser regions. Although 100nm gold nanoparticles do not have discrete energy states and are much larger than atomic dipoles, we observed the described effect similar to blue-detuned atom trapping. We discussed in Chapter 2 that the quantitative analyse is more cumbersome as the metal nanoparticles are too large for a dipolar description. We show in Sec 5.3 of this chapter how this may lead to ambiguous interpretation of the models.

Blue-detuned trapping of metal nanoparticles requires a different trapping geometry than the optical tweezers discussed so far. We used a doughnut-shaped Laguerre-Gaussian (LG) beam profile, exhibiting a dark centre with no intensity surrounded by a ring of laser light, to trap the metal nanoparticle in our experiment. This trapping geometry exploits the plasmonic resonance by using the repulsive gradient force F_{grad} to hold the particle [16]. The scattering force F_{scat} also increases close to resonance and underpins the repulsion of the particles even more. Trapping particles in a dark region opens up new avenues for optical manipulation of metal nanoparticles beyond the single beam tweezers and presents a possibility to avoid potential heating [22] by holding the nanoparticles away from the high intensity region of the trapping laser.

After a brief introduction to Laguerre-Gaussian beams in Sec. 5.1.1, we proceed presenting our experiment in detail in Sec. 5.1.2. Furthermore, the Laguerre-Gaussian beam exhibits orbital angular momentum (OAM). We demonstrate the transfer of OAM from the LG beam on to the metal nanoparticles in Sec. 5.2. Finally, we conclude this chapter with a critical discussion about the dipolar model and its validity in our experiment (Sec. 5.3).

5.1 Optical vortex trap for resonant confinement

Standard optical tweezers are not always the right choice to trap metal nanoparticles. Close to the plasmon resonance of metal nanoparticles, their interaction with laser light changes significantly. Instead of being attracted by a high intensity focus, they are repelled by the laser (see Chapter 2). Therefore we considered an alternative trapping geometry for our blue-detuned trapping experiments, confining metal nanoparticles to a dark region surrounded by high intensity laser light. We employed optical beamshaping to create a ring of light encircling the gold nanosphere. A single-ringed Laguerre-Gaussian (LG) beam generates an annular trapping laser profile (zero intensity in the core). Once loaded into the trap site the particles are surrounded by the high intensity region of the beam and trapped in the dark core. This trapping geometry is commonly used in atom trapping and relies on the repulsive nature of the trapping laser [16]. The repulsion originates from a negative gradient force or a strong scattering force component. Both processes occur at the blue-detuned side of the resonance of metal nanoparticles.

An advantage of confinement compared to tweezing is that particles remain in the dark region hence experiencing less scattering events, avoiding strong absorption and heating. Our LG trap enabled us to manipulate 100nm gold spheres at three different wavelengths below their resonance frequency. We recorded their spatial position in the trap and analysed their confinement with standard video detection. The size of the trap site depends on the applied wavelength and power of the LG beam.

5.1.1 Laguerre-Gaussian beams

The beam profile of a Laguerre-Gaussian beam is commonly referred to as doughnut-shaped beam. A ring of high laser intensity surrounds a dark centre with no intensity. In addition to the unusual spatial intensity distribution, an LG beam also possesses an intriguing phase structure. At the centre all phases are present and this phase singularity causes the doughnut-shaped intensity profile. Figure 5.1 shows pictures and an intensity profile taken from LG beams in our experiment.

Laguerre-Gaussian modes are structurally stable solutions of the paraxial wave equation and form a complete set of eigenfunctions. They are higher order transverse electromagnetic modes and possess a circular symmetry. A certain mode is defined by its radial mode index p, indicating the number of nodes across the radial field distribution and the azimuthal phase index ℓ, determining the phase structure of the beam. The azimuthal phase index ℓ gives the number of 2π cycles in azimuthal direction around the circumference of the beam and is sometimes called the helicity or charge of the beam [80]. The amplitude of the electric field of a weakly focussed LG beam in cylindrical coordinates is given by [81]

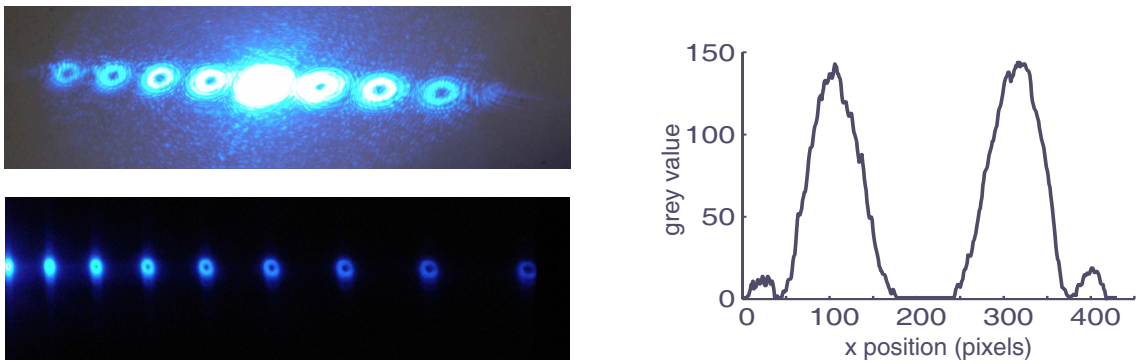

Figure 5.1: *Left* - These two photographs from our experiment depict typical cross sections of LG beams. The top picture shows the diffraction pattern of a hologram illuminated with an Argon Ion laser (Spectra-Physics 2040E). The central beam is the zeroth order with a topological charge $\ell = 0$ (Gaussian beam). To its left and right we see higher order LG beams, starting with $\ell = 2$, $\ell = 4$ and so on. The dark core increases in size for larger topological charge ℓ. The bottom picture shows LG beams created with the same hologram but with a 405nm diode laser. The zeroth order ($\ell = 0$ - Gaussian beam) is towards the left, outside of the picture. *Right* - We plot the intensity profile of the cross section of a typical LG beam used in our experiments. The side lobes stem from the impurity of the LG mode created with our hologram. These also appear in the upper left photograph of the cross section of the LG beam.

$$E_p^\ell(r,\phi,z) \propto e^{-i\ell\phi}\,(-1)^p\,L_p^\ell\Big[\frac{2r^2}{\omega_0^2}\Big]\,\Big(\frac{r\sqrt{2}}{\omega_0}\Big)^\ell\,e^{-i\Psi(1+2p+\ell)}\;\;e^{-\frac{r^2}{\omega^2}}\;e^{-\frac{ikr^2}{2R(z)}}. \tag{5.1}$$

The distance from the centre beam axis is denoted with r, ϕ is the azimuthal angle, z the distance from the beam waist ω_0 with the focus at $z = 0$, k is the wave number ($k = 2\pi/\lambda$), $\omega(z)$ is the radius at which the field amplitude drops to $1/e$ of its on-axis value with its minimum value $\omega_0 = \omega(z{=}0)$ and $R(z)$ is the radius of curvature of the wavefronts comprising the beam ($R(z){=}z + [1 + (z_R/z)^2]$ with the Rayleigh range $z_R = \pi\omega_0^2/\lambda$). Ψ is the Gouy phase of the beam. L_p^ℓ are the generalised Laguerre polynomials with indices ℓ and p.

The amplitude is composed of the standard Gaussian part (the two final terms) and additional contributions characteristic for the LG beam. The distinct phase structure of an LG beam leads to a phase singularity on the beam axis (vortex) with zero light intensity. Due to their helical wavefronts, the Poynting vector has an azimuthal component. The term $e^{-i\ell\phi}$ shows the azimuthal angular dependence of the amplitude and results in an orbital angular momentum of $\ell\hbar$ per photon (see Fig. 5.2).

The main advantage of using an LG beam is the absolute darkness at its centre. We tested an alternative method to create a doughnut-shaped amplitude profile

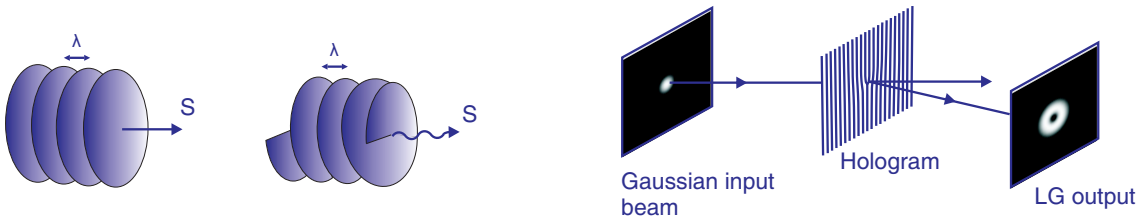

Figure 5.2: *Left* - This diagram illustrates the different wavefronts for Gaussian and LG beams in a schematic manner. Because of their helical wavefronts, LG beams possess orbital angular momentum (OAM). In addition to components in the direction of beam propagation, the Poynting vector has azimuthal components leading to the typical phase structure of the LG beam. *Right* - A stationary hologram acts as diffraction pattern and produces LG beams of different helicities ℓ from an incident Gaussian beam. The zeroth order after the hologram remains the basic Gaussian beam, whereas the higher orders are LG beams with increasing helicity ℓ.

by imaging a circular beam block at the centre of the beam into the trap site. However this does not create complete darkness. There always remains a bright spot of light along the beam axis due to diffraction [82] which is known as Arago's spot or Poisson's bright spot. The doughnut-shaped amplitude profile was the most important criteria for our experiment. In addition to this property the LG beam possesses orbital angular momentum (OAM) due to its phase structure. This feature adds interesting side effects to our experiment which we discuss in more detail in Sec. 5.2.

5.1.2 Laguerre-Gaussian trap

Compared to optical tweezers, the setup for the Laguerre-Gaussian trap requires only few changes; primarily the trapping beam. Choosing the appropriate laser wavelength with respect to the particle plasmon resonance is crucial for resonant optical trapping as we discussed in Sec 2.2. The output mode of a standard laser is commonly Gaussian and is converted to a LG mode with diffractive optics.

We generated the Laguerre-Gaussian beam with a fixed phase hologram ($\ell = 2$, p=0, 24% efficiency) placed in the laser beam path of the fundamental Gaussian (TEM_{00}) output of our Argon laser. The hologram is essentially a diffraction grating with a fork-like singularity at its centre. This is the interference pattern of a fundamental Gaussian mode and an LG beam and hence forms our hologram as we illustrate in Fig. 5.2. It transmits the fundamental Gaussian mode in the zeroth order, and Laguerre-Gaussian modes with increasing mode indices $n \times \ell$ in higher orders n. We used the first diffraction order ($\ell = 2$) of three Argon Ion laser lines (488nm, 514nm, 528nm) for our studies. The size of the dark region at the beam centre depends upon the topological charge ℓ [83] and wavelength λ of the laser. By using different sizes of LG beams (different topological charge ℓ or different wave-

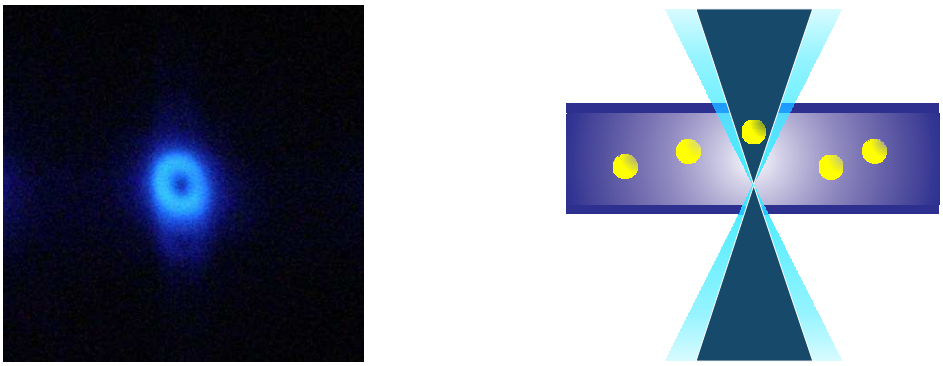

Figure 5.3: *Left* - The photograph of a Laguerre-Gaussian (LG) beam profile (p=0, $\ell = 10$) taken transverse to its propagation axis, clearly shows the dark core. *Right* - This side view sketch of our ringtrap illustrates the trapping of gold nanoparticles inside the dark core of the LG laser beam. The gold nanoparticle is trapped by the LG beam in x and y direction. The laser focus and the top coverslip of the sample chamber confine the nanoparticle in z direction.

lengths λ), we are able to control the area of confinement and the amount of particles taking up at once inside the trap.

The generated LG beam passes a magnifying telescope and subsequently enters a custom-built inverted microscope setup focusing the beam into the sample chamber with a microscope objective (Nikon Plan, 50x oil, NA 0.9) as we show in Fig 5.4. We used a single-ringed LG mode ($p = 0$) with $\ell = 2$ at laser powers varying from 40 to 110mW at the objective back aperture. Two microscope coverslips form the thin (7-10 microns deep) sample chamber containing the 100nm gold particles (see Fig 5.3). There is no need to focus the LG beam as tightly as for single beam tweezers because the particle is trapped in a region surrounded by light instead of tweezed in a high intensity laser focus. We thus created a cone of light along the propagation direction of the laser. The trapped gold sphere is confined within the dark core of LG beam. Its motion in the x-y direction is restricted to a region of a radius from 0.9 μm to 1.4 μm according to the applied wavelength. The sphere's upward (axial) motion is constrained by the top glass coverslip. Below the trapping position, the LG beam is focussed tightly enough that the particle cannot fall through the focus and gets repelled upwards in direction of the beam propagation.

We illuminated the sample with brightfield Köhler illumination and recorded the particle motion in transmission with a CCD camera (Watec, WAT250D) at a speed of 25 frames per second. Köhler illumination was essential to be able to see the nanoparticles as their size is below the diffraction limit. However, we were still limited to particles larger than 100nm. Smaller metal nanoparticles are almost invisible in brightfield transmission microscopy as they do not create enough contrast. More details about our imaging systems are discussed in Sec 3.3.

We achieved trapping of the 100nm gold nanoparticles for three different wave-

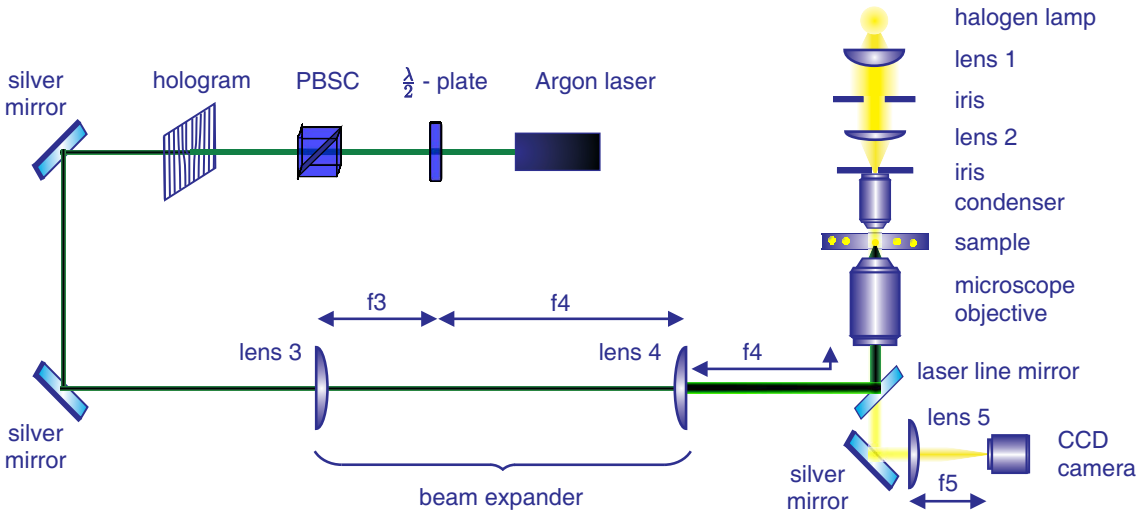

Figure 5.4: This diagram illustrates the setup for the Laguerre-Gaussian (LG) trap including the laser beam path as well as the illumination part of the system. We use antireflection coated lenses (visible 450-900nm) throughout the setup. After a half-wave plate and a polarising beam splitter cube (PBSC), the beam passes the hologram ($\ell = 2$, p=0). We take the first diffraction order and expand the LG beam to fill the back aperture of our microscope objective (Nikon Plan, 50x oil, NA 0.9). We describe the illumination path further in Sec. 3.3.

lengths (488nm, 514nm, 528nm) from an Argon Ion laser (Spectra-Physics 2040E). All wavelengths are situated on the blue-detuned side of the gold nanoparticle's resonance. Additionally, we observed that the particle residence time in the dark core of the LG beam increased as we moved to higher laser powers. The closer we chose a laser wavelength to the plasmon resonance of the nanoparticle, the less laser power we needed to hold the particles in the LG trap. At 528nm, we trapped the 100nm gold nanoparticles at only 40mW of laser power whereas at 488nm we required at least 60mW at the back aperture of the trapping objective. We needed less laser intensity to obtain equal confinement and trapping times at 528nm compared to 514nm and 488nm. This is due to the increased scattering cross section closer to resonance and hence stronger interaction between the laser light and the metal nanosphere. Above all, the absolute value of the nanoparticle's polarisability changes considerably close to resonance, thus alternating the gradient force which acts on the nanoparticles (see Sec. 5.3 for further analysis). The trapping times increased from about 10s to several minutes after we raised the power level at each wavelength.

To load nanoparticles in the trap, we moved the stage quickly such that the Stokes forces overcame any optical forces present. The Brownian motion is very significant for particles of this size and results in rapid and large particle displacements. Therefore, temporarily blocking the trapping beam also enabled us to catch nanoparticles

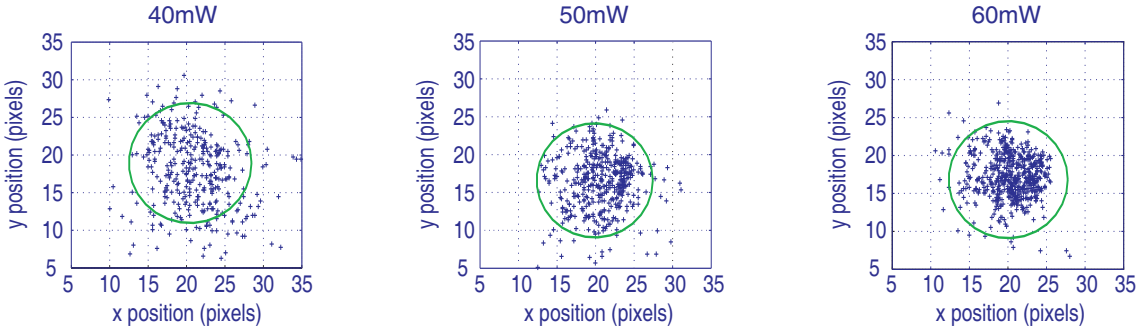

Figure 5.5: We plot the positions (+) of the gold nanoparticle with respect to the LG beam (green circle). In this example we utilised a 514nm LG beam to trap the nanoparticle and increased the laser power from 40mW over 50mW to 60mW. The stronger confinement for higher laser powers is clearly visible.

in the trap. On very few occasions, they entered the trap without external help. However, the gold nanoparticles escaped the trap easier than they were able to enter. This behaviour suggests that the nanoparticles are not deeply confined within the trap. The potential well they have to overcome before entering the trap is higher than the one to exit the trap. Further theoretical analysis confirmed this concept [16]. As the size of the dark core of the LG beam is smaller for shorter laser wavelengths, the trapping region of the gold nanoparticles could be adjusted without changing the azimuthal phase index ℓ of the beam.

We analysed the recorded video images of the particle motion with our own particle tracking software (see Sec. 3.4.1). Figure 5.5 presents representative data extracts for 514nm. The graphs show the positions a trapped 100nm gold sphere visited over time. Increasing the laser power resulted in stronger confinement of the particle. The green circle gives the position of the high intensity ring of the LG beam. In Fig. 5.6 we summarise our results for all three applied wavelengths. The trap site is smallest for 488nm, increasing for 514nm and 528nm. In all experiments the trapped nanosphere resides in the dark core. We analysed the intensity level of each pixel visited by a nanoparticle and displayed this information in the histograms below.

In addition to 100nm gold nanoparticles we also tested 250nm gold particles which are more stably trapped than 100nm particles. These larger gold particles have significantly less Brownian motion and are therefore less subject to those rapid movements that have to be compensated by the trapping laser. We note that micron-sized metallic particles have been trapped using annular light profiles [84] but in such a case, stress that no distinct resonance is involved: as metallic particles increase in size, up to several hundred nanometres, their optical response includes contributions of higher order terms and multiple overlapping resonances. Even larger particles, in the micron-size regime, are more appropriately considered as highly reflective geometrical objects: the physical rationale and interpretation for trapping nanometric

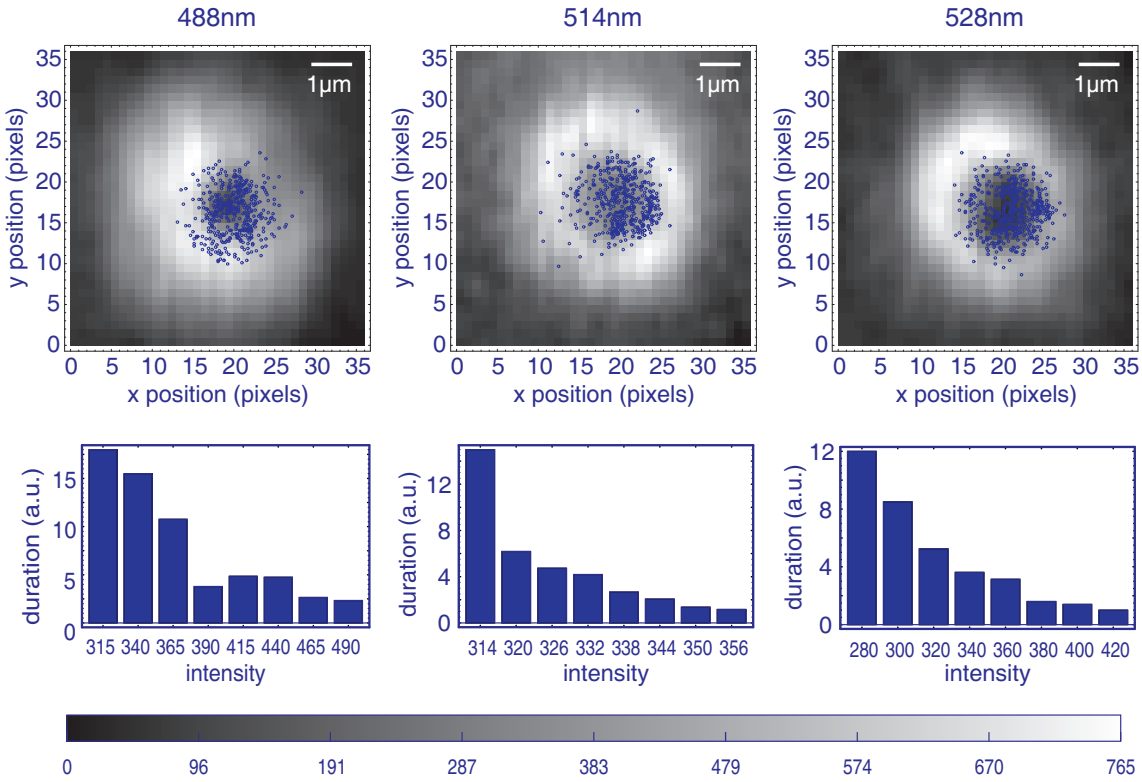

Figure 5.6: *Top* - These three graphs show the positions of the gold nanoparticle with respect to the LG beam for the 488nm, 514nm and 528nm trap. The confined particle resides within the dark core of the LG beam. For this particular experiment we used 120mW at the objective back aperture for the 488nm trap and 90mW for the other two wavelengths. *Bottom* - We analysed the intensity level of each pixel visited by the nanoparticle and the relative duration of a visit. This yields the presented histograms illustrating that the particles remained longest at positions with lowest intensity. These diagrams are a clear evidence of confinement within the low intensity regions of the LG beam. The greyscale intensity shown is the sum of the three colour channels.

sized particles which we consider here is wholly different from that for micron-sized particles [84].

5.2 Orbital angular momentum transfer

In addition to the confinement of the nanoparticles, we observed the transfer of orbital angular momentum (OAM) from the LG beam onto the particle [85]. Once caged by the LG beam, the particles performed a circular motion as we show in Fig. 5.7. They rotated around the beam propagation axis within the dark core of the beam. The sense of their rotation depended upon the sign of the azimuthal index ℓ. We were able to reverse the sense of the rotational motion in our experiments

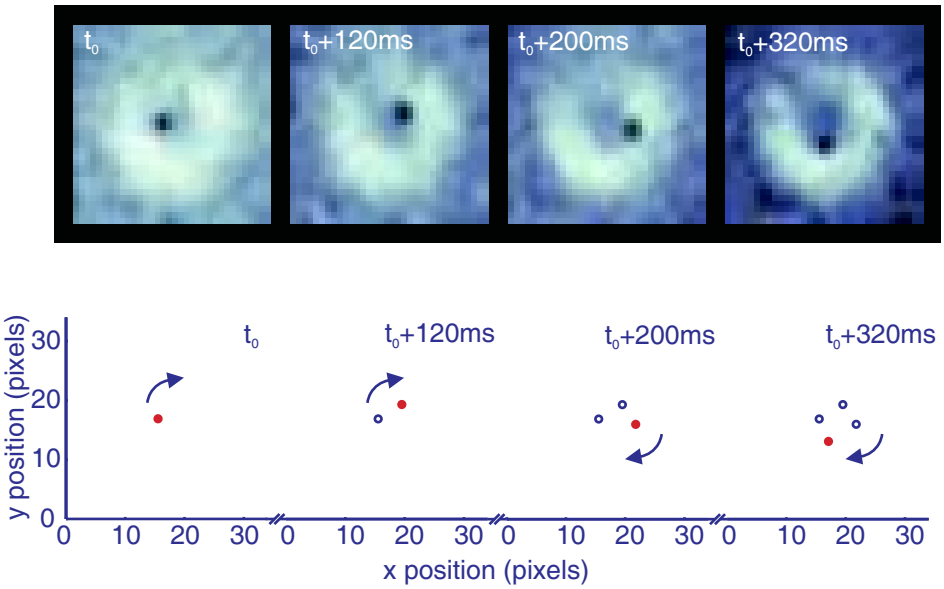

Figure 5.7: *Top* - These four subsequent video frames illustrate the rotation of a 100nm gold particle due to OAM transfer. We used a single-ringed LG beam for this experiment with $\ell = 2$. *Bottom* - We analysed the position of the particle at each time step with our own particle tracking software (see Sec. 3.4.1)

by using an LG beam with $\ell = -2$ instead of $\ell = 2$. To the best of our knowledge 100nm gold nanoparticles are the smallest particles to date for such OAM transfer. There have been numerous experiments in the past rotating micron-sized particles by means of OAM [86–90]. In addition to the rotation of single trapped particles it is possible to rotate a cloud of atoms and pass OAM from a laser beam onto the atoms in a coherent fashion [91].

Because of the helical wavefronts of the LG beam, its Poynting vector exhibits an azimuthal component. This distinct feature gives rise to the OAM of the beam or of $\ell\hbar$ per photon. The OAM of the beam is the fundamental reason for the circular motion of the nanoparticles within the dark core of the LG beam. The nanoparticles start to rotate once they collide with the inner edge of the light annulus of the LG beam. As the particles are overdamped, we assumed a constant speed during the rotation after the accelerating collision with the beam. Between rotations the particles tend to move randomly according to Brownian motion within the dark core.

The rotation rate increased with laser power, reaching a maximum rate of 3.6Hz at 110mW. We found a linear dependence of the rotation rate on power of about 33Hz/W (see Fig. 5.8). This result is in agreement with previous studies on dielectric microparticles [92]. The gold nanoparticles are an order of magnitude smaller than the micron sized beads normally used in OAM experiments. Therefore Brownian motion affects the nanoparticle's trajectory significantly and their displacements are much more rapid. The linear dependence of the rotation rate on laser power is a

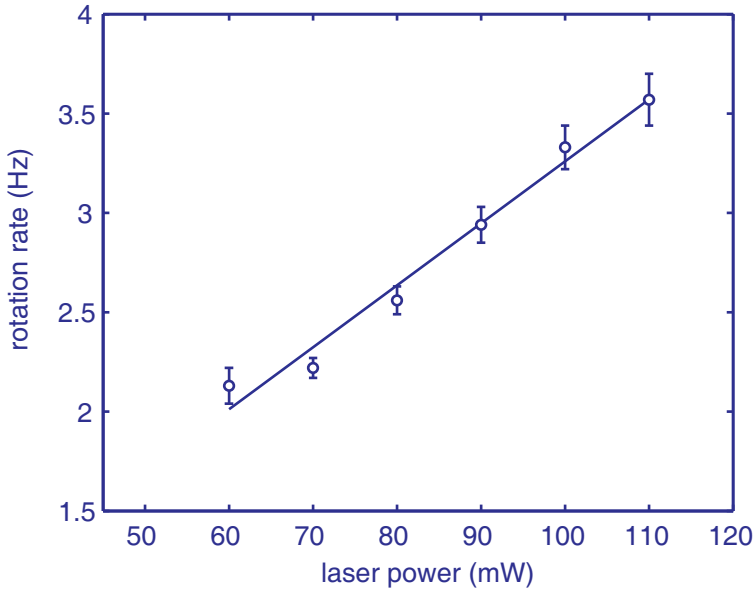

Figure 5.8: This graph represents the OAM transfer rates from the LG beam (514nm, $\ell = 2$) onto a 100nm gold nanoparticle for varying laser powers. The error bars show the standard error of the rotation rate. We increased the applied laser power from 60mW to 110mW resulting in a linear growth of the rotation rate from 2.13 Hz to 3.6Hz.

strong indication that scattering is one of the interaction mechanisms between the laser beam and gold nanoparticles, as OAM is typically transferred by scattering.

We also observed the motion of two nanoparticles simultaneously rotating inside the trap (see Fig. 5.9). The nanoparticles did not attract each other nor coagulate as usually seen in conventional optical tweezers. They repelled each other, resulting in the ejection of one particle out of the trap after only a short period of time. It was thus difficult to confine more than one nanoparticle within the trap if the annulus of light was too small. Only on few occasions we succeeded in confining two nanoparticles. They rotated together within the dark core of the Laguerre-Gaussian beam by keeping the largest distance possible, mostly 180°, apart. These observations suggest an optical binding type interaction [93].

5.3 Results and discussion

After presenting our experiment in the previous sections we now interpret and explain our observations. At this point we find that a valid theoretical model is essential to understand the physical processes leading to our observations. In the first Chapter of this thesis we explained in detail the shortcomings and challenges of the models used to date. We discussed the popular Clausius-Mossotti equation (Eq. (2.24)) and an extended approach using Mie calculations (Eq. (2.43)), both

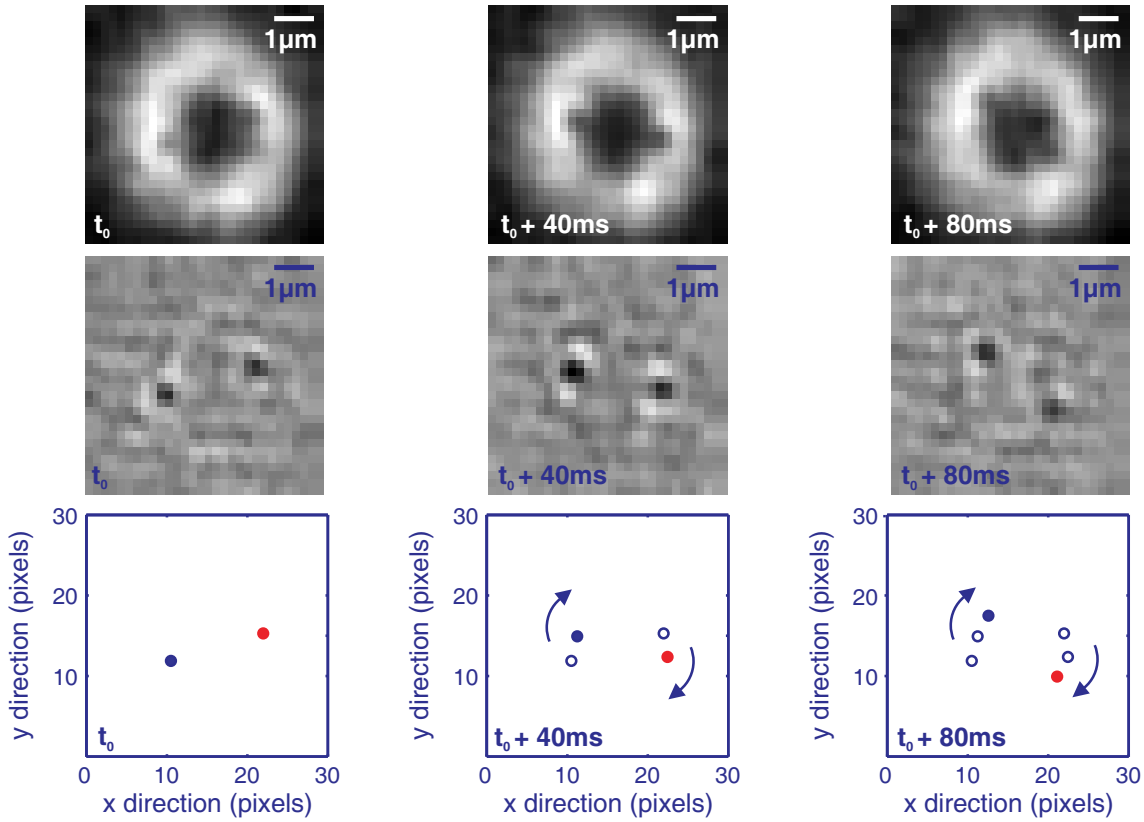

Figure 5.9: We recorded the rotation of two trapped 100nm gold nanoparticles caused by OAM transfer. The particles are confined to the LG beam. However the strong repulsion between the spheres counterbalances the repulsion mediated by the LG beam and does not allow them to interact in the middle of the dark core. Together they rotate clockwise, retaining a separation angle of 180°. We displayed the noise-reduced movie stills of a video sequence in the first row which we processed further with a background subtraction in the second row. The third row presents the positions of the nanoparticles we analysed with our own particle tracking software (see Sec. 3.4.1).

yielding the polarisability α of a metal nanoparticle. The real part of the polarisability $\Re\{\alpha\}$ determines the gradient or dipolar force $\mathrm{F}_{\mathrm{grad}}$ of the force decomposition model (Eq. (2.57)-(2.59)). These equations are briefly repeated here to spare the reader the quest of finding them in previous chapters:

$$\alpha = 3\mathrm{V}\,\frac{\varepsilon_{\mathrm{metal}}(\omega)-\varepsilon_{\mathrm{host}}}{\varepsilon_{\mathrm{metal}}(\omega)+2\varepsilon_{\mathrm{host}}} \qquad \text{(Eq. (2.24))}$$

$$\alpha_{\mathrm{ext}} = \frac{1-\frac{1}{10}(\varepsilon_{\mathrm{metal}}+\varepsilon_{\mathrm{host}})\mathrm{x}^2+O(\mathrm{x}^4)}{\left(\frac{1}{3}+\frac{\varepsilon_{\mathrm{host}}}{\varepsilon_{\mathrm{metal}}-\varepsilon_{\mathrm{host}}}\right)-\frac{1}{30}(\varepsilon_{\mathrm{metal}}+10\varepsilon_{\mathrm{host}})\mathrm{x}^2-i\,\frac{4\pi^2\varepsilon_{\mathrm{host}}^{2/3}}{3}\frac{\mathrm{V}}{\lambda_0^3}+O(\mathrm{x}^4)} \qquad \text{(Eq. (2.43))}$$

$$\langle\mathbf{F}_{\mathrm{grad}}\rangle = \frac{1}{4}\varepsilon_0\varepsilon_{\mathrm{r}}\Re\{\alpha\}\nabla(\mathbf{E}^*\mathbf{E}) \qquad \text{(Eq. (2.57))}$$

$$\langle\mathbf{F}_{\mathrm{scat}}\rangle = \frac{\mathrm{n}_{\mathrm{host}}}{\mathrm{c}}\mathrm{C}_{\mathrm{scat}}\langle\mathbf{S}\rangle \qquad \text{(Eq. (2.58))}$$

$$\langle\mathbf{F}_{\mathrm{abs}}\rangle = \frac{\mathrm{n}_{\mathrm{host}}}{\mathrm{c}}\mathrm{C}_{\mathrm{abs}}\langle\mathbf{S}\rangle \qquad \text{(Eq. (2.59))}$$

In contrast to this detailed breakdown of the forces, the Maxwell stress tensor merely gives a total force exerted by light on a particle. The total force calculation using the Maxwell stress tensor does not help in this discussion as these do not yield single force components attributed to the various physical effects. Hence, this model is not able to answer our question of the underlying processes. It supports our observations that the total force on the gold nanoparticle is repulsive when exposed to laser light shorter than the resonance wavelength [16]. Therefore we continue to analyse our blue-detuned experiment in the light of the force decomposition model.

We observed that gold nanoparticles are repelled by laser light using a wavelength shorter than their resonance. The force decomposition model may help to find the answer what causes this effect which is in direct contrast to the attraction of the nanoparticles observed in tweezing experiments using a laser wavelength much longer than their resonance. We discussed earlier that the main properties changing at resonance are the scattering and absorption cross section of the particle as well as its polarisability α. These quantities directly affect the scattering, absorption and gradient force.

We calculated the scattering and absorption cross section of 100nm gold particles in Chapter 2. These are displayed in Fig. 5.10 once again for comparison with the polarisability in Fig. 5.11. We see an increase in scattering and absorption around the resonance. However it is not exactly clear where the definite resonance of a 100nm gold sphere is. The scattering maximum is at 579nm, the absorption maximum at 532nm and the maximum of its polarisability α at 564nm. In addition, the latter depends on the model used to determine α. We can say for certain that

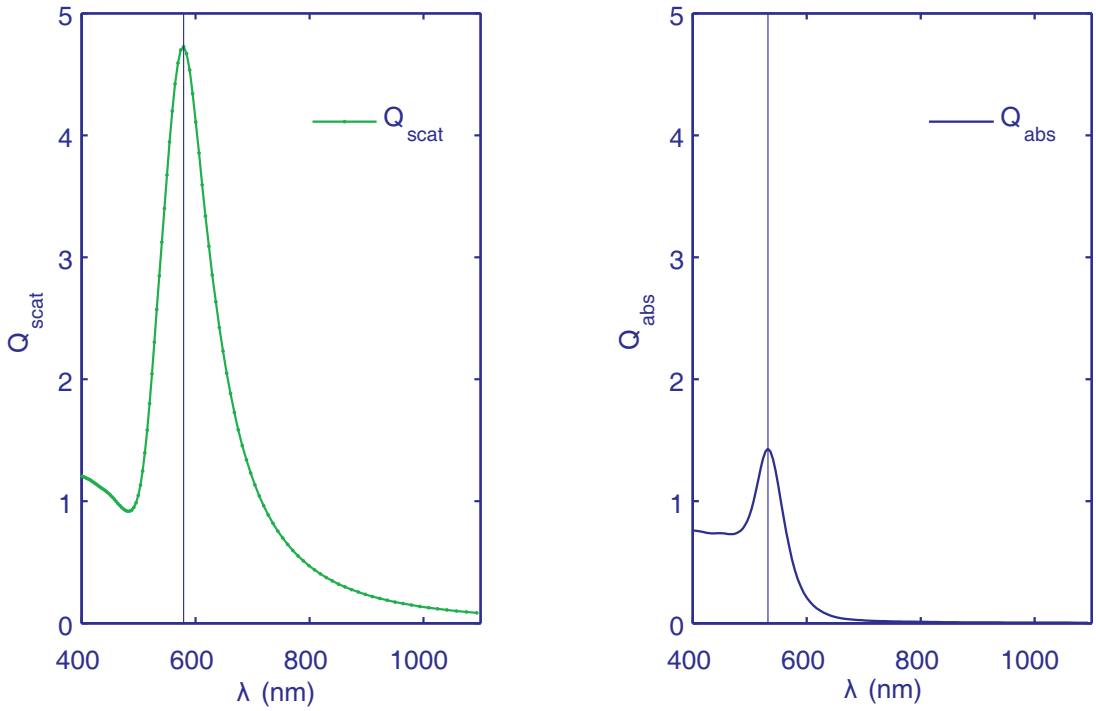

Figure 5.10: *Left* - The scattering efficiency Q_{scat} of a 100nm gold sphere has its maximum at 579nm. We calculated the scattering cross section C_{scat} with Mie theory (see Chapter 2) and divided it with the sphere's surface to obtain the efficiency (see Eq. (2.34)). *Rigth* - Equivalently we obtained the absorption effiency Q_{abs} from Mie theory. Its maximum for a 100nm gold sphere is situated at 532nm. The vertical lines mark the cross section maxima.

scattering and absorption (and thus heating) of metal nanoparticles is significantly increased close to their resonance as compared to the infrared. As Q_{scat} and α are the most important quantities regarding our observations we assume the nanoparticle's resonance to be around 570nm, bearing in mind that its absorption maximum is slightly below this wavelength.

Following the Clausius-Mossotti approach (Eq. (2.24)), we obtain the polarisability α of a 100nm gold sphere as plotted on the left-hand side of Fig. 5.11. The real part of the polarisability remains positive below resonance, although decreased compared to its value in the infrared where typical tweezing experiments take place (for example 1064nm). Thus, this model suggest a decrease of the attracting gradient force compared to the gradient force of a tweezing experiment in the infrared. Together with the enhanced scattering cross section close to resonance, the logical conclusion is that the repulsion is the result of a diminished gradient force and an increased scattering force [16].

However, if we use the extended model (Eq. (2.43)) to calculate the polarisability α (plotted on the right-hand side of Fig. 5.11) we suddenly see a negative value

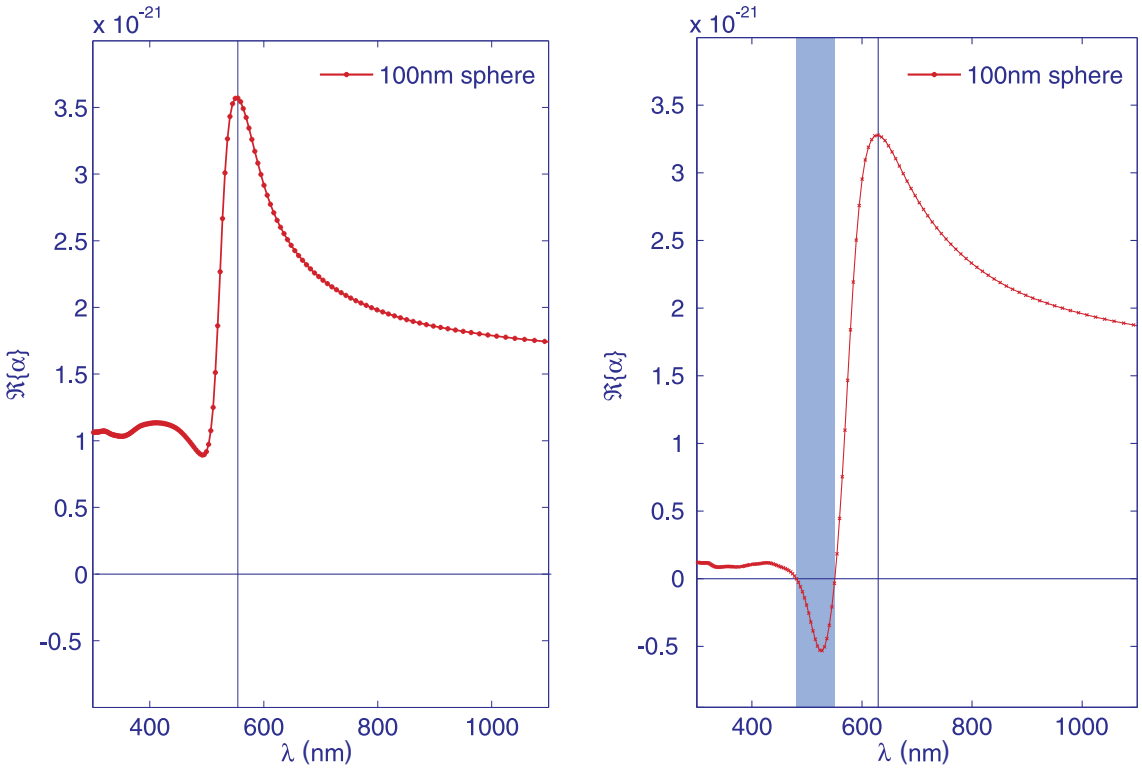

Figure 5.11: *Left* - The real part of the polarisability $\Re\{\alpha\}$ of a 100nm gold sphere, calculated with the Clausius-Mossotti equation (Eq. (2.24)), remains positive throughout the considered spectral range. The plasmon resonance itself is narrower and not red-shifted as expected from Mie theory. The vertical line marks the maximum of the polarisability for better comparison. *Right* - We calculated $\Re\{\alpha\}$ with the extended model (Eq. (2.43)). In contrast to the Clausius-Mossotti approach, it includes the broadening and red-shifting of the resonance for the 100nm gold sphere. The important difference is the negative value of $\Re\{\alpha\}$ on the blue side of the plasmon resonance. We highlighted this region where we conducted our blue-detuned experiments.

for α of a 100nm gold sphere at the questionable wavelength region. Here, we can now argue that the gradient force is repulsive just as the atomic analogue would suggest. This and the increase of the scattering force result in repulsion of the metal nanoparticle from the laser light.

Which interpretation is correct? We argued in Chapter 2 that both models lack validity. One could say that the extended model is 'more correct' and hence we do see a repulsion caused by a negative gradient force. The increased scattering definitely helps to repel the particle, no matter how repulsive the gradient force is. The very fact we observe rotation of the nanoparticles is a strong indication that scattering between the light field and particle is an interaction mechanism simultaneously present to repulsion caused by the gradient force. The big question is if

this force decomposition remains valid for particles much larger than the Rayleigh regime. There is still a lot to do on the theoretical side of trapping metal nanoparticles. Experimentally, the work presented in this thesis is a good start to shine more light on trapping close to resonance.

5.4 Conclusion

We presented the results of our work on trapping of metal nanoparticles close to resonance. This is a first attempt to investigate the trapping behaviour of metal nanoparticles on the blue-detuned side of their plasmon resonance [16,47]. Contrary to standard optical tweezing experiments the gold nanoparticles are not trapped in the tight focus of a Gaussian beam. They are repelled from high intensity regions of the trapping laser if the trapping wavelength is below their resonance. Thus we confined the 100nm gold spheres in the dark core of a single-ringed LG beam.

We changed our optical setup accordingly to create and introduce the LG beam to the trap site. We monitored the particle motion with a CCD camera and subsequently analysed the recorded video footage with our own particle tracking software. Our investigations included a variation of the trapping wavelength and power levels. We were able to confine 100nm gold spheres at three different wavelengths (488nm, 514nm, 528nm - all below the resonance wavelength) and for laser powers ranging from 40-110mW at the back aperture of our objective. The area of confinement decreased for larger laser powers while the trapping times increased. The dark core of the LG beam was larger for longer wavelengths which also affected the area of confinement.

Once confined, the particles showed circular motion inside the trap which we attributed to OAM transfer from the LG beam onto the particles. This additional feature originates from the distinct phase properties of the LG beam in addition to the doughnut-shaped intensity profile. We found that the rotation rate of the particles increases linearly with power. This is due to the fact that OAM is dominantly transferred by scattering. We also observed several particles within the trap. In contrast to optical tweezers they repelled each other and kept the largest possible distance while rotating inside the dark vortex core of the LG beam.

The interpretation of the force mechanism acting on the trapped particles proves difficult as we lack a valid theoretical model. We suggested two possible interpretations. Both assume the presence of the scattering force. We do not believe that the confinement of the particles is based on the scattering force alone, however we cannot say for certain if it is the dominating force. After our analysis in Chapter 2 we favour the interpretation of the gradient force turning repulsive on the blue-detuned side of the resonance over it only decreasing in magnitude. This concludes from our calculations concering the polarisability α which is directly linked to the gradient force. The repulsive gradient force and the scattering force both repel the particles

away from the high intensity regions of the trapping laser and are thus working together to create the observed effect of repulsion.

To further understand the actual physical mechanisms during blue-detuned trapping of metal nanoparticles one needs to design a different experiment that is able to differentiate between scattering and gradient forces. A setup with the ability to fine-tune the laser wavelength should prove advantageous as one could directly probe the non-coinciding scattering and polarisability maxima.

6 Summary and Outlook

This thesis investigated the particle plasmon resonance of metal nanoparticles in the light of optical trapping. We explored the impact of the resonance on the trapping properties both theoretically and experimentally. There are two regimes we distinguished: blue-detuned and red-detuned trapping. The former applies trapping laser wavelengths longer than the plasmon resonance of the nanoparticle and the latter wavelengths shorter than that.

At first we theoretically examined the effect of using various laser wavelengths to trap gold and silver nanoparticles. We analysed the position of the particle plasmon resonance based on the optical properties of metal nanoparticles. For this we focussed on the polarisability α and Mie's cross sections C_{scat} and C_{abs}. It turned out that it remains difficult to make valid theoretical predictions based on the commonly employed polarisability description because of the size scale of our metal nanoparticles. However this polarisability description is the very basis for the force decomposition model that explains optical trapping based on the three simultaneously acting forces: gradient, scattering and absorption force. The gradient force is by definition a force acting on a dipole and thus problematic for exposing a 100nm gold sphere to a 488nm laser. To address this deficiency we explored an extended model for the polarisability and tried to retrieve the polarisability from the exact Mie cross sections. Finally the experiments described in the second half of this thesis confirmed our theoretical considerations.

We employed three different trapping geometries throughout this work: a dual beam fibre trap, single beam tweezers and a dark core LG trap. For our red-detuned experiments we trapped metal nanoparticles in the high intensity region of tightly focussed single beam tweezers. We used the infrared part of a pulsed supercontinuum source instead of a cw single-line laser and thus demonstrated that tweezing metal nanoparticles with a pulsed laser is indeed possible. Additionally we discovered new features in our data that seem to be induced by the pulsed laser source and require further investigation. The gold nanoparticles were repelled by the high intensity regions of the trapping laser on the blue-detuned side of their resonance. Therefore we chose an alternative trapping geometry to the standard tweezers. The dark core LG trap formed our tool to manipulate gold nanoparticles on the blue-detuned side of their resonance.

We made an effort to improve the live imaging of metal nanoparticles during our experiments. After exploring various methods including brightfield and darkfield techniques alike we found the episcopic brightfield Koehler illumination most useful.

The improved imaging also enabled us to preselect trapped particles prior to taking their data. Based on their colour we could determine an appropriate shape and size. Also we were able to see if there was a single particle in the trap or several ones. We relied on video detection analysed with particle tracking and quadrant-photodiode detection for acquiring our data.

In the second half of this thesis we discussed our experimental results. We were able to reproduce the main characteristics of gold and silver nanoparticle trapping as explored by other groups. This included mainly a rise in trap stiffness with increased power as well as a decrease in trap stiffness for smaller particles. Our study compared optical trapping of 80nm silver spheres as well as 80nm and 100nm gold spheres at 4 different power levels (25mW, 33mW, 40mW, 48mW). We did see differences to other group's result that we believe are because of the pulsed laser source. In particular the trapping powers we used to trap the nanoparticles are lower than reported so far. The nanoparticles are trapped by the high intensity laser pulses. Their repetition rate is high enough that the particles were not able to escape the trap due to their Brownian motion. We thus needed less average power for trapping. We also believe that the peak powers caused the disintegration of the nanoparticles at higher laser powers. We expected a wavelength dependence of the trap stiffness from our theoretical considerations; this property remains to be explored.

We investigated the blue-detuned side of the resonance of 100nm gold spheres. This is a new approach to study metal nanoparticle's trapping behaviour as most experiments are conducted on the red-detuned side. This experiment demonstrated the analogy between trapping atoms and metal nanoparticles. We discovered a repulsion of the particles away from high intensity regions. Based on our previous theoretical considerations the interpretation of this observed effect is ambiguous. However we believe that the repulsion is the result of a repulsive gradient force and increased scattering. Additionally we observed, contrary to a red-detuned trap, that particles themselves repel each other at the trap site. This also proved the repulsion of metal nanoparticles from blue-detuned laser light.

In addition to blue-detuned trapping we took advantage of the orbital angular momentum of the LG beam that caused the metal nanoparticles to rotate in the trap. We measured the transfer of OAM from the beam onto the particle. The rotation rate of the nanoparticles within the trap site increased linearly with power. This observation suggests a considerable scattering force component in this experiment. We even observed the rotation of two particles trapped at once. By scattering the repulsive light of the trapping laser they kept the largest distance possible rotating separated by 180° around the beam axis.

For future research we see two questions that remain to be explored. First a thorough reassessment of the theoretical framework for force decomposition appears necessary. One possibility might be an extension of the existing formalism for higher orders including quadrupolar effects. That is defining the polarisability beyond

the dipolar description and potentially adding another force term to the dipolar (gradient) force. We came to the conclusion that the quasi-static approximation for the polarisability of metal nanoparticles is not accurate enough to describe plasmon based optical trapping and thus disagree with common practise within the trapping community.

Second an experimental study on the wavelength dependence of the trap stiffness appears to be very valuable to support any new theoretical framework. Also we believe that there is potential to optimise the trapping of metal nanoparticles by including resonant effects. A well balanced trapping wavelength with increased gradient force due to resonant enhancement, yet at the same time moderate increase in scattering and absorption promises interesting applications. Trapped metal nanoparticles may serve as useful tool in biophotonics for sensing and nanosurgery. These applications in particular require minimum absorption to avoid heating of the nanoprobe which would damage the biological sample. Additionally exploring resonant trapping further should open up new possibilities for nonlinear processes within the trap.

Bibliography

[1] K.C. Neuman and S.M. Block. Optical trapping. *Review of Scientific Instruments*, 75:2787, 2004.

[2] K. Dholakia, P. Reece, and M. Gu. Optical micromanipulation. *Chemical Society Reviews*, 37(1):42–55, 2008.

[3] E. Ozbay. Plasmonics: Merging photonics and electronics at nanoscale dimensions. *Science*, 311(5758):189, 2006.

[4] M. Pelton, J. Aizpurúa, and G. Bryant. Metal-nanoparticle plasmonics. *Laser & Photon. Rev*, 2:136–159, 2008.

[5] A. Ashkin. Applications of laser radiation pressure. *Science*, 210(4474):1081, 1980.

[6] K. Sasaki, M. Koshioka, H. Misawa, N. Kitamura, and H. Masuhara. Optical trapping of a metal particle and a water droplet by a scanning laser beam. *Applied Physics Letters*, 60:807, 1992.

[7] K. Svoboda and S.M. Block. Optical trapping of metallic Rayleigh particles. *Optics Letters*, 19(13):930–932, 1994.

[8] J.E. Molloy and M.J. Padgett. Lights, action: optical tweezers. *Contemporary Physics*, 43(4):241–258, 2002.

[9] J. Prikulis, F. Svedberg, M. Käll, J. Enger, K. Ramser, M. Goksor, and D. Hanstorp. Optical spectroscopy of single trapped metal nanoparticles in solution. *Nano Letters*, 4(1):115–118, 2004.

[10] K.C. Toussaint, M. Liu, M. Pelton, J. Pesic, M.J. Guffey, P. Guyot-Sionnest, and N.F. Scherer. Plasmon resonance-based optical trapping of single and multiple Au nanoparticles. *Optics Express*, 15(19):12017–12029, 2007.

[11] M. Righini, A.S. Zelenina, C. Girard, and R. Quidant. Parallel and selective trapping in a patterned plasmonic landscape. *Nature Physics*, 3(7):477–480, 2007.

[12] M.L. Juan, R. Gordon, Y. Pang, F. Eftekhari, and R. Quidant. Self-induced back-action optical trapping of dielectric nanoparticles. *Nature Physics*, 2009. [doi:10.1038/nphys1422].

[13] P.M. Hansen, V.K. Bhatia, N. Harrit, and L. Oddershede. Expanding the optical trapping range of gold nanoparticles. *Nano Letters*, 5(10):1937–1942, 2005.

[14] L. Bosanac, T. Aabo, P.M. Bendix, and L.B. Oddershede. Efficient optical trapping and visualization of silver nanoparticles. *Nano Letters*, 8(5):1486–1491, 2008.

[15] M. Pelton, M. Liu, H. Y. Kim, G. Smith, P. Guyot-Sionnest, and N. F. Scherer. Optical trapping and alignment of single gold nanorods by using plasmon resonances. *Optics Letters*, 31(13):2075–2077, 2006.

[16] M. Dienerowitz, M. Mazilu, P.J. Reece, T.F. Krauss, and K. Dholakia. Optical vortex trap for resonant confinement of metal nanoparticles. *Optics Express*, 16(7):4991–4999, 2008.

[17] A. Ashkin, J.M. Dziedzic, J.E. Bjorkholm, and S. Chu. Observation of a single-beam gradient force optical trap for dielectric particles. *Optics Letters*, 11(5):288, 1986.

[18] K. Svoboda and S.M. Block. Biological applications of optical forces. *Annual Review of Biophysics and Biomolecular Structure*, 23(1):247–285, 1994.

[19] T. Sugiura, T. Okada, Y. Inouye, O. Nakamura, and S. Kawata. Gold-bead scanning near-field optical microscope with laser-force position control. *Optics letters*, 22(22):1663–1665, 1997.

[20] F. Svedberg, Z. Li, H. Xu, and M. Käll. Creating hot nanoparticle pairs for surface-enhanced Raman spectroscopy through optical manipulation. *Nano Letters*, 6(12):2639–2641, 2006.

[21] K. Sasaki, J. Hotta, K. Wada, and H. Masuhara. Analysis of radiation pressure exerted on a metallic particle within an evanescent field. *Optics Letters*, 25(18):1385–1387, 2000.

[22] Y. Seol, A.E. Carpenter, and T.T. Perkins. Gold nanoparticles: enhanced optical trapping and sensitivity coupled with significant heating. *Optics Letters*, 31(16):2429–2431, 2006.

[23] R.R. Agayan, F. Gittes, R. Kopelman, and C.F. Schmidt. Optical trapping near resonance absorption. *Applied optics*, 41(12):2318–2327, 2002.

[24] J.R. Arias-Gonzalez and M. Nieto-Vesperinas. Optical forces on small particles: attractive and repulsive nature and plasmon-resonance conditions. *Journal of the Optical Society of America A*, 20(7):1201–1209, 2003.

[25] A.S. Zelenina, R. Quidant, G. Badenes, and M. Nieto-Vesperinas. Tunable optical sorting and manipulation of nanoparticles via plasmon excitation. *Optics Letters*, 31(13):2054–2056, 2006.

[26] S.A. Maier. *Plasmonics: Fundamentals and Applications*. Springer Verlag, 2007.

[27] C.F. Klingshirn. *Semiconductor optics*. Springer Verlag, 2007.

[28] C.F. Bohren and D.R. Huffman. *Absorption and scattering of light by small particles*. Wiley-Interscience, 1983.

[29] N.W. Ashcroft and N.D. Mermin. *Solid state physics*. Singapore, 1976.

[30] J.D. Jackson. *Klassische Elektrodynamik*. de Gruyter, 2002.

[31] P.B. Johnson and R.W. Christy. Optical constants of the noble metals. *Physical Review B, Solid State*, 6(12):4370–4379, 1972.

[32] L. Novotny and B. Hecht. *Principles of Nano-Optics*. Cambridge University Press: New York, 2006.

[33] M. Zhu, G. Qian, G. Ding, Z. Wang, and M. Wang. Plasma resonance of silver nanoparticles deposited on the surface of submicron silica spheres. *Materials Chemistry & Physics*, 96(2-3):489–493, 2006.

[34] G. Dolling, M. Wegener, C.M. Soukoulis, and S. Linden. Negative-index metamaterial at 780 nm wavelength. *Optics Letters*, 32(1):53–55, 2007.

[35] A. Ashkin. Forces of a single-beam gradient laser trap on a dielectric sphere in the ray optics regime. *Biophysical Journal*, 61(2):569–582, 1992.

[36] S. Chu, JE Bjorkholm, A. Ashkin, and A. Cable. Experimental observation of optically trapped atoms. *Physical Review Letters*, 57(3):314–317, 1986.

[37] J.P. Gordon. Radiation forces and momenta in dielectric media. *Physical Review A*, 8(1):14–21, 1973.

[38] C. Selhuber-Unkel, I. Zins, O. Schubert, C. Sönnichsen, and L.B. Oddershede. Quantitative Optical Trapping of Single Gold Nanorods. *Nano Letters*, 8(9):2998–3003, 2008.

[39] M. Meier and A. Wokaun. Enhanced fields on large metal particles: dynamic depolarization. *Optics Letters*, 8(11):581–583, 1983.

[40] T. Kokkinakis and K. Alexopoulos. Observation of radiative decay of surface plasmons in small silver particles. *Physical Review Letters*, 28(25):1632–1634, 1972.

[41] A. Wokaun, J.P. Gordon, and P.F. Liao. Radiation damping in surface-enhanced Raman scattering. *Physical Review Letters*, 48(14):957–960, 1982.

[42] H. Kuwata, H. Tamaru, K. Esumi, and K. Miyano. Resonant light scattering from metal nanoparticles: Practical analysis beyond Rayleigh approximation. *Applied Physics Letters*, 83:4625, 2003.

[43] A.J. Hallock, P.L. Redmond, and L.E. Brus. Optical forces between metallic particles. *Proceedings of the National Academy of Sciences*, 102(5):1280–1284, 2005.

[44] Z. Li, M. Käll, and H. Xu. Optical forces on interacting plasmonic nanoparticles in a focused gaussian beam. *Phys. Rev. B*, 77(8):085412, 2008.

[45] J.P. Barton and D.R. Alexander. Fifth-order corrected electromagnetic field components for a fundamental Gaussian beam. *Journal of Applied Physics*, 66:2800, 1989.

[46] J.P. Barton, D.R. Alexander, and S.A. Schaub. Theoretical determination of net radiation force and torque for a spherical particle illuminated by a focused laser beam. *Journal of Applied Physics*, 66:4594, 1989.

[47] M. Dienerowitz, M. Mazilu, and K. Dholakia. Optical manipulation of nanoparticles: a review. *Journal of Nanophotonics*, 2(1):021875, 2008.

[48] J.P. Gordon. Radiation forces and momenta in dielectric media. *Physical Review A*, 8:14, 1969.

[49] A. Ashkin and J.P. Gordon. Stability of radiation-pressure particle traps: an optical Earnshaw theorem. *Optics Letters*, 8(10):511–513, 1983.

[50] G. Pesce, G. Volpe, A.C.D. Luca, G. Rusciano, and G. Volpe. Quantitative assessment of non-conservative radiation forces in an optical trap. *Europhysics Letters*, 86:38002, 2009.

[51] Y. Roichman, B. Sun, A. Stolarski, and D.G. Grier. Influence of nonconservative optical forces on the dynamics of optically trapped colloidal spheres: The fountain of probability. *Physical Review Letters*, 101(12):128301, 2008.

[52] M. Danckwerts and L. Novotny. Optical frequency mixing at coupled gold nanoparticles. *Physical Review Letters*, 98(2):26104, 2007.

[53] S. Kujala, B.K. Canfield, M. Kauranen, Y. Svirko, and J. Turunen. Multipole interference in the second-harmonic optical radiation from gold nanoparticles. *Physical Review Letters*, 98(16):167403, 2007.

[54] A. Pralle, M. Prummer, E.L. Florin, E.H.K. Stelzer, and J.K.H. Hörber. Three-dimensional high-resolution particle tracking for optical tweezers by forward scattered light. *Microscopy Research and Technique*, 44:378–386, 1999.

[55] K. Berg-Sørensen and H. Flyvbjerg. Power spectrum analysis for optical tweezers. *Review of Scientific Instruments*, 75:594, 2004.

[56] www.britishbiocell.co.uk.

[57] S.N.S. Reihani and L.B. Oddershede. Optimizing immersion media refractive index improves optical trapping by compensating spherical aberrations. *Optics Letters*, 32(14):1998–2000, 2007.

[58] N.K. Metzger, K. Dholakia, and E.M. Wright. Observation of bistability and hysteresis in optical binding of two dielectric spheres. *Physical Review Letters*, 96:068102, 2002.

[59] P.R.T. Jess, V. Garcés-Chávez, D. Smith, M. Mazilu, L. Paterson, A. Riches, C.S. Herrington, W. Sibbett, and K. Dholakia. Dual beam fibre trap for Raman micro-spectroscopy of single cells. *Optics Express*, 14(12):5779–5791, 2006.

[60] A. van der Horst, A.I. Campbell, L.K. van Vugt, D.A. Vanmaekelbergh, M. Dogterom, and A. van Blaaderen. Manipulating metal-oxide nanowires using counter-propagating optical line tweezers. *Optics Express*, 15(18):11629–11639, 2007.

[61] R.A. Farrer, F.L. Butterfield, V.W. Chen, and J.T. Fourkas. Highly efficient multiphoton-absorption-induced luminescence from gold nanoparticles. *Nano Letters*, 5(6):1139–1142, 2005.

[62] C. Sönnichsen, T. Franzl, T. Wilk, G. Von Plessen, J. Feldmann, O. Wilson, and P. Mulvaney. Drastic reduction of plasmon damping in gold nanorods. *Physical Review Letters*, 88(7):77402–77402, 2002.

[63] C. Sönnichsen, B.M. Reinhard, J. Liphardt, and A.P. Alivisatos. A molecular ruler based on plasmon coupling of single gold and silver nanoparticles. *Nature biotechnology*, 23(6):741–745, 2005.

[64] A. Csaki, F. Garwe, A. Steinbruck, G. Maubach, G. Festag, A. Weise, I. Riemann, K. Konig, and W. Fritzsche. A parallel approach for subwavelength molecular surgery using gene-specific positioned metal nanoparticles as laser light antennas. *Nano Letters*, 7(2):247–253, 2007.

[65] www.micro.magnet.fsu.edu/primer/.

[66] www.microscopyu.com.

[67] S. Keen, J. Leach, G. Gibson, and M.J. Padgett. Comparison of a high-speed camera and a quadrant detector for measuring displacements in optical tweezers. *Journal of Optics A: Pure and Applied Optics*, 9(8):264, 2007.

[68] L.P. Ghislain, N.A. Switz, and W.W. Webb. Measurement of small forces using an optical trap. *Review Of Scientific Instruments*, 65:2762, 1994.

[69] E.L. Florin, A. Pralle, E.H.K. Stelzer, and J.K.H. Hörber. Photonic force microscope calibration by thermal noise analysis. *Applied Physics A: Materials Science & Processing*, 66:75–78, 1998.

[70] M.W. Allersma, F. Gittes, M.J. deCastro, R.J. Stewart, and C.F. Schmidt. Two-dimensional tracking of ncd motility by back focal plane interferometry. *Biophysical Journal*, 74(2):1074–1085, 1998.

[71] F. Gittes and C.F. Schmidt. Interference model for back-focal-plane displacement detection in optical tweezers. *Optics Letters*, 23(1):7–9, 1998.

[72] http://en.wikipedia.org/wiki/Viscosity.

[73] E.J.G. Peterman, F. Gittes, and C.F. Schmidt. Laser-induced heating in optical traps. *Biophysical Journal*, 84(2):1308–1316, 2003.

[74] L. Oddershede, S. Grego, S. Nørrelykke, and K. Berg-Sørensen. Optical tweezers: probing biological surfaces. *Probe Microscopy*, 2:129–137, 2001.

[75] B. Agate, C. Brown, W. Sibbett, and K. Dholakia. Femtosecond optical tweezers for in-situ control of two-photon fluorescence. *Optics Express*, 12(13):3011–3017, 2004.

[76] J. Nappa, G. Revillod, I. Russier-Antoine, E. Benichou, C. Jonin, and PF Brevet. Electric dipole origin of the second harmonic generation of small metallic particles. *Physical Review B*, 71(16):165–407, 2005.

[77] L. Malmqvist and H.M. Hertz. Second-harmonic generation in optically trapped nonlinear particles with pulsed lasers. *Applied Optics*, 34(18):3392–3397, 1995.

[78] L. Pan, A. Ishikawa, and N. Tamai. Detection of optical trapping of CdTe quantum dots by two-photon-induced luminescence. *Physical Review B*, 75(16):161305, 2007.

[79] L.G. Wang and C.L. Zhao. Dynamic Radiation Force of a Pulsed Gaussian Beam Acting on Rayleigh Dielectric Sphere. *Optics Express*, 15(17):10615–10621, 2007.

[80] L. Allen, M.W. Beijersbergen, R.J.C. Spreeuw, and J.P. Woerdman. Orbital angular momentum of light and the transformation of Laguerre-Gaussian laser modes. *Physical Review A*, 45(11):8185–8189, 1992.

[81] J. Courtial, K. Dholakia, L. Allen, and M.J. Padgett. Second-harmonic generation and the conservation of orbital angular momentum with high-order Laguerre-Gaussian modes. *Physical Review A*, 56(5):4193–4196, 1997.

[82] Eugene Hecht. *Optics*. Addison Wesley, 2002.

[83] M.A. Clifford, J. Arlt, J. Courtial, and K. Dholakia. High-order Laguerre–Gaussian laser modes for studies of cold atoms. *Optics Communications*, 156(4-6):300–306, 1998.

[84] A.T. O'Neil and M.J. Padgett. Three-dimensional optical confinement of micron-sized metal particles and the decoupling of the spin and orbital angular momentum within an optical spanner. *Optics Communications*, 185(1-3):139–143, 2000.

[85] M. Dienerowitz and K. Dholakia. Transfer of Orbital Angular Momentum from an Optical Vortex Beam to a Nanoparticle. *Topologica*, 2:008–1–008–7, 2009.

[86] H. He, M.E.J. Friese, N.R. Heckenberg, and H. Rubinsztein-Dunlop. Direct observation of transfer of angular momentum to absorptive particles from a laser beam with a phase singularity. *Physical Review Letters*, 75(5):826–829, 1995.

[87] M.E.J. Friese, J. Enger, H. Rubinsztein-Dunlop, and N.R. Heckenberg. Optical angular-momentum transfer to trapped absorbing particles. *Physical Review A*, 54(2):1593–1596, 1996.

[88] N.B. Simpson, K. Dholakia, L. Allen, and M.J. Padgett. Mechanical equivalence of spin and orbital angular momentum of light: an optical spanner. *Optics Letters*, 22(1):52–54, 1997.

[89] A.T. O'Neil, I. MacVicar, L. Allen, and M.J. Padgett. Intrinsic and extrinsic nature of the orbital angular momentum of a light beam. *Physical Review Letters*, 88(5):53601, 2002.

[90] A.J. Wright, J.M. Girkin, G.M. Gibson, J. Leach, and M.J. Padgett. Transfer of orbital angular momentum from a super-continuum, white-light beam. *Optics Express*, 16(13):9495–9500, 2008.

[91] M.F. Andersen, C. Ryu, P. Clade, V. Natarajan, A. Vaziri, K. Helmerson, and W.D. Phillips. Quantized rotation of atoms from photons with orbital angular momentum. *Physical Review Letters*, 97(17):170406, 2006.

[92] A. Rohrbach and E.H.K. Stelzer. Optical trapping of dielectric particles in arbitrary fields. *Journal of the Optical Society of America A*, 18(4):839–853, 2001.

[93] D.S. Bradshaw and D.L. Andrews. Interactions between spherical nanoparticles optically trapped in Laguerre-Gaussian modes. *Optics Letters*, 30(22):3039–3041, 2005.

List of publications

Peer-reviewed publications

- M. Dienerowitz, M. Mazilu, P.J. Reece, T.F. Krauss, and K. Dholakia. "Optical vortex trap for resonant confinement of metal nanoparticles", *Optics Express*, 16(7):4991-4999, 2008
- M. Dienerowitz, M. Mazilu, and K. Dholakia. "Optical manipulation of nanoparticles: a review", *Journal of Nanophotonics*, 2(1):021875, 2008
- M. Dienerowitz and K. Dholakia. "Transfer of Orbital Angular Momentum from an Optical Vortex Beam to a Nanoparticle", *Topologica*, 2:008-1-008-7, 2009

Conference and seminar contributions

Talks

- M. Dienerowitz, J. Baumgartl, M. Mazilu, T. F. Krauss and K. Dholakia, "Exciting Nanoparticles: Plasmonics in a trap", 12. Deutsche Physikerinnentagung Münster, November 2008
- M. Dienerowitz, M. Mazilu, T. F. Krauss and K. Dholakia, "Exciting Nanoparticles: Plasmonics in a trap", Seminar, Universität Zürich, October 2008, *invited*
- M. Dienerowitz, M. Mazilu, T. F. Krauss and K. Dholakia, "Exciting Nanoparticles: Plasmonics in a trap", Institute Seminar, Universität Karlsruhe, July 2008, *invited*
- M. Dienerowitz, M. Mazilu, P. Reece, T. F. Krauss and K. Dholakia, "Blue-detuned trap for resonant confinement of metal nanoparticles", Nanobiotechnology Seminar, Johannes Gutenberg Universität Mainz, June 2007, *invited*
- M. Dienerowitz, M. Mazilu, P. Reece, T. F. Krauss and K. Dholakia, "Blue-detuned trap for resonant confinement of metal nanoparticles", Optical Trapping and Optical Micromanipulation IV, SPIE NanoScience + Engineering, San Diego, August 2007

- M. Dienerowitz, P. Reece, K. Metzger, T. F. Krauss and K. Dholakia, "Blue-detuned trap for resonant confinement of metal nanoparticles", Molecular Plasmonics 2007, IPHT Jena, May 2007
- M. Dienerowitz, T. F. Krauss and K. Dholakia, "Methods for plasmon-enhanced Raman spectroscopy", The Rank Prize Funds Mini-Symposium on Metamaterials in Nature and Technology, Windermere, August 2006

Posters

- M. Dienerowitz, M. Mazilu, T. F. Krauss and K. Dholakia, "Exciting Nanoparticles: Plasmonics in a trap", Women in Photonics School on Photonic Metamaterials, Paris, April 2008
- M. Dienerowitz, K. Busch, T. F. Krauss and K. Dholakia, "Surface-enhanced Raman scattering on periodic metal nano-structures", Epixnet Winterschool, Pontresina, March 2006

Acknowledgements

I would like to thank both my supervisors Prof. Kishan Dholakia and Prof. Thomas Krauss for their support and help throughout my PhD. Their encouragement and enthusiasm has been very motivating.

I truly enjoyed working with my colleagues of both the "Trapping group" and the "Microphotonics group": Dave Stevenson, Lynn Paterson, Ben Agate, Klaus Metzger, Phil Jess, Janelle Shane, Claire Patterson, Lani Torres, Toni Carruthers, David Gherardi, Andrew Rudhall, Jill Morris, David Carnegie, Steve Lee, Tomas Cizmar, Will Whelan-Curtin , Chris Reardon, Douglas McRobbie and Andrea Di Falco. Particular thanks go to Peter Reece, Steven Neale, Dan Burnham, Martin Ploschner, Michael Mazilu and Jörg Baumgartl who spent hours answering all my questions.

The St Andrews physics department provided a fantastic working atmosphere with a lot of support across group boundaries: I would like to thank Alex Lagatski, Dave Stothard, Chris Hooley, Aly Gillies and Cameron Rae. I cannot forget the support I received from the electronics and mechanical workshop as well as the secretarial staff.

Furthermore I would like to thank the Studienförderwerk Klaus Murmann of the Stiftung der Deutschen Wirtschaft for funding my PhD scholarship.

Finally I must thank my husband Frank for his enormous support and understanding throughout the past years.